National Library of Canada

Acquisitions and Bibliographic Services Branch

395 Wellington Street
Ottawa, Ontario
K1A 0N4

Bibliothèque nationale du Canada

Direction des acquisitions et des services bibliographiques

395, rue Wellington
Ottawa (Ontario)
K1A 0N4

Your file Votre référence

Our file Notre référence

NOTICE

The quality of this microform is heavily dependent upon the quality of the original thesis submitted for microfilming. Every effort has been made to ensure the highest quality of reproduction possible.

If pages are missing, contact the university which granted the degree.

Some pages may have indistinct print especially if the original pages were typed with a poor typewriter ribbon or if the university sent us an inferior photocopy.

AVIS

La qualité de cette microforme dépend grandement de la qualité de la thèse soumise au microfilmage. Nous avons tout fait pour assurer une qualité supérieure de reproduction.

S'il manque des pages, veuillez communiquer avec l'université qui a conféré le grade.

La qualité d'impression de certaines pages peut laisser à désirer, surtout si les pages originales ont été dactylographiées à l'aide d'un ruban usé ou si l'université nous a fait parvenir une photocopie de qualité inférieure.

Canada

Control of a Flexible-Link Manipulator

Howard Geniele

A Thesis

in

The Department

of

Electrical and Computer Engineering

Presented in Partial Fulfilment of the Requirements

for the Degree of Master of Applied Science at

Concordia University

Montreal, Quebec, Canada

June 1994

Abstract

Control of a Flexible-Link Manipulator

Howard Geniele

This thesis focuses on the tip-position control of a single flexible link which rotates in the horizontal plane. The dynamic model is derived using a Lagrangian assumed modes method based on Euler-Bernoulli beam theory. The model is then linearized about an operating point. An output feedback control strategy that uses the principle of transmission zero assignment achieves tracking for this nonminimum phase linear time-invariant system. The control strategy consists essentially of two parts. The first part is an inner (stabilizing) control loop that incorporates a feed-through term to assign the system's transmission zeros at desired locations in the complex plane, and a feedback term to move the system's poles to appropriate positions in the left-half plane. The second part is a feedback servo loop that allows tracking of the desired trajectory. Two controllers that use variations of this method are developed, one of which is implemented on an experimental test-bed. The performance is compared with that of a third controller based on pole placement state feedback.

To my late mother, Lila, and my father, Henry

Contents

List of Figures

List of Tables

CHAPTER 1

Introduction

1.1 The Flexible Manipulator Control Problem

Traditionally, robotic manipulators are designed and built in a manner that maximizes stiffness to minimize vibration and allow for good positional accuracy with relatively simple controllers. High stiffness is achieved by using heavy materials that limit the rapid motion of the manipulator, increase the sizes of the actuators and boost energy consumption. Conversely, a lightweight manipulator is less expensive to manufacture and operate. The reduced inertia results in safer operation and faster response. Weight reduction, however, incurs a penalty in that the manipulator becomes more flexible and more difficult to control accurately. The control difficulty is caused by the fact that since the manipulator is a distributed system, a large number of flexible modes is required to accurately model its behaviour. Further complications arise because of the highly nonlinear nature of the system. In addition, the system is nonminimum phase since the sensor at the manipulator's tip is not colocated with the actuator at the hub.

For a rigid manipulator, the tip trajectory is completely defined by the trajectory of the joint. Effective control of the joint is synonymous with good control of the tip. The situation is not as straightforward for the flexible manipulator. Several possible control objectives exist. One objective consists of (i) tracking a reference joint trajectory while (ii) reducing the elastic arm deflections. This approach rests on the assumption that the motion of the system consists of the elastic displacements of the arm superimposed on the nominal path (the rigid body motion of the manipulator). The two part control system effectively partitions the system into a rigid subsystem and an elastic subsystem (the flexible arm). If the second part of the controller is effective in reducing the elastic

deflections, the behaviour of the closed loop system approximates that of the rigid manipulator. As in the case of the rigid manipulator, the tip trajectory is then defined by the trajectory of the joint which is determined by the first part of the controller. Another objective involves regulating the tip about a desired steady state position. The controller acts by causing the tip to move from a start position to a specified destination position without regard to the path it must follow. Yet another possibility involves having the tip actually track a given trajectory as it moves from its start position to its destination.

In an effort to reduce the complexity, many of the works on flexible manipulator control perform a local linearization of the equations of motion and truncate the number of flexible modes. Canon and Schmitz (1984) applied linear quadratic Gaussian (LQG) control by designing an optimal controller that assumes the availability of all the states of the system. Since the states are not directly measureable, they must be reconstructed from the available input (the applied torque at the hub) and outputs (the hub velocity and the tip position). By assuming that all measurement errors and disturbances have Gaussian probability density functions, an optimal estimator was then used to reconstruct the states. Sakawa *et al* (1985) used linear quadratic (LQ) control to dampen the flexible modes while tracking the hub reference angle. An observer was used to reconstruct the system states, neglecting measurement errors and disturbances. Wang *et al* (1989) used output feedback PD control to design a regulator around a target point that dampens the flexible modes. Wang and Vidyasagar (1990) chose the reflected tip position as the output and devised an output feedback point-to-point linear control based on passivity of the model's transfer function. Siciliano and Book (1988) applied singular perturbation theory to decompose the flexible manipulator into slow and fast subsystems. This procedure only partially linearizes the flexible manipulator model: although the fast subsystem is linear, the slow subsystem is nonlinear. A nonlinear control was developed for the slow subsystem, while a linear state feedback control was used for the fast subsystem. The result was a composite controller that dampens flexible modes while tracking a desired hub angle trajectory.

Most of the foregoing control strategies are designed for models of the flexible manipulator that are linearized about a particular operating point, that is, for a given

(*nominal*) set of hub angle and elastic mode positions and velocities. The greater the variation of these positions and velocities from the operating point, the greater is the variation of the linearized model from the actual system. This variation becomes more pronounced for high performance control systems since high performance implies rapid motion and therefore large departures of the hub angle and elastic mode positions and velocities from their nominal values. System performance and stability will degrade unless the situation is addressed. To overcome this problem, various researchers have developed nonlinear controllers incorporating the principle of nonlinear inversion. De Luca and Siciliano (1988) used the input-output inversion algorithm (Hirschorn 1979) to develop two controllers. One controller defines the output as the joint angle and asymptotically tracks it. The other controller defines the output as the position of a point along the arm and tracks a trajectory specified for that point. As the location of the point nears the tip, in an attempt to achieve tracking of the tip itself, the zero dynamics of the system become unstable and the control becomes difficult. Madhavan and Singh (1991) also used the Hirschorn algorithm to design a nonlinear controller for a two link flexible manipulator. They also specified the output to be a point along the arm, but not at its end, to prevent the occurence of unstable zero dynamics. The location of the point, however, is sufficiently close to the arm's tip so that the closed-loop system is marginally stable. Once the trajectory nears its steady-state value, (and the dynamics of the manipulator are almost linear), a linear stabilizer control loop is closed. This linear stabilizer dampens the vibrations and ensures asymptotic tracking of the reference trajectory. Madhavan and Singh (1992) applied the theory of sliding modes to design a controller that tolerates a wide range of payload uncertainty and thus exhibits a certain robustness. (Sliding mode control strategies belong to the class of variable structure control systems (VSS) and are characterized by structures that are switched abruptly to achieve a control objective.) As in Madhavan and Singh (1991), the output is chosen to be a point near the arm's tip to avoid unstable zero dynamics. The separate linear stabilizer control loop is also retained.

Shifman (1990) designed a controller that asymptotically tracks a desired end point trajectory without truncating the series of elastic modes. This is achieved by defining the desired trajectories of (i) the end point, (ii) the hub angle, and (iii) τ_d, the torque applied

to the hub. An error space is then specified, in which the actual values of the three foregoing quantities are subtracted from their desired trajectories. The partial differential Euler-Bernoulli equation that describes the motion of the manipulator is then rewritten in terms of the error space. A composite control signal τ is designed such that $\tau=\tau_d+\tau'$, where τ' is a linear control that acts on a function defined in the error space and minimizes the perturbations of the hub angle and the end point from their desired trajectories.

The foregoing control schemes are designed according to a specific flexible manipulator model. If the model accurately describes the actual manipulator, the controller will perform as expected. Problems can occur due to discrepancies between the model and the actual system. Such discrepancies include the effects of truncated higher order elastic modes, unmodeled friction and backlash effects and, for linearized models, system nonlinearities. The control schemes exhibit varying degrees of performance and stability, (that is, robustness), in the face of these uncertainties. Yuan *et al* (1989) have designed a robust adaptive controller that attains a specific level of robustness for a model with a prescribed amount of uncertainty. This is achieved by separating the system into a nominal part that has been linearized about a particular operating point, and a nonlinear part that accounts for uncertainty in the linear model. Model reference adaptive control is used together with a full state robust observer.

The approach taken in this thesis involves linearizing the nonlinear equations of motion to simplify the design of the controller. The controller consists of two parts. An outer (servo) control loop yields the desired tracking of the reference input. An inner (stabilizing) loop incorporates a feedforward term, which addresses the nonminimum phase behaviour, and a feedback term that stabilizes the overall closed-loop system.

The design of the controller is based on the work of Patel and Misra (1992). The original contribution of this thesis lies in the design and construction of an experimental test-bed to implement and assess the performance of the controller. The simulations presented in Geniele *et al* (1992), and the experimental results shown in Patel *et al* (1993) are extended to provide a more in-depth analysis of the controller's performance.

It is important to note that the control theory discussed in this thesis is not restricted to the flexible-link manipulator, and may be applied to a larger class of nonminimum phase systems.

1.2 The Flexible Manipulator

To reduce the complexity of a multiple degree of freedom flexible-link manipulator operating in three dimensional space, and yet capture the essence of the control problem, a single-link flexible manipulator has been constructed. As shown in Figure 1.1, the 1.2 m long manipulator rotates in the horizontal plane to minimize the effects of gravity. It consists of a central stainless steel tube with annular surface corrugations. Aluminum blocks are bolted to the tube, and two thin parallel spring steel strips slide freely within slots cut into the blocks. Since the tube resists torsional flexure, and the steel strips resist vertical flexure, the resulting structure is lightweight (1.45 kg), strong and horizontally flexible. This approach attempts to reduce the coupling between the horizontal and the vertical and torsional modes of vibration. A high performance drive was assembled consisting of a pulse width modulated amplifier that operates in current feedback mode, a brush-type permanent magnet DC servo motor and, to eliminate backlash, a Harmonic Drive speed reducer. A combination of two sensors is used to measure the position of the manipulator's end point with respect to an inertial reference frame: (i) a photodetector, located at and revolving with the hub, monitors an infrared emitting diode located at the tip and (ii) an incremental optical encoder mounted on the motor shaft measures the position of the hub. The digital controller samples the sensor outputs and computes the desired torque required from the servo motor.

1.3 Organization of the Thesis

Chapter 2 discusses the modeling of the flexible manipulator. The derivation proceeds step-by-step from the simple static cantilever beam (fixed at one end and free at the other) through to the dynamic rotating flexible manipulator. Concepts from static beam theory, (the study of beam deflection under static loads), are presented so that the reader may

gain a thorough comprehension of the basic theory defining the flexible beam model. The section proceeds with the dynamic beam problem that incorporates the dimension of time to yield the Euler-Bernoulli partial differential equation. Lagrange's equations generate the final nonlinear equations of motion of the rotating flexible manipulator which are linearized to yield a simpler representation of the system about a particular operating point. The section concludes with measurement of the actual manipulator parameters, and validation of the model by comparing the responses of the actual flexible manipulator and the model to a given input.

Chapter 3 describes the design of the control systems. The principle of transmission zero assignment, which forms the basis for the design of two distinct controllers, is explained. Chapter 4 presents computer simulations of the controllers and compares the results. Chapter 5 describes the actual flexible manipulator test-bed and implements one of the controllers designed in Chapter 3. Conclusions and suggestions for further work are discussed in Chapter 6.

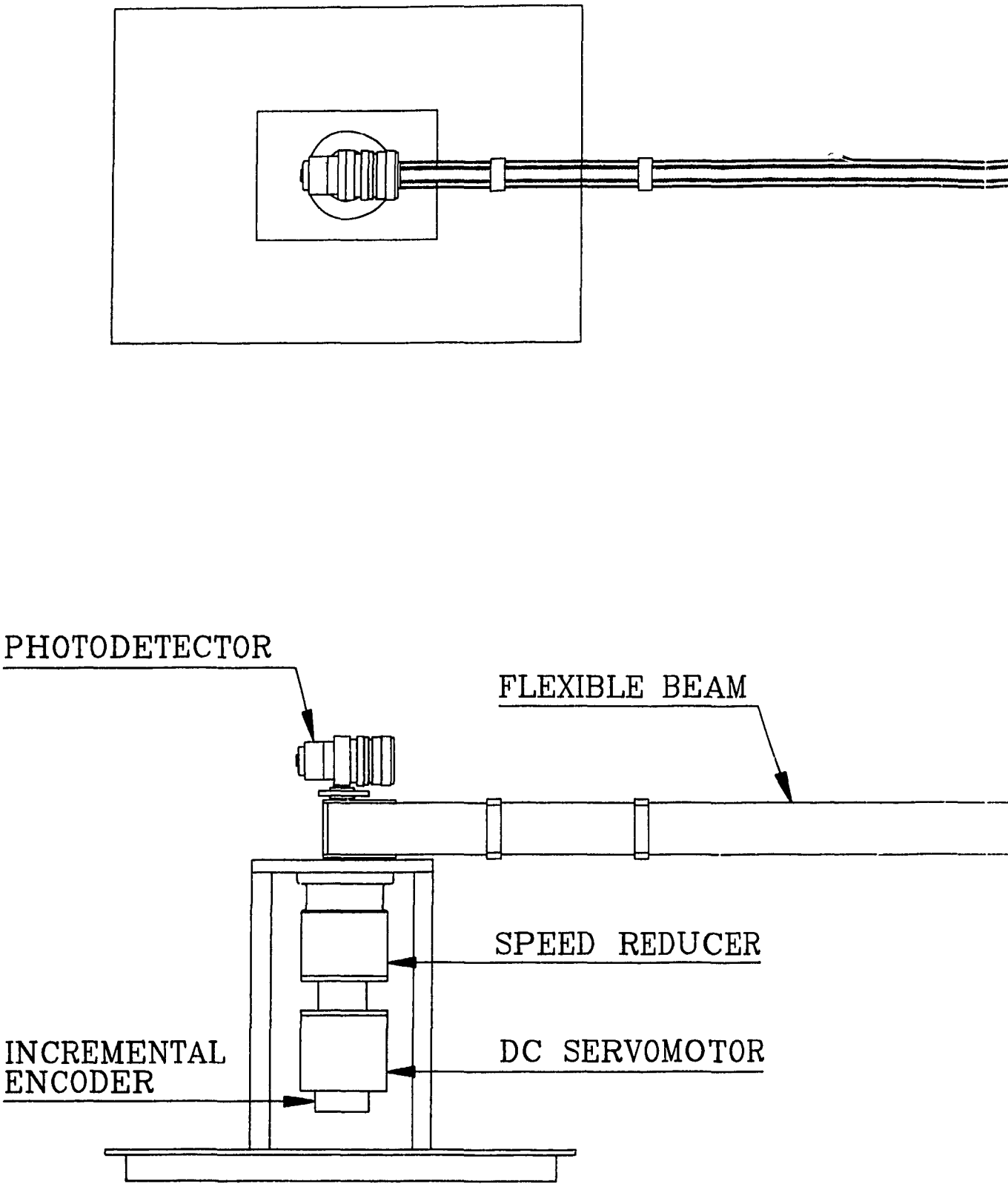

Figure 1.1 The flexible manipulator.

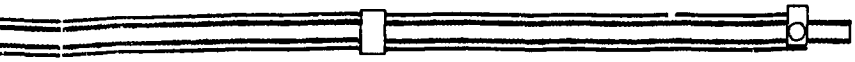

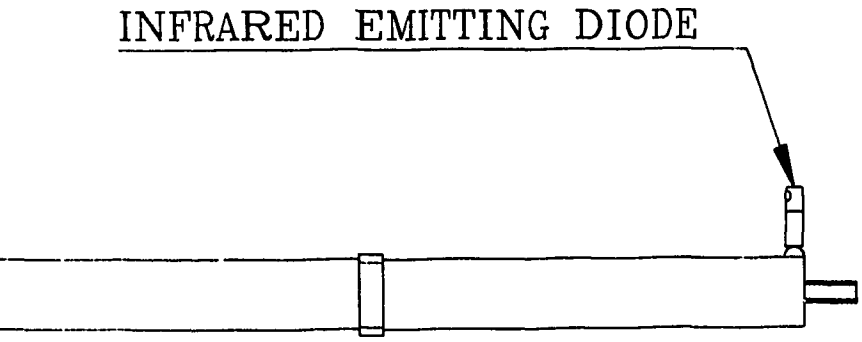
INFRARED EMITTING DIODE

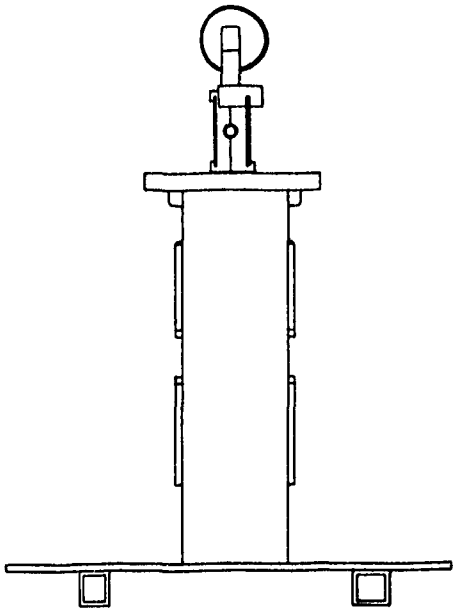

Chapter 2

The Model

2.1 Introduction

This section develops the model for the flexible manipulator from basic concepts that begin with the static deflection of beams as described by elementary beam theory. Expressions for the deflection of a beam are derived as a function of distance along the beam and the boundary conditions of moment and shear force.

The **dynamic** deflection, i.e. vibration, of a beam is then explored. A partial differential equation (PDE) known as Euler's beam equation is used to model this distributed parameter system, yielding an expression for the deflection that is a function of both time and distance along the beam. Using the separation of variables method, Euler's beam equation is expressed as two ordinary differential equations (ODE's). Frequencies of vibration and the role of boundary conditions are analyzed. Lagrange's equation yields the equations of motion of the vibrating beam. The effects of damping are explored. A simplified dynamic model that neglects higher frequencies of vibration, the assumed modes model, is examined.

The preceding theory is then extended to the case of interest - the flexible manipulator rotating in the horizontal plane. Lagrange's equation is used to yield the equations of motion of the manipulator. This model is linearized to yield the simplified equations of motion.

Finally, the experimental manipulator's parameters are measured and are incorporated into the model. The accuracy of the model is verified by comparing its response with that of the experimental manipulator.

2.2 Static Beam Theory

2.2.1 Fundamentals

The objective of this section is to determine the static deflection of a beam caused by an applied load. Several concepts that are fundamental to the field of statics will now be explained. The modulus of elasticity, or Young's modulus (E), relates the elongation (strain, ε) of a material to the applied stress (force per cross sectional area of the material, σ) by the expression $\sigma = E\varepsilon$. E defines the stiffness or rigidity of the material.

Different portions of a beam are in tension and compression when subject to a bending moment. There exists a neutral axis within the beam along which elements of the beam are in neither tension nor compression. The radius of curvature of the neutral axis is defined as ρ.

The area moment of inertia about the neutral axis, I, is a measure of an object's resistance to bending solely as a result of its geometry. For example, a long bar of rectangular cross section bends more easily about its thinner dimension than about its thicker dimension.

The stiffness factor EI will appear regularly and is a measure of the stiffness of an object that takes into account the object's material and its geometry.

2.2.2 The Cantilever Beam

Consider the cantilever beam (fixed at one end and free at the other) in Figure 2.1. The beam is of constant cross sectional area, length h and mass m. Gravitational acceleration g acts in the negative W direction, creating a load $p(x) = -mg/h$ distributed uniformly along the length of the beam ($p(x)$ has dimensions of force per unit length).

An upward or *reaction* force, $R=mg$, occurs at the fixed end $x=0$. R is equal and opposite to the gravitational force acting on the beam $F_g=-mg$. Force F_g produces a *moment* M, that is, a tendency to cause rotation of the beam in the clockwise direction. Reaction moment M_0 occurs at $x=0$ in a counter-clockwise direction. M_0 is equal to F_g multiplied by the distance from its point of application. The point of application of the force caused by a uniform load is at the beam's centre of mass, at $x=h/2$. M_0 is therefore

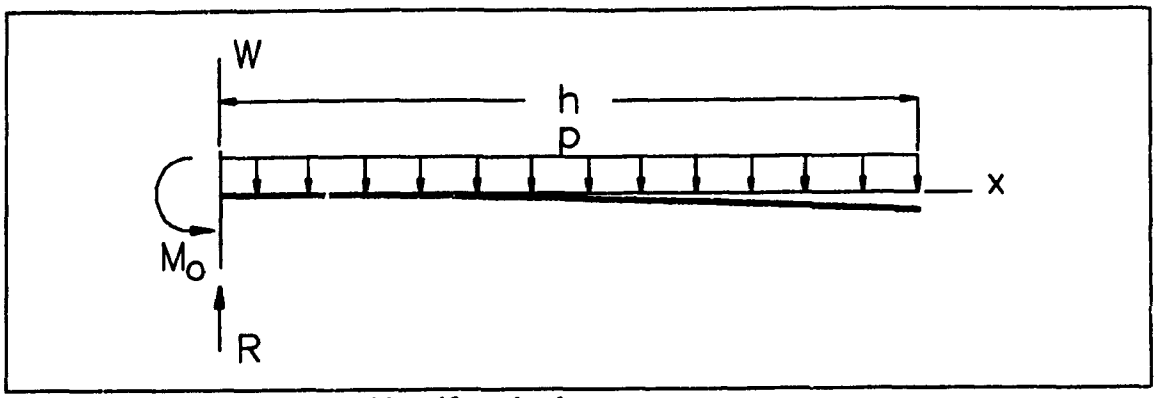

Figure 2.1 Cantilever beam with uniform load.

equal to $-mgh/2$. Both R and M_0 counteract the effect of load $p(x)$ and keep the cantilever beam in an equilibrium or *static* state.

Beam Deflection - Uniform Load

If the external forces and moments acting on the beam were the only quantities of interest, the problem would now be solved. Determination of the beam's deflection, however, requires analysis of the internal forces and moments in the beam.

As shown in Figure 2.2, shear force tends to break the beam perpendicular to its longitudinal axis. Shear force is calculated at a specific location x along the beam by summing all external forces on either the left side or the right side of x. The convention used for this analysis is to consider the forces to the left of x. Upward forces are positive while downward forces are negative.

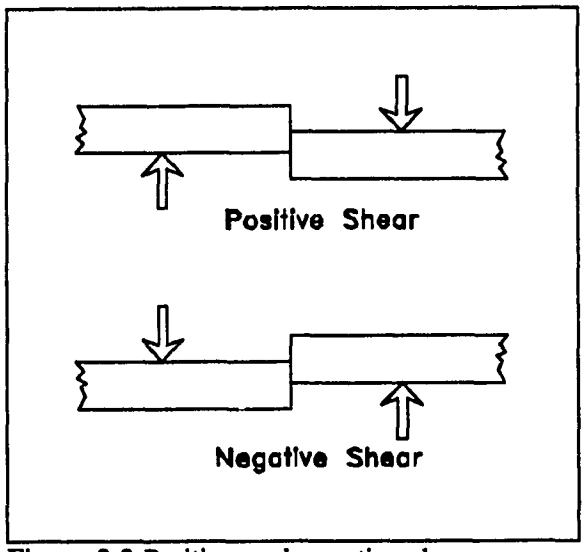

Figure 2.2 Positive and negative shear.

The shear S and bending moment M at the boundaries of the beam, (x=0 and x=h), will now be determined. R is the only force acting to the left of $x=0^+$ (an infinitesimal distance to the right of x=0). Hence, $S(0)=R$. The forces to left of x=h include R and the downward force $-mg$ (found by

integrating load $p(x)$ from $x=0$ to $x=h$). Therefore, $S(h)=R-mg=0$.

A negative bending moment M tends to flex the beam so that the upper portion of the beam is in tension (stretched) while the lower portion is in compression (see Figure 2.3). The bending moment at location x equals the sum of the moments of the forces to the left of x. At $x=h$, the moment M_h equals the sum of the negative reaction moment M_0, the positive moment produced by R, and the negative moment produced by F_g acting at the centre of mass. That is,

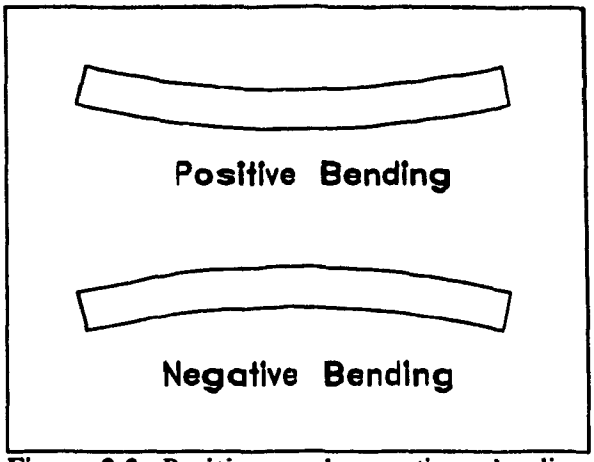

Figure 2.3 Positive and negative bending moments.

$$\begin{aligned} M_h &= M_0 + Rh + F_g\frac{h}{2} \\ &= -\frac{mgh}{2} + mgh - \frac{mgh}{2} \\ &= 0. \end{aligned}$$

At $x=0^+$, the moment is simply M_0.

Shear force and bending moment are related by the equation

$$S = \frac{dM}{dx}. \tag{2.1}$$

In the case of a distributed load the relation may be written

$$\frac{dS}{dx} = \frac{d^2M}{dx^2} = p(x). \tag{2.2}$$

It can be shown (Shigley, 1983) that the curvature of a beam undergoing a bending moment is

$$\frac{1}{\rho} = \frac{M}{EI}. \tag{2.3}$$

The curvature of a plane curve is specified as

$$\frac{1}{\rho} = \frac{d^2w/dx^2}{[1+(dw/dx)^2]^{3/2}} \tag{2.4}$$

where w is the deflection of the beam at any point x along its length. The slope of the beam is

$$\theta = \frac{dw}{dx}.$$

If the slope is very small, the denominator of Eq. (2.4) is approximately unity, and Eq. (2.3) can be rewritten as

$$\frac{M}{EI} = \frac{d^2w}{dx^2}. \tag{2.5}$$

Noting Eqs. (2.1) and (2.2) and repeatedly differentiating Eq. (2.5), we get

$$\frac{S}{EI} = \frac{d^3w}{dx^3}$$
$$\frac{p}{EI} = \frac{d^4w}{dx^4}$$

where EI is assumed to be constant and, as before, p is the load intensity with dimensions of force per unit length.

These relations are normally displayed in a group as:

$$EI\frac{d^4w}{dx^4} = p(x) \quad (\textit{load intensity}) \tag{2.6}$$

$$EI\frac{d^3w}{dx^3} = S(x) \quad (\textit{shear}) \tag{2.7}$$

$$EI\frac{d^2w}{dx^2} = M(x) \quad (\textit{moment}) \tag{2.8}$$

$$\frac{dw}{dx} = \theta(x) \quad (\textit{slope}) \tag{2.9}$$

$$w = f(x) \quad (\textit{deflection}). \tag{2.10}$$

To solve the problem of the cantilever beam under a uniform load, integrate Eq. (2.6) with $p = -mg/h$. Then integrate Eq's. (2.7) through (2.9), solving for the constants

of integration with the boundary conditions:

$$EI\frac{d^3w(x=L)}{dx^3} = S(L)=0$$

$$EI\frac{d^2w(x=L)}{dx^2} = M(L)=0$$

$$EI\frac{dw(x=0)}{dx} = EI\,\theta(0)=0$$

$$EI\,w(x=0) = 0.$$

The expression for the beam's deflection is,

$$w = \frac{mgx^2}{24EIh}(4hx-x^2-6h^2).$$

Figure 2.4 shows the loading, deflection, shear and moment diagrams.

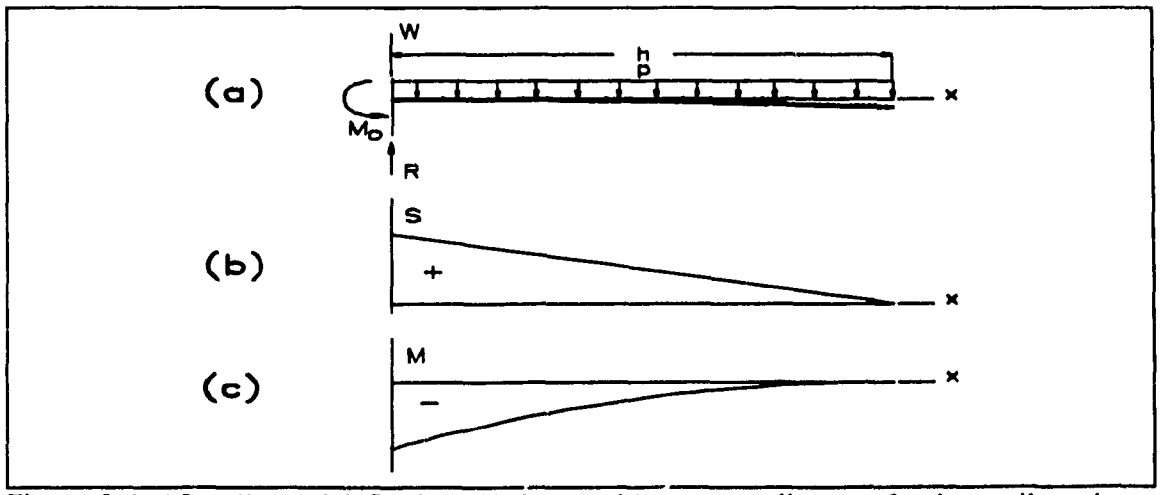

Figure 2.4 (a) Loading and deflection, (b) shear and (c) moment diagrams for the cantilever beam with uniform loading.

Beam Deflection - Uniform Load Plus Concentrated Load At Free End

Consider the cantilever beam with uniform loading $p(x) = -mg/h$ and the addition of a concentrated force $-F$ at the free end as shown in Figure 2.5. Such a concentrated force can result from a point mass located at the free end in the presence of gravity.

Reaction force R, at x=0, is equal and opposite to the sum of the gravitational force acting on the beam (F_g=$-mg$) and force $-F$: $R = mg + F$. Reaction moment M_0 is

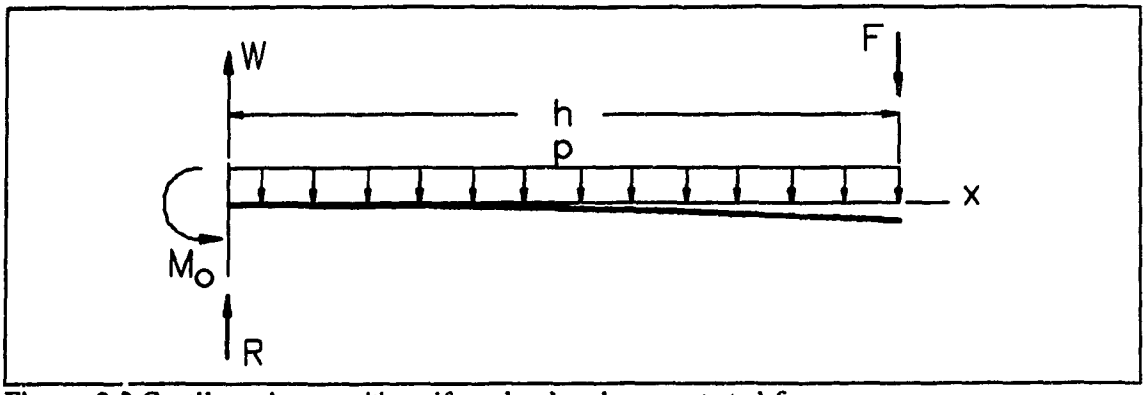

Figure 2.5 Cantilever beam with uniform load and concentrated force.

equal to the sum of the moments caused by F_g and $-F$: $M_0 = -mgh/2 - Fh$.

The shear forces and moments at the boundaries of the beam, (x=0 and x=h), will now be determined. R is the only force acting to the left of $x=0^+$. Hence, $S(0)=R$. The forces to the left of $x=h$ include R and the downward force $-mg$ (found by integrating load $p(x)$ from x=0 to x=h). Therefore, $S(h)=R-mg=F$.

At $x=h$, the moment M_h equals the sum of the negative reaction moment M_0, the positive moment produced by R and the negative moment produced by F_g acting at the centre of mass. That is,

$$\begin{aligned} M_h &= M_0 + Rh + F_g\frac{h}{2} \\ &= \left(-\frac{mgh}{2} - Fh\right) + (mg + F)h - \frac{mgh}{2} \\ &= 0. \end{aligned}$$

At $x=0^+$, the moment is simply M_0.

To solve the problem of the cantilever beam under a uniform load and concentrated force, we integrate Eq. (2.6) with $p = -mg/h$. Then we integrate Eq's. (2.7) through (2.9), solving for the constants of integration with the boundary conditions:

$$\begin{aligned} S(0) &= R \qquad S(h) = F \\ M(0) &= M_0 \quad M(h) = 0 \\ \theta(0) &= 0 \\ w(0) &= 0. \end{aligned}$$

The expression for the beam's deflection is,

$$w = \frac{x^2}{2EI}\left(\frac{(mg+F)x}{3} - \frac{mgx^2}{12h} - \frac{mgh}{2} - Fh\right).$$

2.3 The Dynamic Beam Problem

2.3.1 The Euler-Bernoulli Equation

The Euler-Bernoulli beam equation is one of the simpler expressions describing the transverse vibration of beams, and may be derived from Eq's. (2.6) through (2.9). All quantities now feature two independent variables: time, t, as well as horizontal distance, x. It is assumed that rotary inertia, (the inertia associated with rotation of the beam in the x-w plane), and deformation of the beam due to shear forces may be neglected. EI is assumed to be constant. The derivatives in Eq's. (2.6) through (2.9) may then be replaced with partial derivatives as follows:

$$EI\frac{\partial^4 w}{\partial x^4} = \frac{\partial S}{\partial x} = p(x,t) \tag{2.11}$$

$$EI\frac{\partial^3 w}{\partial x^3} = \frac{\partial M}{\partial x} = S(x,t) \tag{2.12}$$

$$EI\frac{\partial^2 w}{\partial x^2} = M(x,t) \tag{2.13}$$

$$\frac{\partial w}{\partial x} = \theta(x,t) \tag{2.14}$$

$$w = f(x,t)\ . \tag{2.15}$$

Consider the differential beam element of length dx shown in Figure 2.6. The mass of the beam per unit length is specified as γ, and the acceleration of the differential beam element is $\partial^2 w/\partial t^2$. The loading per unit length of the beam, $p(x,t)$, is equal to the sum of the inertia load per unit length, $\gamma\partial^2 w/\partial t^2$, and the lateral external force per unit length, $p_f(x,t)$.

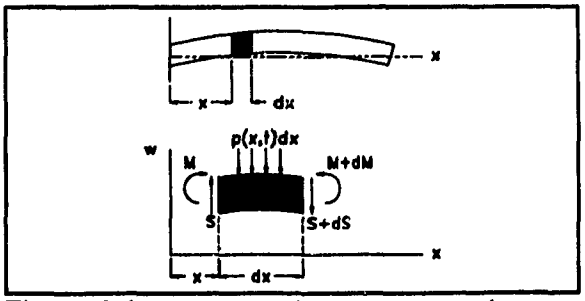

Figure 2.6 Forces and moments acting on differential beam element dx.

The equation of motion for the element in the vertical direction is given by

Newton's second law as

$$-(S+dS)-p_f(x,t)dx+S=\gamma dx\frac{\partial^2 w}{\partial t^2}.$$

Since $dS=\frac{\partial S}{\partial x}dx$,

$$-p_f dx-\left(\frac{\partial S}{\partial x}\right)dx=\gamma\left(\frac{\partial^2 w}{\partial t^2}\right)dx. \tag{2.16}$$

Substituting Eq. (2.11) into Eq. (2.16), we obtain the Euler-Bernoulli equation for constant EI

$$EI\frac{\partial^4 w}{\partial x^4}+\gamma\frac{\partial^2 w}{\partial t^2}=-p_f(x,t). \tag{2.17}$$

For the case of free vibration, $p_f(x,t)=0$, and Eq. (2.17) becomes

$$\frac{EI}{\gamma}\frac{\partial^4 w}{\partial x^4}+\frac{\partial^2 w}{\partial t^2}=0. \tag{2.18}$$

To obtain a solution for Eq. (2.18) by the separation of variables method, we theorize that the beam always maintains a fixed shape $\phi(x)$ and that only the amplitude varies with time. That is, we assume a solution of the form

$$w(x,t)=\phi(x)q(t). \tag{2.19}$$

Eq. (2.19) leads to the two equations

$$\frac{\partial^4 w}{\partial x^4}=\frac{d^4\phi}{dx^4}q$$

and

$$\frac{\partial^2 w}{\partial t^2}=\phi\frac{d^2 q}{dt^2}=\phi\ddot{q}.$$

Substituting the above into Eq. (2.18) gives

$$\frac{EI}{\gamma}\frac{d^4\phi}{dx^4}q=-\phi\ddot{q}.$$

Dividing both sides of this equation by the product ϕq yields

$$\frac{EI}{\gamma}\frac{d^4\phi}{dx^4}\frac{1}{\phi} = -\frac{\ddot{q}}{q}. \tag{2.20}$$

Since the expression on the left involves functions depending only on x and the expression on the right involves functions depending only on t, both expressions must be equal to a constant, say ω^2. Thus

$$\frac{EI}{\gamma}\frac{d^4\phi}{dx^4}\frac{1}{\phi} = -\frac{\ddot{q}}{q} = \omega^2.$$

This yields the two ordinary differential equations

$$\ddot{q} + \omega^2 q = 0 \tag{2.21}$$

and

$$\frac{d^4\phi}{dx^4} - k^4\phi = 0 \tag{2.22}$$

in which

$$k^4 = \frac{\omega^2\gamma}{EI}. \tag{2.23}$$

The solution of Eq. (2.21) is

$$q(t) = A\cos\omega t + B\sin\omega t. \tag{2.24}$$

Eq. (2.22) is of the form

$$B(\phi) = \lambda C(\phi) \tag{2.25}$$

where B and C are linear differential operators and ϕ is a function of x only. This particular form constitutes an eigenvalue problem for which the number λ is an eigenvalue and $\phi(x)$ is an eigenfunction. It can be shown (Thomson, 1988 and James, Wolford and Whaley, 1989) that the solution of Eq. (2.22) is

$$\phi(x) = C\cosh kx + D\sinh kx + E\cos kx + F\sin kx. \tag{2.26}$$

The solution of Euler's beam equation is written as

$$w(x,t) = (C\cosh kx + D\sinh kx + E\cos kx + F\sin kx)\,q(t) \tag{2.27}$$

in which $q(t)$ is given by Eq. (2.24).

2.3.2 The Cantilever Beam With An Inertia Tip Load

A complete solution of the cantilever beam problem with an inertia tip load consisting of point mass M_p requires solving for the constants C through F in Eq. (2.27). These constants are calculated using the following boundary conditions:

At $x = 0$	**At $x = L$**
$w = 0$	$M = EI\dfrac{d^2w}{dx^2} = 0$
$\dfrac{dw}{dx} = 0.$	$S = EI\dfrac{d^3w}{dx^3} = M_p\dfrac{\partial^2 w(h,t)}{\partial t^2}.$

The condition on S follows from the fact that M_p causes concentrated force $M_p\dfrac{\partial^2 w}{\partial t^2}$ to act on the beam at $x=h$. Substituting these boundary conditions into Eq. (2.27) leads to the transcendental equation

$$\frac{M_p k}{\gamma}(\sin kh\cosh kh - \cos kh\sinh kh) - \cosh kh\cos kh - 1 = 0. \tag{2.28}$$

For M_p=0, Eq. (2.28) reduces to

$$\cosh kh\ \cos kh + 1 = 0. \tag{2.29}$$

From Eq. (2.23), the natural frequencies of vibration are

$$\omega_n = (k_n h)^2\sqrt{\frac{EI}{\gamma h^4}}.$$

An infinite number of values of kh exists that satisfy Eq. (2.28), each of which corresponds to a natural frequency of vibration. That infinitely many natural frequencies exist is to be expected due to the continuously distributed mass and elasticity of the beam. Specifying the position of each particle in the beam requires an infinite number of

coordinates or *modes*, and the beam is said to possess an infinite number of degrees of freedom.

Table 2.1 lists numerical values of $(k_n h)^2$ for a beam of length 1.2 m and mass 1.42 kg. The results are tabulated for (i) M_p=0 kg and (ii) M_p=0.03 kg. Note the smaller values corresponding to M_p=0.03 kg. Since the natural frequencies are proportional to $(k_n h)^2$, introduction of an inertia load at the tip decreases the natural frequencies.

n	$(k_n h)^2$	
	$(M_p=0)$	$(M_p=0.03\text{kg.})$
1	3.516	3.376
2	22.035	21.213
3	61.700	59.529
4	120.902	116.893

Table 2.1 $(k_n h)^2$ for a cantilever beam with and without inertia load M_p at the free end.

Solution of the Dynamic Beam Problem

To each of the natural frequencies ω_n, corresponds a specific mode shape function $\phi_n(x)$ and a specific amplitude function or *normal coordinate* $q_n(t)$. A single solution to the deflection problem may be written

$$w_n(x,t) = \phi_n(x)\, q_n(t)\,.$$

The single solution $w_n(x,t)$ will not usually satisfy the initial conditions for position, $w(x,0)$, and velocity, $\dot{w}(x,0)$. Since Eq. (2.18) is linear and homogeneous, the principle of superposition holds that the sum of infinitely many solutions w_n is a solution of (2.18). That is,

$$w(x,t) = \sum_{n=1}^{\infty} \phi_n(x) q_n(t)\,. \tag{2.30}$$

Eq. (2.30) may be interpreted as a consequence of the eigenvalue problem defined by Eq. (2.22). As previously explained, the set of functions $\{\phi_n(x), n = 1,2,...,\infty\}$ is the set of eigenfunctions of Eq. (2.22). The eigenfunctions of a continuous system are orthogonal and can be normalized to produce an orthonormal set of functions. Such an orthonormal set of functions can be used to uniquely express any arbitrary function $f(x)$. At any instant of time $t=\beta$, the function $w(x,\beta)$ can therefore be uniquely expressed as a linear

combination

$$w(x,\beta) = a_1\phi_1(x) + a_2\phi_2(x) + \ldots + a_N\phi_N(x) \tag{2.31}$$

where a_n is constant and N tends to infinity. As $w(x,t)$ varies with time, it can be expressed in the form of Eq. (2.31) by choosing the values $\{a_n\}$ to be time varying, that is

$$w(x,t) = q_1(t)\phi_1(x) + q_2(t)\phi_2(x) + \ldots + q_N(t)\phi_N(x)$$

where N tends to infinity.

Eigenfunction Determination

To determine $\phi_n(x)$, begin with Eq. (2.27)

$$w(x,t) = (C\cosh kx + D\sinh kx + E\cos kx + F\sin kx)\,q(t) \tag{2.27}$$

and the boundary conditions

1) $w(0,t) = 0$

2) $\dfrac{\partial w(0,t)}{\partial x} = 0$

3) $\dfrac{\partial^2 w(h,t)}{\partial x^2} = 0$

4) $\dfrac{\partial^3 w(h,t)}{\partial x^3} = \dfrac{M_p}{EI}\dfrac{\partial^2 w(h,t)}{\partial t^2}$.

Substituting the boundary conditions into Eq. (2.27) yields the following expression for $\phi(x)$:

$$\phi(x) = -D\left(\sin kx - \sinh kx - \frac{(\sin kh + \sinh kh)}{(\cos kh + \cosh kh)}(\cos kx - \cosh kx)\right). \tag{2.32}$$

The individual mode functions $\phi_n(x)$ are found by substituting the values k_n determined from the transcendental frequency equation, Eq. (2.28) and by substituting the coefficients d_n for $-D$:

$$\phi_n(x) = d_n\left(\sin k_n x - \sinh k_n x - \frac{(\sin k_n h + \sinh k_n h)}{(\cos k_n h + \cosh k_n h)}(\cos k_n x - \cosh k_n x)\right). \tag{2.33}$$

Finally, the $\phi_n(x)$ are normalized by choosing d_n to satisfy $\int_0^h \phi_n^2(x)\,dx = 1$. Figure 2.7 shows some typical mode shape functions for a cantilever beam with an inertia tip load.

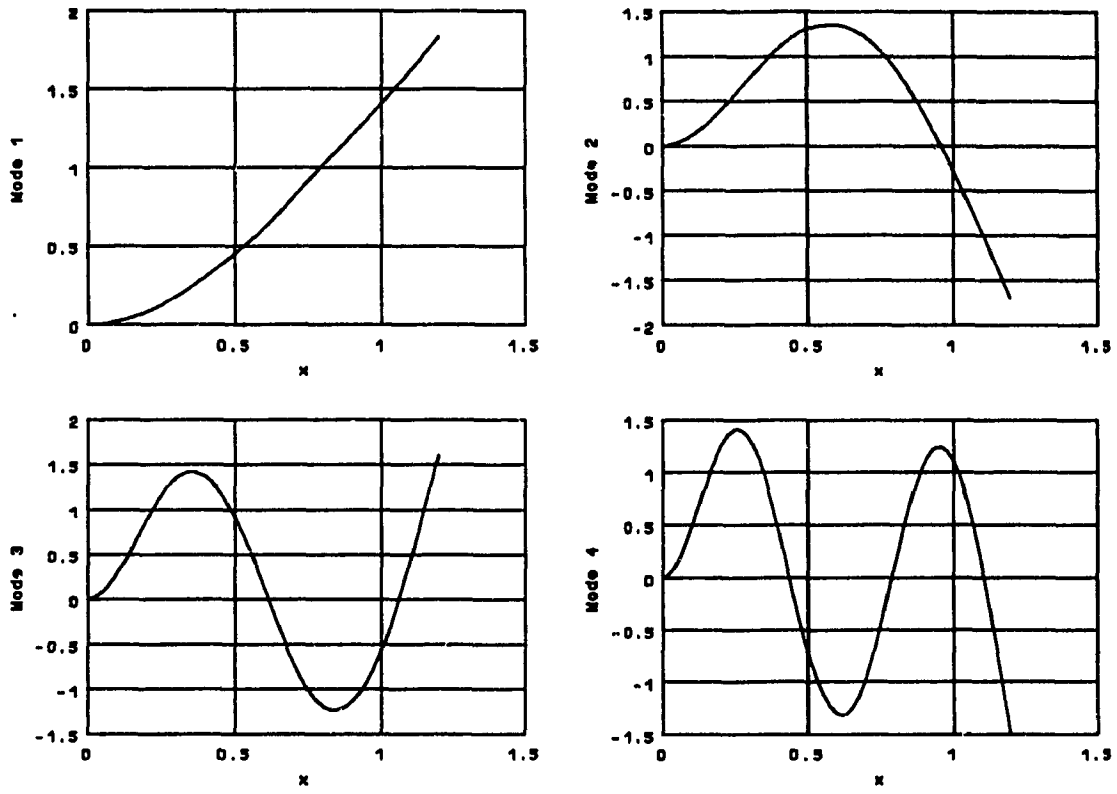

Figure 2.7 The first four mode shape functions for a cantilever beam with an inertia load at the free end.

As described in Thomson (1988), the normal coordinate $q_n(t)$ may be found from Lagrange's equation by first determining the kinetic and potential energies. Lagrange's equation is written as

$$\frac{d}{dt}\left(\frac{\partial K}{\partial \dot{q}_n}\right) - \frac{\partial K}{\partial q_n} + \frac{\partial U}{\partial q_n} = H_n . \tag{2.34}$$

The kinetic energy is

$$K = \frac{1}{2}\sum_{n=1}^{\infty} M_n \dot{q}_n^2 \tag{2.35}$$

where the generalized mass M_n is

$$M_n = \int_0^h \phi_n^2(x)\gamma dx + M_p \phi_n^2(h) . \tag{2.36}$$

The potential energy is

$$U = \frac{1}{2}\sum_{n=1}^{\infty} K_n q_n^2 \tag{2.37}$$

where K_n is the generalized stiffness given by

$$K_n = \int_0^h EI[\phi_n''(x)]^2 dx . \tag{2.38}$$

To account for the forcing function $p_f(x,t)$ the generalized force is defined as

$$H_n = \int_0^h p_f(x,t)\phi_n(x)dx . \tag{2.39}$$

After substituting into Lagrange's equation, the differential equation for q_n is written as

$$M_n\ddot{q}_n + K_n q_n = \int_0^h p_f(x,t)\phi_n(x)dx . \tag{2.40}$$

Dividing both sides of Eq. (2.40) by M_n yields

$$\ddot{q}_n + \omega_n^2 q_n = \frac{1}{M_n}\int_0^h p_f(x,t)\phi_n(x)dx . \tag{2.41}$$

where $\omega_n^2 = K_n/M_n$. For the case where $p_f(x,t)$ is separable in the form

$$p_f(x,t) = \frac{P_0}{h} p_f(x)g(t) \tag{2.42}$$

Eq. (2.41) may be rewritten as

$$\ddot{q}_n + \omega_n^2 q_n = \frac{P_o}{M_n} \Gamma_n g(t) \tag{2.43}$$

where

$$\Gamma_n = \frac{1}{h} \int_0^h p_f(x) \phi_n(x) dx \tag{2.44}$$

is the *mode participation factor* for mode n. The solution of Eq. (2.43) is

$$\begin{aligned} q_n(t) = {} & q_n(0) \cos \omega_n t + \frac{1}{\omega_n} \dot{q}_n(0) \sin \omega_n t \\ & + \left(\frac{P_0 \Gamma_n}{M_n \omega_n 2} \right) \omega_n \int_0^t g(\xi) \sin \omega_n (t - \xi) d\xi . \end{aligned} \tag{2.45}$$

2.3.3 The Assumed Modes Method

Equation (2.30) states that an exact solution to the Euler-Bernoulli PDE requires an infinite number of modes. The assumed modes method approximates the exact solution by using a finite number of modes,

$$w(x,t) = \sum_{n=1}^{N} \psi_n(x) q_n(t)$$

where the $\psi_n(x)$ are any functions that satisfy the boundary conditions. Choosing a finite, i.e. N, number of modes has the effect of approximating the continuous system by means of an N degrees of freedom discrete system. If the functions $\psi_n(x)$ are selected to be a set of polynomials in x, as is frequently the case, the resulting frequencies of vibration are only approximations to the actual natural frequencies of the system. If the functions $\psi_n(x)$ are chosen to equal the eigenfunctions $\phi_n(x)$, the frequencies of vibration equal the natural frequencies of the system. The deflection of the cantilever beam can therefore be approximated by

$$w(x,t) = \sum_{n=1}^{N} \phi_n(x) q_n(t) .$$

Mode Selection

It is important to remember that some of the idealizations used to derive the Euler-Bernoulli equation include: (i) perfectly elastic material, (ii) uniform cross-section and density, (iii) small deflections, and (iv) negligible rotary inertia and shear deformation. Furthermore, the concept of infinitely many modes is inherently false since it implies infinitely large natural frequencies, and that the particles in the structure move faster than the speed of light. In view of this argument, one may interpret Eq. (2.30) as implying that the actual beam consists of a very large, but finite, number of modes. This assertion begs the question, "How many modes are required?". Hughes (1987) attempts to answer this question by deriving three model error indices based on a set of "modal identities". For example, the first error index, ε_1, is based on the modal identity

$$\sum_{n=1}^{\infty} P_n^2 = \gamma h \tag{2.46}$$

where P_n, the modal coefficient of momentum about x=0, is

$$P_n = \gamma \int_0^h \phi_n \, dx \, .$$

Equation (2.46) leads to the relation

$$0 = 1 - 4 \sum_{n=1}^{\infty} \nu_n^{-2} \kappa_n^2 \tag{2.47}$$

where $\nu_n = \gamma \omega_n^2 h^4 / EI$ and $\kappa_n = (\sinh \nu_n - \sin \nu_n)/(\cosh \nu_n + \cos \nu_n)$. If only the first N modes are retained, Eq. (2.47) has a non-zero value. Defining this value to be $\varepsilon_1(N)$, Eq. (2.47) becomes

$$\varepsilon_1(N) = 1 - 4 \sum_{n=1}^{N} \nu_n^{-2} \kappa_n^2 \, . \tag{2.48}$$

Index ε_1 is therefore a measure of the error related to the modeling of P. Error index $\varepsilon_2(N)$ corresponds to the error related to H, the modal coefficient of angular momentum about x=0. $\varepsilon_3(N)$ is a measure of the error involving both H and natural frequency ω_n. All three indices equal unity for N equal to zero, and all three tend to zero as N tends to infinity. Plots of the indices show that they decrease rapidly for increasing

N. For N=4, for example, ε_1=0.10, ε_2=0.0065, and ε_3<0.00001

Although these indices relate to P, H and ω_n, it is not clear how they relate to the actual deflection, $w(x,t)$. In spite of this deficiency, this approach is meaningful since it does quantify the mode selection process.

2.3.4 Damping

Damping is present in most physical systems and the cantilever beam is no exception. Both structural and Coulomb damping are present. To have a tractable mathematical model, the net damping effect is modeled by viscous damping. All three types are now examined.

Viscous Damping

The viscous damping force for the n'th mode is proportional to $\dot{q}_n$, the derivative of the normal coordinate, and is written

$$F_n = c_n \dot{q}_n \tag{2.49}$$

where c_n is the viscous damping coefficient. The equation of motion for vibration of the n'th mode has been derived in Section 2.3.2 as

$$M_n \ddot{q}_n + K_n q_n = H_n$$

where H_n is the n'th generalized force. For the undamped system, H_n is a function of forcing function $p_f(x,t)$. For the damped case, however, H_n also consists of the (nonconservative) damping force F_n:

$$H_n = \int_0^h p_f(x,t)\phi_n(x)\,dx - F_n \,. \tag{2.50}$$

The damped equation for free vibration of the n'th mode is written by setting $p_f(x,t)$=0 in Eq. (2.50), yielding

$$M_n \ddot{q}_n + c_n \dot{q}_n + K_n q_n = 0 \,. \tag{2.51}$$

The general solution of Eq. (2.51) is

$$q_n(t) = A_1 e^{\left(-\zeta+(\zeta^2-1)^{\frac{1}{2}}\right)\omega_n t} + A_2 e^{\left(-\zeta-(\zeta^2-1)^{\frac{1}{2}}\right)\omega_n t} \tag{2.52}$$

where ζ is the damping ratio and A_1 and A_2 are constants determined from the initial conditions. For underdamped systems $\zeta < 1$ and the solution, Eq. (2.52), becomes

$$q_n(t) = Q_n e^{-\zeta\omega_n t}\cos\left(\sqrt{1-\zeta^2}\,\omega_n t - \Omega\right) \tag{2.53}$$

where Q_n and Ω are constants determined from the initial conditions. For initial conditions $q_n(0) = q_0$ and $\dot{q}_n(0) = \dot{q}_0$:

$$Q_n = \sqrt{q_0^2 + \left(\frac{\dot{q}_0 + \zeta\omega_n q_0}{\sqrt{1-\zeta^2}\,\omega_n}\right)^2}$$

$$\Omega = \tan^{-1}\left(\frac{q_0\omega_n\sqrt{1-\zeta^2}}{\dot{q}_0 + \zeta\omega_n q_0}\right).$$

Equation (2.53) describes a sinusoid of frequency $\omega_n\sqrt{1-\zeta^2}$ and an amplitude that decays according to the factor $Q_n e^{-\zeta\omega_n t}$.

Energy Loss

The expression for energy loss due to viscous damping in one cycle of vibration is found by integrating the viscous damping force with respect to the normal coordinate, that is,

$$\Delta W = \oint c_n \dot{q}_n dq_n . \tag{2.54}$$

Noting that $dq_n = \dot{q}_n dt$, Eq. (2.54) is rewritten

$$\Delta W = \int_0^{(2\pi/\omega_d)} c_n \dot{q}_n^2 dt \tag{2.55}$$

where $\omega_d = \omega_n\sqrt{1-\zeta^2}$ is the frequency of damped vibration.

Substituting Eq. (2.53) into Eq. (2.55) gives

$$\Delta W = \pi \omega_n c_n Q_n^2 . \tag{2.56}$$

A graphical interpretation of the energy dissipated per cycle by the damping force can be made by considering the case of steady-state forced vibration in which generalized force H_n is a harmonic function with frequency ω_f. The energy dissipated by the damping force is supplied by the excitation. Assume that q_n exhibits a simple harmonic response of the form

$$q_n = Q_n \cos(\omega_f t - \Omega) . \tag{2.57}$$

The expression for the viscous damping force is found by substituting Eq. (2.57) into Eq. (2.49)

$$F_n = c_n \dot{q}_n = -c_n \omega_f Q_n \sin(\omega_f t - \Omega) . \tag{2.58}$$

Eqs. (2.57) and (2.58) can be combined to yield

$$\left(\frac{F_n}{c_n \omega_f Q_n} \right)^2 + \left(\frac{q_n}{Q_n} \right)^2 = 1 . \tag{2.59}$$

When plotted, the relationship between damping force and displacement yields a curve referred to as a hysteresis loop. The hysteresis loop resulting from Eq. (2.59) is an ellipse in the q_n-F_n plane as shown in Figure 2.8. The energy lost in one cycle of vibration is given by the area enclosed by the ellipse.

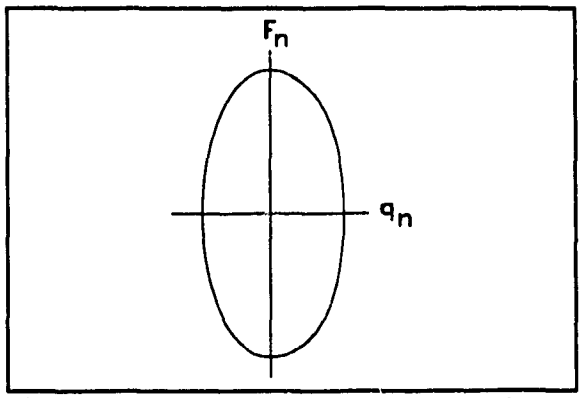

Figure 2.8 The energy dissipated by viscous damping equals the area enclosed by the ellipse.

Structural Damping

Solid materials, especially metals, exhibit a type of damping caused by internal friction within the material called *structural* or *hysteretic* damping. Experiments have shown that for structural damping, the energy dissipated per cycle of vibration is approximately proportional to the square of the amplitude and is independent of frequency:

$$\Delta W = \alpha_n Q_n^2 \tag{2.60}$$

where α_n is a constant.

A typical structural damping hysteresis curve depicting energy loss for steady state forced vibration is shown in Figure 2.9. It is difficult to incorporate structural damping directly into the equations of motion because, unlike viscous damping, it is a nonlinear function of displacement and is defined in terms of energy loss.

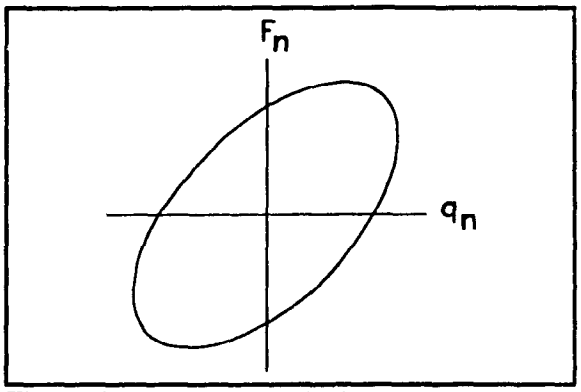

Figure 2.9 The energy dissipated by structural damping equals the area enclosed by the ellipse.

Coulomb Damping

Coulomb damping occurs when sliding contact exists between components of a system. As explained in Section 1.2, the flexible manipulator is a composite structure that incorporates two thin, parallel spring steel strips that slide freely within slots cut into aluminum blocks. This sliding action is a source of Coulomb damping. The magnitude of the damping force F_n is equal to the product of the coefficient of friction, μ, and the normal force between the contact surfaces, f

$$F_n = \mu f .$$

Coulomb damping is accounted for in the differential equation of motion by noting that it opposes the direction of motion, that is, its sign is opposite that of $\dot{q}_n$. For the case of free vibration, the equations of motion are written

$$M_n \ddot{q}_n + \mu f + K_n q_n = 0 \text{ for } \dot{q}_n > 0$$
$$M_n \ddot{q}_n - \mu f + K_n q_n = 0 \text{ for } \dot{q}_n < 0 .$$

Coulomb damping is nonlinear due to the abrupt transition of F_n as the sign of $\dot{q}_n$ changes.

For the case of free vibration, Coulomb damping is characterized by a linearly decaying harmonic function of time, as shown in Figure 2.10.

The frequency of oscillation is unaffected by the damping. Contrast this behaviour with that of viscous damping where the amplitude of the oscillation decays exponentially with time and the frequency of oscillation is reduced by the factor $\sqrt{1-\zeta^2}$.

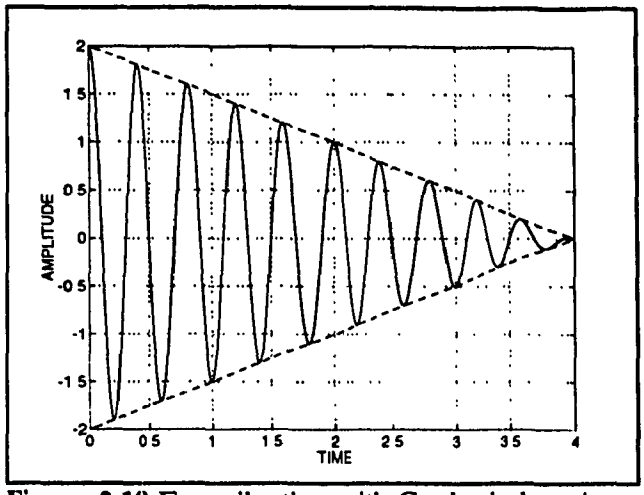

Figure 2.10 Free vibration with Coulomb damping.

Equations of Motion

The final equations of motion for the cantilever beam using the assumed modes method and approximating structural and Coulomb damping by viscous damping are written

$$\begin{aligned}
M_1\ddot{q}_1 + c_1\dot{q}_1 + K_1 q_1 &= \int_0^h p(x,t)\phi_1(x)\,dx \\
M_2\ddot{q}_2 + c_2\dot{q}_2 + K_2 q_2 &= \int_0^h p(x,t)\phi_2(x)\,dx \\
M_3\ddot{q}_3 + c_3\dot{q}_3 + K_3 q_3 &= \int_0^h p(x,t)\phi_3(x)\,dx \\
&\vdots \\
M_N\ddot{q}_N + c_N\dot{q}_N + K_N q_N &= \int_0^h p(x,t)\phi_N(x)\,dx
\end{aligned} \tag{2.61}$$

where M_N is given by Eq. (2.36) and K_N is given by Eq. (2.38).

The analysis of the cantilever beam is now complete. The next phase involves extending this theory to the flexible-manipulator problem.

2.4 The Flexible Manipulator Model

The preceding theory describing the dynamic behaviour of the cantilever beam is now extended to the flexible-link manipulator. In this configuration the beam is no longer fixed but is free to rotate in response to the application of a torque exerted at the hub. The strategy used to write the equations of motion of the system is the same as for the cantilever beam; once the kinetic and potential energies of the system are determined, Lagrange's equations yield the equations of motion. These nonlinear equations will then be linearized to facilitate the development of a control law in subsequent chapters.

2.4.1 Lagrange's Equations

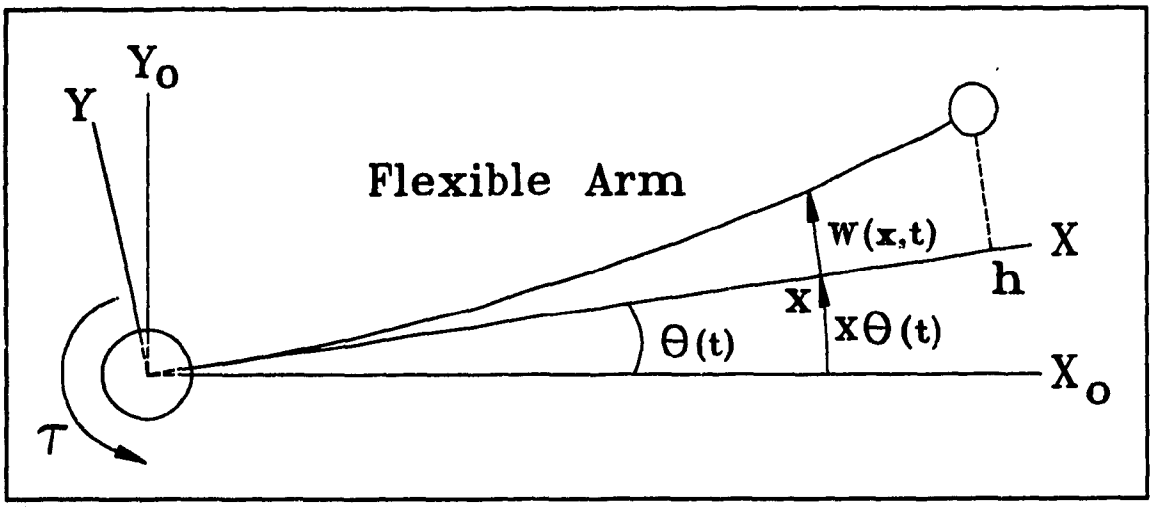

Figure 2.11. Schematic of the flexible link.

Figure 2.11 defines the position of any point along the link $y(x,t)=x\theta(t)+w(x,t)$. As for the cantilever beam, the effects of rotary inertia and shear deformation are ignored by assuming that the cross-sectional area of the link is small in comparison with its length h. Euler-Bernoulli beam theory and the assumed modes method can be used to express the deflection of a point located at a distance x along the arm as

$$w(x,t) = \sum_{i=1}^{N} \phi_i(x)\, q_i(t) \tag{2.62}$$

where $q_i(t)$ is the generalized coordinate of the i'th mode. As defined in Wang and Vidyasagar (1989), $\phi_i(x)$ is the normalized, clamped-free eigenfunction of the i'th mode.

Energy Relations

In the case of the cantilever beam, the coordinate frame used to express the deflection w at a position x along the arm is itself an inertial or base frame. For the flexible manipulator, however, w and x are expressed with respect to the rotating X-Y frame. As explained in Wang and Vidyasagar (1989), the vector $\boldsymbol{P}(x)$ defines the deflection and position of a point on the arm with respect to the inertial X_0-Y_0 frame as follows,

$$\boldsymbol{P}(x) = \begin{pmatrix} x\cos\theta - w\sin\theta \\ x\sin\theta + w\cos\theta \end{pmatrix}$$

and

$$\dot{\boldsymbol{P}}^t\dot{\boldsymbol{P}} = x^2\dot{\theta}^2 + \dot{w}^2 + 2\dot{w}x\dot{\theta} + w^2\dot{\theta}^2 . \tag{2.63}$$

The kinetic energy K is written as

$$K = \frac{1}{2}I_h\dot{\theta}^2 + \frac{1}{2}\int_0^h \dot{\boldsymbol{P}}^t\boldsymbol{P}\,dm + \frac{1}{2}M_p\dot{\boldsymbol{P}}^t(h)\dot{\boldsymbol{P}}(h) \tag{2.64}$$

where

$$\dot{\boldsymbol{P}}^t(h)\dot{\boldsymbol{P}}(h) = h^2\dot{\theta}^2 + \dot{w}^2(h) + 2\dot{w}(h)h\dot{\theta} + w^2(h)\dot{\theta}^2 . \tag{2.65}$$

Since $dm = \gamma dx$ for the uniform beam, the integral term in Eq. (2.64) is rewritten as

$$\frac{1}{2}\int_0^h \dot{\boldsymbol{P}}^t\dot{\boldsymbol{P}}\,dm = \frac{\gamma}{2}\int_0^h \dot{\boldsymbol{P}}^t\dot{\boldsymbol{P}}\,dx . \tag{2.66}$$

Substituting Eq. (2.63) into Eq. (2.66) yields

$$\frac{\gamma}{2}\int_0^h \dot{\boldsymbol{P}}^t\dot{\boldsymbol{P}}\,dx = \frac{\gamma}{2}\int_0^h (\dot{\theta}^2x^2 + \dot{w}^2 + \dot{w}x\dot{\theta} + w^2\dot{\theta}^2)\,dx . \tag{2.67}$$

Since $w(x,t) = \sum_{n=1}^{N}\phi_n(x)q_n(t)$ and $\dot{w}(x,t) = \sum_{n=1}^{N}\phi_n(x)\dot{q}_n(t)$, the three integrals

involving these terms in Eq. (2.67) are solved as follows:

$$\text{(i)} \quad \int_0^h \dot{w}^2 dx = \int_0^h (\sum_{n=1}^N \phi_n \dot{q}_n)^2 dx = \int_0^h \sum_{i=1}^N \sum_{j=1}^N \phi_i \phi_j \dot{q}_i \dot{q}_j dx = \sum_{i=1}^N \sum_{j=1}^N \dot{q}_i \dot{q}_j \int_0^h \phi_i \phi_j dx .$$

The ϕ_i's are orthonormal, i.e.,

$$\int_0^h \phi_i \phi_j dx = \begin{cases} 0, & i \neq j \\ 1, & i = j \end{cases}$$

and

$$\int_0^h \dot{w}^2 dx = \sum_{i=1}^N \dot{q}_i^2 \int_0^h \phi_i^2 dx = \sum_{i=1}^N \dot{q}_i^2 . \tag{2.68}$$

$$\text{(ii)} \quad \int_0^h \dot{w} x \dot{\theta} dx = \dot{\theta} \int_0^h \dot{w} x dx = \dot{\theta} \int_0^h x \sum_{i=1}^N \dot{q}_i \phi_i dx = \dot{\theta} \sum_{i=1}^N \dot{q}_i \int_0^h x \phi_i dx . \tag{2.69}$$

$$\text{(iii)} \quad \int_0^h w^2 dx = \int_0^h (\sum_{i=1}^N \phi_i q_i)^2 dx = \int_0^h \sum_{i=1}^N \sum_{i=1}^N \phi_i \phi_j q_i q_j dx = \sum_{i=1}^N \sum_{j=1}^N q_i q_j \int_0^h \phi_i \phi_j dx = \sum_{i=1}^N q_i^2 . \tag{2.70}$$

Making the appropriate substitutions, Eq. (2.64) is rewritten as

$$K = \frac{1}{2} I_h \dot{\theta}^2 + \frac{\gamma h^3}{6} \dot{\theta}^2 + \frac{\gamma}{2} \sum_{i=1}^N \dot{q}_i^2 + \gamma \dot{\theta} \sum_{i=1}^N \dot{q}_i \int_0^h x \phi_i dx + \frac{\gamma}{2} \dot{\theta}^2 \sum_{i=1}^N q_i^2 + \frac{M_p}{2} \left(h^2 \dot{\theta}^2 + (\sum_{i=1}^N \phi_i(h) \dot{q}_i)^2 + 2h\dot{\theta} \sum_{i=1}^N \phi_i(h) \dot{q}_i + \dot{\theta}^2 (\sum_{i=1}^N \phi_i(h) q_i)^2 \right). \tag{2.71}$$

The potential energy U is

$$U = \frac{1}{2}\int_0^h EI\left(\frac{\partial^2 w}{\partial x^2}\right)dx = \frac{EI}{2}\int_0^h\left(\sum_{i=1}^N q_i\frac{d^2\phi_i}{dx^2}\right)^2 dx = \frac{EI}{2}\int_0^h\sum_{j=1}^N\sum_{k=1}^N q_j q_k\frac{d^2\phi_i}{dx^2}\frac{d^2\phi_k}{dx^2}dx$$

$$U = \frac{EI}{2}\sum_{j=1}^N\sum_{k=1}^N q_j q_k\int_0^h\frac{d^2\phi_j}{dx^2}\frac{d^2\phi_k}{dx^2}dx.$$

Since $\int_0^h\frac{d^2\phi_j}{dx^2}\frac{d^2\phi_k}{dx^2}dx = 0$ for j≠k,

$$U = \frac{EI}{2}\sum_{i=1}^N q_i^2\int_0^h\left(\frac{d^2\phi_j}{dx^2}\right)^2 dx = \frac{EI}{2}\sum_{i=1}^N q_i^2\int_0^h(\phi_i'')^2 dx \tag{2.72}$$

where $\phi_i'' = \frac{d^2\phi_i}{dx^2}$.

It can be shown that $\int_0^h(\phi_i'')^2 dx = k_i^4 = \frac{\omega_i^2\gamma}{EI}$. Equation (2.72) can therefore be rewritten as

$$U = \frac{\gamma}{2}\sum_{i=1}^N q_i^2\omega_i^2 . \tag{2.73}$$

The Lagrangian, $L=K-U$, is written as

$$L = \frac{\dot\theta^2}{2}\left(I_h + \frac{\gamma h^3}{3} + \gamma\sum_{i=1}^N q_i^2\right) + \frac{\gamma}{2}\sum_{i=1}^N\dot q_i^2 + \gamma\dot\theta\sum_{i=1}^N\dot q_i\int_0^h x\phi_i dx + \frac{M_p}{2}\left(h^2\dot\theta^2 + (\sum_{i=1}^N\phi_i(h)\dot q_i)^2 + 2h\dot\theta\sum_{i=1}^N\phi_i(h)\dot q_i + \dot\theta^2(\sum_{i=1}^N\phi_i(h)q_i)^2\right) - \frac{\gamma}{2}\sum_{i=1}^N q_i^2\omega_i^2 . \tag{2.74}$$

Lagrange's equations are

$$\frac{d}{dt}\left(\frac{\partial L}{\partial \dot{\theta}}\right) - \frac{\partial L}{\partial \theta} = H_\theta$$
$$\frac{d}{dt}\left(\frac{\partial L}{\partial \dot{q}_j}\right) - \frac{\partial L}{\partial q_j} = H_j, \quad j = 1,2,\ldots,N \ . \tag{2.75}$$

The generalized force H_θ consists of the applied hub torque $\tau(t)$ and the hub frictional and damping torque F_θ, and is written as $H_\theta = \tau(t) - F_\theta$; F_θ is the sum of the viscous damping torque, $b\dot{\theta}$ and the Coulomb friction torque, $c_{coul}\,\mathrm{sgn}(\dot{\theta})$: $F_\theta = b\dot{\theta} + c_{coul}\,\mathrm{sgn}(\dot{\theta})$. ($b$ and c_{coul} are the coefficients of viscous damping and Coulomb friction, respectively). The generalized forces H_j consist simply of viscous damping forces F_j, that is, $H_j = -F_j = -c_j\dot{q}_j$.

We write the equations of motion by substituting Eq. (2.74) into Eq. (2.75):

$$\ddot{\theta}\left\{I_h + \frac{\gamma h^3}{3} + \gamma\sum_{i=1}^{N} q_i^2 + M_p\left(h^2 + (\sum_{i=1}^{N}\phi_i(h)q_i)^2\right)\right\} +$$
$$\dot{\theta}\left(2\gamma\sum_{i=1}^{N} q_i\dot{q}_i + M_p\sum_{k=1}^{N}\sum_{m=1}^{N}\phi_k\phi_m(\dot{q}_k q_m + q_k\dot{q}_m)\right) + \tag{2.76a}$$
$$b\dot{\theta} + c_{coul}\,\mathrm{sgn}(\dot{\theta}) + \sum_{i=1}^{N}\ddot{q}_i\left(\gamma\int_0^h \phi_i x\,dx + M_p h\phi_i(h)\right) = \tau(t)$$

$$\ddot{\theta}\left(\gamma\int_0^h \phi_j x\,dx + M_p h\phi_j(h)\right) + \gamma\ddot{q}_j + M_p\phi_j(h)\sum_{i=1}^{N}\phi_i(h)\ddot{q}_i + c_j\dot{q}_j -$$
$$\left(\dot{\theta}^2\gamma - EI\int_0^h(\phi_j'')^2\,dx\right)q_j - M_p\dot{\theta}^2\phi_j(h)\sum_{i=1}^{N}\phi_i(h)q_i = 0 \ . \tag{2.76b}$$

Equation (2.76) may be written in the matrix form

$$\boldsymbol{M}(q)\begin{pmatrix}\ddot{\theta}\\ \ddot{\boldsymbol{q}}\end{pmatrix}+\boldsymbol{C}(\boldsymbol{q},\dot{\boldsymbol{q}})\begin{pmatrix}\dot{\theta}\\ \dot{\boldsymbol{q}}\end{pmatrix}+\boldsymbol{K}(\theta)\begin{pmatrix}\theta\\ \boldsymbol{q}\end{pmatrix}+\begin{pmatrix}c_{coul}\operatorname{sgn}(\dot{\theta})\\ \mathbf{0}\end{pmatrix}=\begin{pmatrix}\tau(t)\\ \mathbf{0}\end{pmatrix} \tag{2.77}$$

with the net tip position output

$$y = [h \;\; \Phi(h)]\begin{pmatrix}\theta\\ \boldsymbol{q}\end{pmatrix}$$

where

$$\Phi(h) = [\phi_1(h) \;\; \phi_2(h) \;\; \ldots \;\; \phi_N(h)] \; .$$

Matrix $\boldsymbol{M}(q)$ may be partitioned as

$$\boldsymbol{M}(q) = \begin{bmatrix} m_1 & \boldsymbol{m}_2{}^T \\ \boldsymbol{m}_2 & \boldsymbol{M}_3 \end{bmatrix} \tag{2.78}$$

where

$$m_1 = I_h + \frac{\gamma h^3}{3} + \gamma\sum_{i=1}^{N} q_i^2 + M_p[h^2 + (\sum_{i=1}^{N}\phi_i(h)q_i)^2] \tag{2.79}$$

$$\boldsymbol{m}_2{}^T = \left[\gamma\int_0^h \phi_1 x\,dx + M_p h\phi_1(h) \;\; \gamma\int_0^h \phi_2 x\,dx + M_p h\phi_2(h) \;\; \ldots \;\; \gamma\int_0^h \phi_n x\,dx + M_p h\phi_N(h)\right] \tag{2.80}$$

and

$$\boldsymbol{M}_3 = \begin{bmatrix} \gamma + M_p\phi_1^2(h) & M_p\phi_1(h)\phi_2(h) & .. & M_p\phi_1(h)\phi_N(h) \\ M_p\phi_2(h)\phi_1(h) & \gamma + M_p\phi_2^2(h) & .. & M_p\phi_2(h)\phi_N(h) \\ . & . & .. & . \\ M_p\phi_N(h)\phi_1(h) & M_p\phi_N(h)\phi_2(h) & .. & \gamma + M_p\phi_N^2(h) \end{bmatrix}. \tag{2.81}$$

The term $\boldsymbol{C}(\boldsymbol{q},\dot{\boldsymbol{q}})$ may be partitioned as

$$\boldsymbol{C}(\boldsymbol{q},\dot{\boldsymbol{q}}) = \begin{bmatrix} C_1 & \mathbf{0} \\ \mathbf{0} & \boldsymbol{C}_2 \end{bmatrix} \tag{2.82}$$

where

$$C_1 = b + 2\gamma\sum_{i=1}^{N} q_i\dot{q}_i + M_p\sum_{k=1}^{N}\sum_{m=1}^{N}\phi_k\phi_m(\dot{q}_k q_m + q_k\dot{q}_m) \tag{2.83}$$

and

$$\boldsymbol{C}_2 = \begin{bmatrix} c_1 & 0 & \dots & 0 \\ 0 & c_2 & \dots & 0 \\ 0 & 0 & \dots & c_N \end{bmatrix}. \tag{2.84}$$

The term $\boldsymbol{K}(\dot{\theta})$ may be partitioned and rewritten as follows:

$$\boldsymbol{K}(\dot{\theta}) = \begin{bmatrix} 0 & \mathbf{0} \\ \mathbf{0} & \boldsymbol{K}_1 \end{bmatrix} - \dot{\theta}^2\begin{bmatrix} 0 & \mathbf{0} \\ \mathbf{0} & \boldsymbol{K}_2 \end{bmatrix} \tag{2.85}$$

where

$$\boldsymbol{K}_1 = \gamma\begin{bmatrix} \omega_1^2 & 0 & .. & 0 \\ 0 & \omega_2^2 & .. & 0 \\ . & . & .. & . \\ 0 & 0 & .. & \omega_N^2 \end{bmatrix} \tag{2.86}$$

and

$$\boldsymbol{K}_2 = \begin{bmatrix} \gamma + M_p\phi_1^2(h) & M_p\phi_1(h)\phi_2(h) & .. & M_p\phi_1(h)\phi_N(h) \\ M_p\phi_2(h)\phi_1(h) & \gamma + M_p\phi_2^2(h) & .. & M_p\phi_2(h)\phi_N(h) \\ . & . & .. & . \\ M_p\phi_N(h)\phi_1(h) & M_p\phi_N(h)\phi_2(h) & .. & \gamma + M_p\phi_N^2(h) \end{bmatrix}. \tag{2.87}$$

Model Nonlinearities

Equation (2.77) is the set of nonlinear equations that models the rotating flexible manipulator. In addition to Coulomb friction at the hub, the following nonlinearities occur:

- Inertia matrix $\boldsymbol{M}(\boldsymbol{q})$:

  m_l contains terms involving products of the type q_i^2 and $q_i q_j$ where $i \neq j$. These terms are variations of the rigid body inertia of the manipulator introduced by deflection of the arm.

- Coriolis, and viscous damping matrix $\boldsymbol{C}(\boldsymbol{q},\dot{\boldsymbol{q}})$:

  When multiplied by $\dot{\theta}$, the terms in C_l involving $q_k \dot{q}_k$ and $q_k \dot{q}_m$ where $k=1,2,...,N$ and $m=1,2,...,N$ are Coriolis forces.

- Matrix $\boldsymbol{K}_2$:

  Forming the product $\dot{\theta}^2 \boldsymbol{K}_2 \boldsymbol{q}$ yields the vector of centrifugal forces.

All nonlinear terms noticeably influence the behaviour of the manipulator only when they become significant in relation to their neighbouring *constant* terms. In m_l, for example, the nonlinearities are significant only when they approach the value of $I_h + \gamma h^3/3 + M_p h^2$.

2.4.2 Parameter Evaluation

With the structure of the model having been established in the previous section, all that remains is the evaluation of c_{coul} and the parameters that appear in the matrices $\boldsymbol{M}$, $\boldsymbol{C}$, and $\boldsymbol{K}$. The parameters are grouped into 2 categories: hub parameters and arm parameters.

Hub Parameters

Inertia I_h. I_h is the sum of the encoder, motor, coupling and speed reducer inertias and is referred to the output of the speed reducer. Using the manufacturers' data, I_h=0.30 kg-m^2.

Viscous damping coefficient b and coefficient of Coulomb friction c_{coul}. Since the component manufacturers do not supply friction data, these parameters must be determined experimentally. A constant current I_a is delivered to the motor armature. The motor then develops a constant torque $\tau_m=K_t I_a$, where the torque constant K_t=0.1175 Nm/A. The speed reducer, in turn, transmits a constant torque $\tau=G\tau_m$ to the hub, where the gear ratio G=50. Under the application of constant torque τ, the hub will rotate and accelerate to a constant velocity. At this point the inertial torque is zero and the only torques that oppose τ are due to viscous damping and Coulomb friction. A set of known armature currents I_a are applied and the resulting steady state hub velocities $\dot{\theta}$ are plotted. The speed-torque curve shown in Figure 2.12 is fitted to the experimental data points.

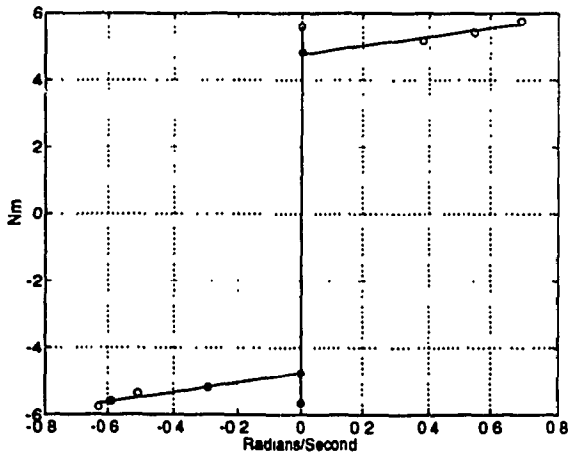

Figure 2.12 Hub viscous damping and friction torque vs. hub velocity.

Coulomb friction is the frictional force in the system when $|\dot{\theta}|$ is just slightly greater than zero. The Coulomb friction coefficients for both positive and negative hub velocities can therefore be found from Figure 2.12. Note the friction values of +5.58 Nm and -5.64 Nm that correspond to zero velocity. These values are due to stiction and represent the torque required to begin rotation. The effects of stiction are neglected in order to simplify the model. For $\dot{\theta}<0$ $c_{coul} \approx 4.77$ Nm and for $\dot{\theta}>0$ $c_{coul} \approx 4.74$ Nm. The viscous damping coefficient b is simply the slope of the speed-torque curve. For $\dot{\theta}<0$ $b \approx 1.29$ Nm/R-s^{-1} and for $\dot{\theta}>0$ $b \approx 1.45$ Nm/R-s^{-1}. The values for b have been obtained by fitting a first order polynomial to experimental data and are necessarily approximations. Furthermore, the Coulomb friction coefficient is also dependent on the hub position. The experimental values given are averaged over several ranges of hub position.

Arm Parameters

Length h. The arm length is 1.2 m.

Uniform mass per unit length γ. γ is found by dividing the arm's mass M by the length h. M is the sum of the masses of the central annular tube, the two parallel spring steel strips, the three aluminum bridges and the infrared emitting diode at the tip, (M = 1.45 kg). γ = 1.45 kg/1.2 m = 1.208 kg/m. Since the lumped masses of the bridges and the diode are included in M, γ only approximates a uniform density.

Stiffness factor EI. EI is measured by applying a known force to the tip with a spring scale and measuring the resulting deflection. EI = 1.94 Nm^2.

Inertia tip load M_p. To simplify the model, the 0.030 kg mass of the infrared emitting diode is neglected: M_p=0.

Natural frequencies of vibration ω_n. The hub is clamped and an impulsive force is applied to the arm. Analysis of the frequency spectrum of the ensuing tip vibrations reveals the

following values for the first four natural frequencies: $\omega_1 = 3.0$ rad/s, $\omega_2 = 19$ rad/s, $\omega_3 = 52$ rad/s and $\omega_4 = 102$ rad/s.

Constants k_n. The k_n's are found by substituting experimentally determined values for h, EI, ω_n and γ into Eq. (2.29b) and solving for k_n yielding $k_1 = 1.5387$, $k_2 = 3.8734$, $k_3 = 6.4062$ and $k_4 = 8.9721$.

Eigenfunctions $\phi_n(x)$. The $\phi_n(x)$'s are calculated by substituting h and k_n into Eq. (2.33) and normalizing to determine the coefficients d_n: $d_1 = 0.6861$, $d_2 = 0.9431$, $d_3 = 0.9375$ and $d_4 = 0.9353$. The first four eigenfunctions are plotted in Figure 2.13.

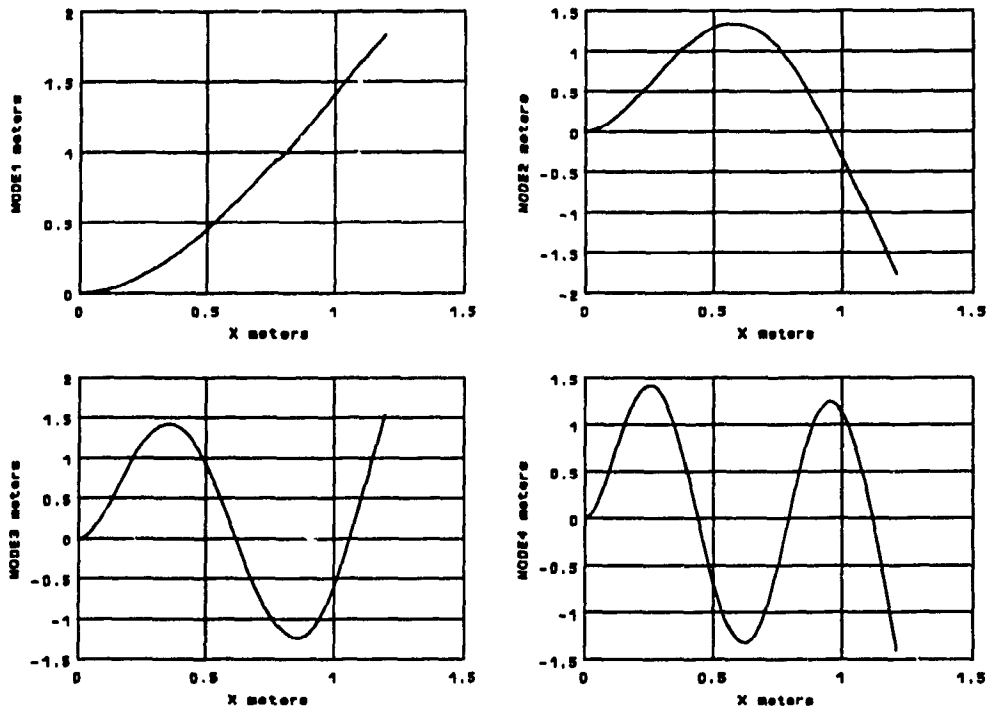

Figure 2.13 Eigenfunctions corresponding to the first four modes.

Damping coefficients c_n. To determine c_1, the hub is clamped. The arm is then given an initial displacement that corresponds to eigenfunction $\phi_1(x)$, (so as to excite only the fundamental frequency ω_1), and is then released. The envelope of the resulting oscillations yields c_1; c_2, c_3 and c_4 are difficult to determine using this procedure because of the

problems in achieving the more intricate initial displacements. As described in Hastings and Book (1987), though, the first two modes exert a greater influence on the accuracy of the model than do the higher modes. It may be argued, then, that precise estimation of the higher modes is not critical for an accurate model; c_2, c_3 and c_4 are set to values that ensure that the response of the model agrees with that of the test-bed when both are subjected to a given torque input $\tau(t)$, i.e., $c_1 = 0.4$, $c_2 = 4.0$, $c_3 = 2.0$ and $c_4 = 5.0$.

2.4.3 Model Validation

The validity of the model represented by Eq. (2.77) is tested by simulating the model's response to two different torque signals. The same torques are applied to the actual test-bed. If the model is accurate, its responses should agree with those of the test-bed. (The simulations were conducted on a SUN 4/370 using MATLAB).

Torque $\tau_1(t)$ and its responses are shown in Figures 2.14 through 2.17, while torque $\tau_2(t)$ and its responses appear in Figures 2.18 through 2.21. Each response figure includes the simulation plot (solid line) and three experimental plots. The Coulomb friction coefficient values used for the simulations differ from the values of Section 2.4.2. Specifically, for $\dot{\theta}<0$, c_{coul} has been reduced by 0.5% to 4.75 Nm and for $\dot{\theta}>0$ c_{coul} has been increased by 5% to 4.98 Nm. These amendments are required because the original values are averaged over a range of hub angles and therefore yield imprecise responses when compared with the test-bed responses, particularly for the hub position.

A single set of Coulomb friction coefficients could not be found that yield good agreement between the model and the test-bed for both $\tau_1(t)$ and $\tau_2(t)$. The amended values are therefore compromises that attempt to reduce this disparity.

The essence of the problem is that the use of a single set of Coulomb friction coefficients leads to an inaccurate model because of the variation of actual Coulomb friction with hub position. Neglecting stiction also contributes to inaccuracy. This dependence on hub position is demonstrated by differences among the three experimental hub position plots for each of the applied torques. These differences are caused by very slight variations of the initial hub positions. The inaccuracy is particularly significant when the value of the applied torque approaches that of the Coulomb friction. The erroneous hub position predicted by the model results in a substantial error at the output.

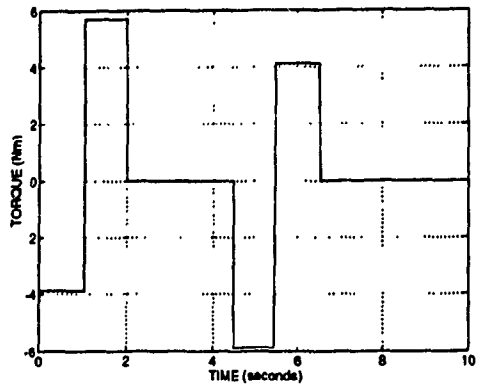

Figure 2.14 Applied torque $\tau_1(t)$.

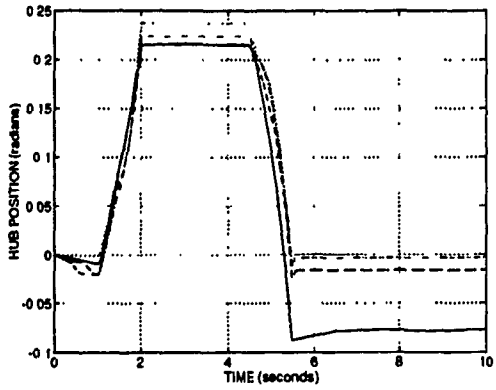

Figure 2.15 Simulated (solid) and experimental hub angles $\theta(t)$.

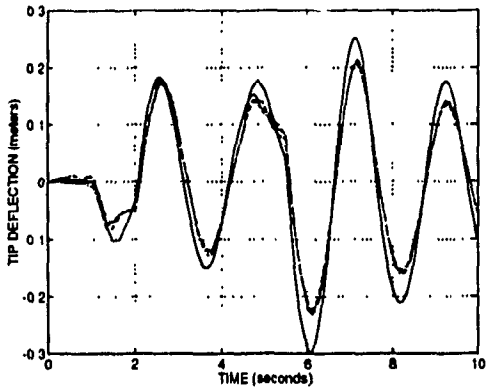

Figure 2.16 Simulaied (solid) and experimental tip deflection $w(h,t)$.

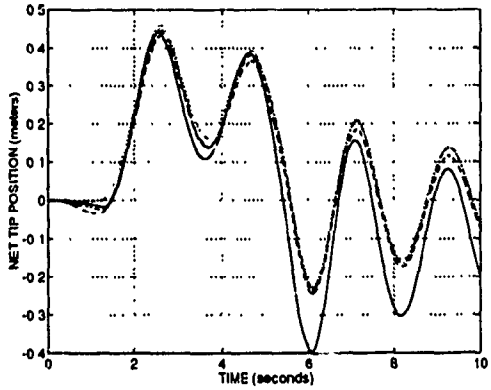

Figure 2.17 Simulated (solid) and experimental net tip position $y = h\theta(t) + w(h,t)$.

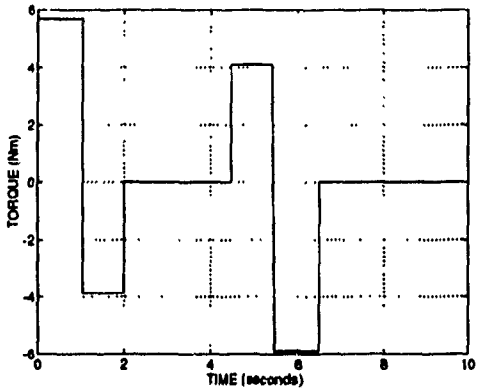

Figure 2.18 Applied torque $\tau_2(t)$.

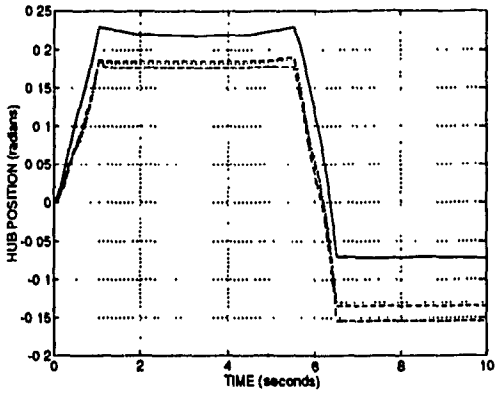

Figure 2.19 Simulated (solid) and experimental hub angles $\theta(t)$.

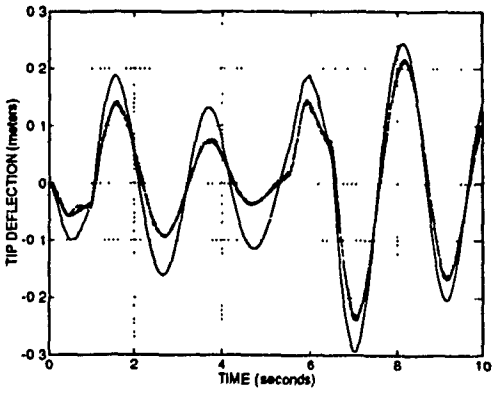

Figure 2.20 Simulated (solid) and experimental tip deflection $w(h,t)$.

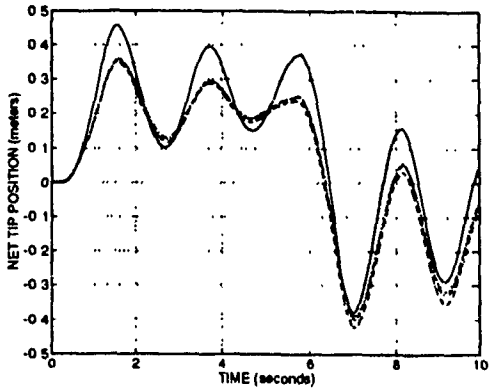

Figure 2.21 Simulated (solid) and experimental net tip position $h\theta(t) + w(h,t)$.

One method of compensating for model errors that cause hub position inaccuracies is to redefine the model such that the input is no longer hub *torque*, but rather hub *position*. This redefinition begs the question: exactly how are these arbitrary hub positions achieved? The solution is to design a control loop that positions the hub as required. Figures 2.22 and 2.23 illustrate the concept. If the position controller of Figure 2.22 is perfect, in that the commanded and actual hub positions are identical, then the schematic of Figure 2.23 results in which the control loop is omitted. This strategy forms the basis for a modified version of the flexible-link model, described in the next section.

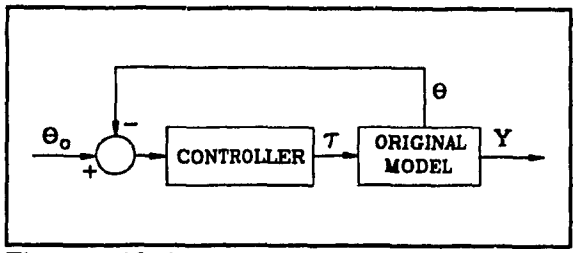

Figure 2.22 Schematic illustrating concept of revised model.

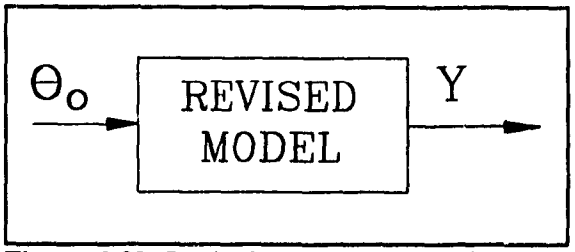

Figure 2.23 Revised model with perfect hub position control.

2.4.4 Revised Model

Assuming that the hub position control action is ideal, the revised nonlinear model of the flexible manipulator will now be derived. Eq. (2.77) is expanded as follows:

$$\begin{bmatrix} m_1 & m_2^T \\ m_2 & M_3 \end{bmatrix}\begin{pmatrix} \ddot{\theta} \\ \ddot{q} \end{pmatrix} + \begin{bmatrix} C_1 & 0 \\ 0 & C_2 \end{bmatrix}\begin{pmatrix} \dot{\theta} \\ \dot{q} \end{pmatrix} + \begin{bmatrix} 0 & 0 \\ 0 & K_1 \end{bmatrix}\begin{pmatrix} \theta \\ q \end{pmatrix} - \dot{\theta}^2\begin{bmatrix} 0 & 0 \\ 0 & K_2 \end{bmatrix}\begin{pmatrix} \theta \\ q \end{pmatrix} + \begin{bmatrix} c_{coul}\mathrm{sgn}(\dot{\theta}) \\ 0 \end{bmatrix} = \begin{pmatrix} \tau(t) \\ 0 \end{pmatrix} . \tag{2.88}$$

Equation (2.88) is rewritten as:

$$m_1\ddot{\theta} + m_2^T\ddot{q} + C_1\dot{\theta} + c_{coul}\mathrm{sgn}(\dot{\theta}) = \tau(t) \tag{2.89a}$$

$$m_2\ddot{\theta} + M_3\ddot{q} + C_2\dot{q} + K_1 q - \dot{\theta}^2 K_2 q = 0 \tag{2.89b}$$

with the net tip position output

$$y = [\,h \;\; \Phi(h)\,]\begin{pmatrix} \theta \\ q \end{pmatrix} . \tag{2.89c}$$

It is important to understand the physical significance of Eq. (2.89) before proceeding with the derivation. Equation (2.89a) describes the various torques acting upon the hub. In the context of the implementation of an ideal position control loop, $\tau(t)$ is the control torque generated by an appropriate controller, and $\theta(t)$ is the actual hub position (which equals the desired hub position trajectory, $\theta_0(t)$). This idealized situation is facilitated by the use of a speed reducer that minimizes the coupling effect of the term $m_2^T\ddot{q}$ in Eq. (2.89a). Equation (2.89b) models the various forces that act upon the flexible arm. Since $\theta(t)$ is now considered as a system input, the terms $\dot{\theta}(t)$ and $\ddot{\theta}(t)$ are obviously the first and second derivatives of the input. With ideal hub position control, the equations of motion are written by rearranging Eq. (2.89b) such that the variable $q(t)$ and its derivatives appear on the left, and the derivatives of the input $\theta(t)$ appear on the right:

$$M_3\ddot{q} + C_2\dot{q} + K_1 q = \dot{\theta}^2 K_2 q - m_2\ddot{\theta} . \tag{2.90}$$

To facilitate simulation of the response of Eq. (2.90) to a given trajectory $\theta_0(t)$, it is advantageous to transform Eq. (2.90) to a form in which $\theta(t)$, and not its derivatives,

explicitly appears. To this end, choose as state variables:

$$\begin{aligned} z_1 &= q \\ z_2 &= \dot{z}_1 + M_3^{-1} m_2 \dot{\theta} \quad . \end{aligned} \tag{2.91}$$

Substituting Eq. (2.91) into Eq. (2.90) yields

$$\begin{aligned} \dot{z}_1 &= z_2 - M_3^{-1} m_2 \dot{\theta} \\ \dot{z}_2 &= M_3^{-1} \left(-K_1 z_1 - C_2 z_2 + C_2 M_3^{-1} m_2 \dot{\theta} + K_2 z_1 \dot{\theta}^2 \right) \quad . \end{aligned} \tag{2.92}$$

The net tip position is written

$$y = h\theta + [\phi_1(h) \;\; \phi_2(h) \;\; \ldots \;\; \phi_N(h)] z_1 \quad . \tag{2.93}$$

Equations (2.92) and (2.93) constitute the state-space form of the revised nonlinear model. Note the appearance of the first derivative of input $\theta(t)$, rather than the input itself. This inconsistency occurs because the nonlinear term $\dot{\theta}^2(t)$ makes it difficult to choose a set of state variables that would allow the input, and not its derivative, to explicitly appear. In spite of this alteration, simulation of the response of Eq's. (2.92) and (2.93) to a specific input trajectory $\theta(t)$ is readily achieved using **MATLAB's SIMULINK** block concept. (A differentiation block inserted prior to the block representing the above system transforms $\theta(t)$ to $\dot{\theta}(t)$ as required by Eq. (2.92)).

2.4.5 Local Linearization of the Revised Equations of Motion

Local linearization may be used to derive a linear model when nonlinearities are not severe. This linear model is an approximation of the nonlinear system in the neighbourhood of an operating point. Since the accuracy of the approximation deteriorates as the range of operation increases, the linearization is therefore local to its operating point.

Local linearization of the equations of motion described by Eq. (2.90) is performed to facilitate the controller design task, as will be explained in Chapter 3. The linearization is achieved using a Taylor series expansion of each term (see Appendix A for details). Only the linear parts in the expansion are kept. Specifying the operating point $\dot{\theta}_0 = \ddot{\theta}_0 = 0$ and $q_0 = \dot{q}_0 = \ddot{q}_0 = \mathbf{0}$ simplifies the calculations and essentially approximates the nonlinear

system as a manipulator that does not deflect, (a *rigid* manipulator), and whose hub velocity and hub acceleration are zero.

The linearized equations of motion are:

$$M_3\delta\ddot{q} + C_2\delta\dot{q} + K_1\delta q = -m_2\delta\ddot{\theta} \quad . \tag{2.94}$$

where δq, $\delta\dot{q}$, $\delta\ddot{q}$ and $\delta\ddot{\theta}$ denote small perturbations in q, $\dot{q}$, $\ddot{q}$ and $\ddot{\theta}$, respectively, about the operating point. The relationship between a variable, its operating point and its perturbed value is demonstrated for the case of $\ddot{\theta}(t)$ as follows.

Let

$$\ddot{\theta}(t) = \ddot{\theta}_0 + \delta\ddot{\theta}(t) \quad . \tag{2.95}$$

Premultiplying both sides of Eq. (2.94) by M_3^{-1} yields

$$\delta\ddot{q} + M_3^{-1}C_2\delta\dot{q} + M_3^{-1}K_1\delta q = -M_3^{-1}m_2\delta\ddot{\theta} \quad . \tag{2.96}$$

Substituting the state variables $v_1 = \delta q + M_3^{-1}m_2\delta\theta$ and $v_2 = \dot{v}_1 + M_3^{-1}C_2\delta q$ into Eq. (2.96) yields the perturbed state-space form:

$$\begin{aligned} \begin{pmatrix} \dot{v}_1 \\ \dot{v}_2 \end{pmatrix} &= \begin{pmatrix} -M_3^{-1}C_2 & I_N \\ -M_3^{-1}K_1 & 0_N \end{pmatrix}\begin{pmatrix} v_1 \\ v_2 \end{pmatrix} + \begin{pmatrix} M_3^{-1}C_2M_3^{-1}m_2 \\ M_3^{-1}K_1M_3^{-1}m_2 \end{pmatrix}\delta\theta \\ \delta y &= [\Phi(h) \quad 0_{1xN}]\begin{pmatrix} v_1 \\ v_2 \end{pmatrix} + (h - \Phi(h)M_3^{-1}m_2)\delta\theta \quad . \end{aligned} \tag{2.97}$$

Note the appearance of $\delta\theta$ in Eq. (2.97). This term occurs as part of the linearization process and does not appear in the original, nonlinear equation of motion (Eq. (2.90)). Requiring $\delta\theta$ to be small (as for the previous perturbed variables) constrains the system to operate about a single hub position. A controller based upon this restrictive scenario will obviously have limited usefulness; increasing the range of permissible values of $\delta\theta$, however, will degrade the validity of the linearization.

The variables $\delta\dot{\theta}$ and $\delta\ddot{\theta}$ appear during the linearization procedure: $\delta\theta$ does not occur. It is therefore postulated that the linearization will remain accurate for all values

of $\delta\theta$ that result in acceptably small ranges of operation for $\delta\dot{\theta}$ and $\delta\ddot{\theta}$. To sum up, it is theorized that the linearized model remains valid for large ranges of hub angle as long as the hub velocity and hub acceleration are not excessive.

Analysis of the Linearized Equations of Motion

To facilitate the use of frequency response methods of analysis, the linearized perturbed state-space equations of motion in Eq. (2.97) are transformed to the transfer function representation

$$G_t(s) = \frac{\Delta Y(s)}{\Delta\Theta(s)} = \frac{p(s)}{q(s)} \tag{2.98}$$

where $p(s)$ and $q(s)$ are polynomial functions of the Laplace variable s, and $\Delta Y(s)$ and $\Delta\Theta(s)$ are the Laplace tranforms of $\delta y(t)$ and $\delta\theta(t)$, respectively. The zeros and poles of $G_t(s)$ are simply the roots of $p(s)$ and $q(s)$, respectively. For the parameter values determined in Section 2.4.2,

$$\begin{aligned} p(s) &= 0.22850s^8 + 1.2385s^7 + 1.7828\times10^3 s^6 + 3.7317\times10^3 s^5 + 2.3179\times10^6 s^4 \\ &\quad -7.9107\times10^5 s^3 - 1.2344\times10^9 s^2 + 5.1552\times10^9 s + 1.0980\times10^{11} \\ q(s) &= s^8 + 9.4345s^7 + 1.3507\times10^4 s^6 + 7.8467\times10^4 s^5 + 3.3112\times10^7 s^4 \\ &\quad +1.1497\times10^8 s^3 + 1.0497\times10^{10} s^2 + 4.2960\times10^9 s + 9.1498\times10^{10} \ . \end{aligned} \tag{2.99}$$

The zeros and poles of $G_t(s)$ are shown in Table 2.2 and are plotted in Figure 2.24.

ZEROS	-1.87 ±77.0i	-1.12 ±47.9i	14.31 ±4.0i	-20.1	-8.0
POLES	-2.07 ±102.0i	-0.83 ±52.0i	-1.66 ±18.9i	-0.17 ±3.0i	

Table 2.2 Poles and zeros of $G_t(s)$.

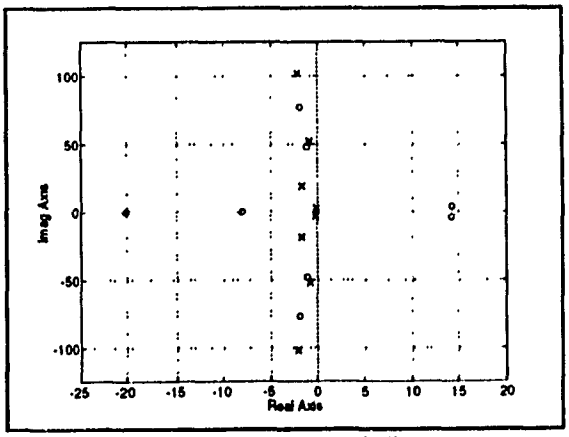

Figure 2.24 Pole-zero map of $G_t(s)$.

The Bode plot of $G_t(j\omega)$ appears in Figure 2.25. The peaks in the magnitude plot correspond to the poles, while the valleys correspond to the zeros. Note the sharpness of the valleys for frequencies above 40 rad/s which is caused by the proximity of the relevant zeros to the imaginary axis.

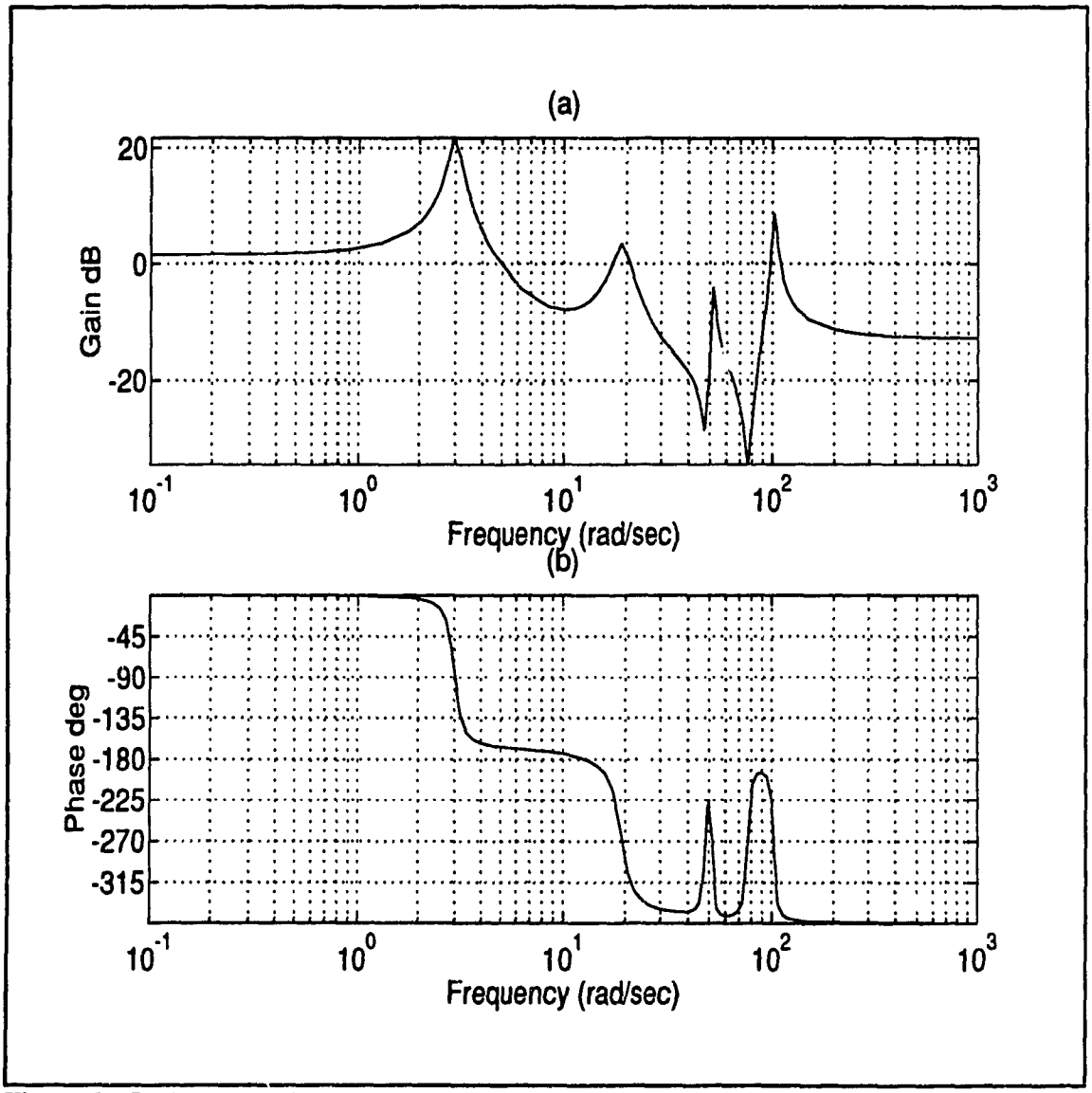

Figure 2.25 (a) Magnitude and (b) phase plots of $G_t(j\omega)$.

Minimum Phase and Nonminimum Phase Systems

Transfer functions without zeros in the right-half s-plane are termed *minimum phase* transfer functions. Transfer functions possessing zeros in the right-half s-plane are called

nonminimum phase transfer functions. The presence of right-half plane zeros identifies $G_t(s)$ as a nonminimum phase transfer function. For a minimum phase transfer function with numerator and denominator polynomials of degrees m and n, respectively, the phase angle at infinite frequency equals $-90°(n-m)$. The phase angle at infinite frequency differs from this value for a nonminimum phase system. For $G_t(s)$, $n=m=8$. For $G_t(s)$ to be minimum phase, its phase angle at infinite frequency would have to equal $-90°(n-m)=0°$. This is clearly not the case as can be seen in Figure 2.25b: the range of phase angle is not minimum and so the system is nonminimum phase.

Nonminimum phase is defined in the context of a system's frequency response. The excessive phase lag characteristic of nonminimum phase systems typically slows the transient response.

The reason for the nonminimum phase behaviour of $G_t(s)$ is that the flexible manipulator is a *non-colocated* system; the location of the actuator (at the hub) is not the same as that of the sensor (at the tip).

Zero Dynamics

The concepts of minimum phase and nonminimum phase linear systems are subsets of the more general notion of *zero dynamics* that applies to nonlinear systems. Consider the single input, single output nonlinear system with input u, output y and state vector z

$$\begin{aligned} \dot{z} &= \boldsymbol{f}(z,u) \\ y &= \boldsymbol{g}(z,u) \quad . \end{aligned} \tag{2.100}$$

The zero dynamics are found by setting $y = 0$. This constraint, in turn, restricts u and z. The dynamical system of Eq. (2.100) can be rewritten to describe the behaviour of the states when the output is forced to be zero by input u. This behaviour is termed the *zero dynamics* of the system. Depending on their initial values, the states may be unstable even though the output remains zero. In this situation the system is "internally" unstable and is said to have unstable zero dynamics.

Validation of the Linearized Model

A key factor during the derivation of the linearized model of Eq. (2.97) is the assumption that implementation of an ideal hub position control loop allows $\theta(t)$ and its derivatives to be considered as inputs. As an input, $\theta(t)$ is not influenced by the "disturbance" effects of the terms in Eq. (2.89a). Ideally, then, the dynamics of Eq. (2.89a) do not affect Eq. (2.89b). The behaviour of the flexible manipulator is therefore described by a nonlinear reduced-order model that involves only Eq. (2.89b). To more formally justify this line of reasoning, we begin by modeling the Coulomb friction by using a modified sigmoid function instead of the function $c_{coul}\text{sgn}(\dot{\theta})$. That is,

$$\text{Coulomb friction} = c_{coul}\left(\frac{2}{1+e^{-k\dot{\theta}}} - 1\right). \tag{2.101}$$

Unlike the signum function it replaces, the slope in the vicinity of $\dot{\theta} = 0$ is finite. This characteristic facilitates the approximation of Coulomb friction using a Taylor series expansion. The modified sigmoid function is plotted for various values of k in Figure 2.26.

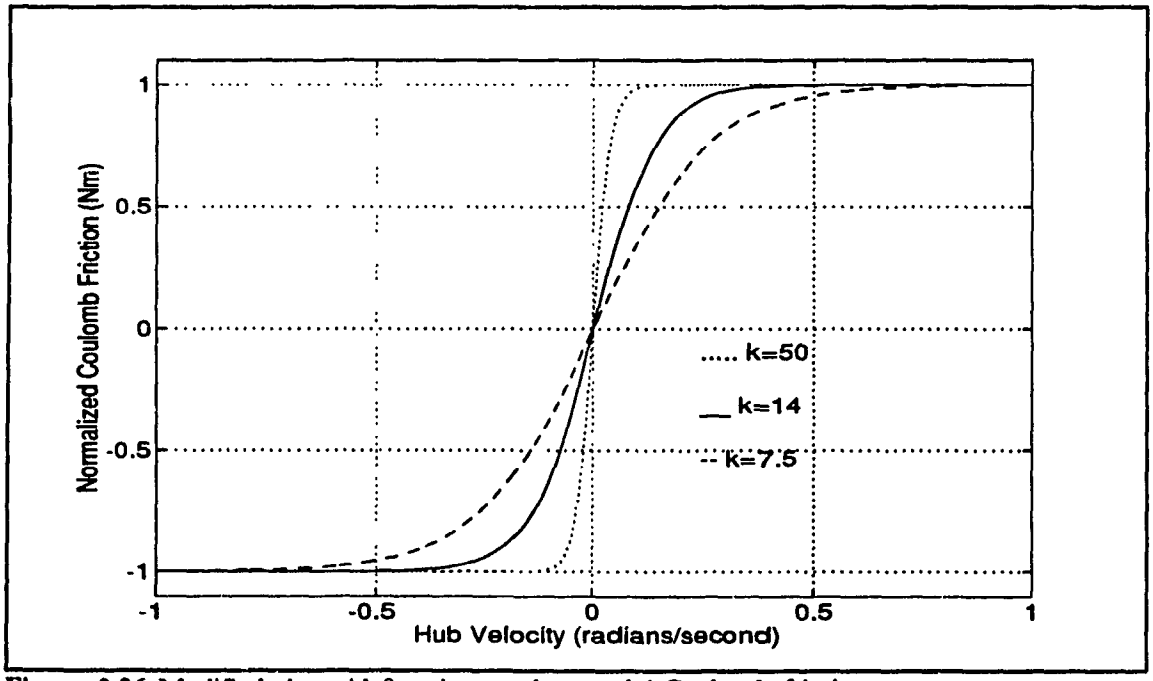

Figure 2.26 Modified sigmoid function used to model Coulomb friction.

Equation (2.89) is rewritten, substituting Eq. (2.101) for the Coulomb friction term.

$$m_1\ddot{\theta} + \boldsymbol{m}_2^T\ddot{\boldsymbol{q}} + C_1\dot{\theta} + c_{coul}\left(\frac{2}{1+e^{-k\dot{\theta}}} - 1\right) = \tau(t) \tag{2.102a}$$

$$\boldsymbol{m}_2\ddot{\theta} + \boldsymbol{M}_3\ddot{\boldsymbol{q}} + \boldsymbol{C}_2\dot{\boldsymbol{q}} + \boldsymbol{K}_1\boldsymbol{q} - \dot{\theta}^2\boldsymbol{K}_2\boldsymbol{q} = \boldsymbol{0} \quad . \tag{2.102b}$$

Consider the Taylor series expansion of Eq. (2.102) about the operating point $\boldsymbol{q}_0 = \dot{\boldsymbol{q}}_0 = \ddot{\boldsymbol{q}}_0 = \boldsymbol{0}$, $\dot{\theta}_0$ and $\ddot{\theta}_0$ (see Appendix B). Unlike the previous linearization in Section 2.4.5, the nominal hub velocity and acceleration are not set to 0. The nominal system that corresponds to this particular choice of operating point is an arm that rotates with hub velocity $\dot{\theta}_0$ and acceleration $\ddot{\theta}_0$ but undergoes no deflection, hence, a *rigid* arm.

As a result of its Taylor series expansion, Eq. (2.102) can be partitioned into a nominal equation of motion (Eq. (2.103)) and a set of linear perturbed equations of motion (Eq. (2.104)).

$$b\dot{\theta}_0 + c_{coul}\left(\frac{2}{1+e^{-k\dot{\theta}_0}} - 1\right) = \tau_0 \tag{2.103}$$

$$m_1(\boldsymbol{q}_0)\delta\ddot{\theta} + \boldsymbol{m}_2^T\delta\ddot{\boldsymbol{q}} + b\delta\dot{\theta} + \frac{2kc_{coul}e^{-k\dot{\theta}_0}}{(1+e^{-k\dot{\theta}_0})^2}\delta\dot{\theta} = \delta\tau \tag{2.104a}$$

$$\boldsymbol{m}_2\delta\ddot{\theta} + \boldsymbol{M}_3\delta\ddot{\boldsymbol{q}} + \boldsymbol{C}_2\delta\dot{\boldsymbol{q}} + \boldsymbol{K}_1\delta\boldsymbol{q} - \dot{\theta}_0^2\boldsymbol{K}_2\delta\boldsymbol{q} = \boldsymbol{0} \; . \tag{2.104b}$$

Equations (2.103) and (2.104) can be used to develop a scheme for the control of the hub angle position. Figure 2.27 illustrates the strategy.

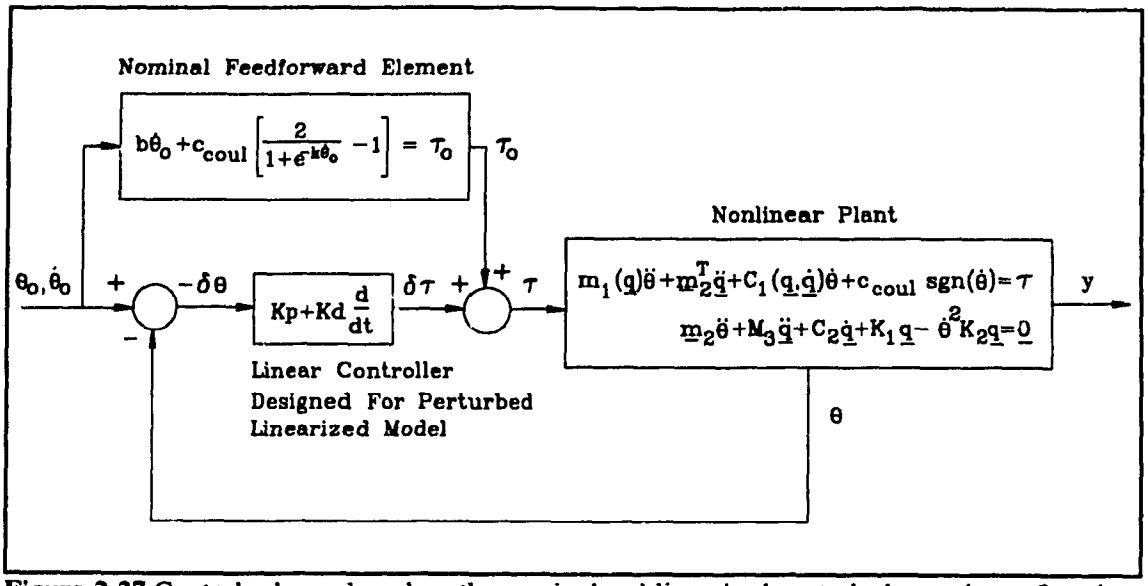

Figure 2.27 Control scheme based on the nominal and linearized perturbed equations of motion.

The control torque τ applied to the plant is the sum of the nominal control torque τ_0 and the perturbed control torque $\delta\tau$. The nominal control torque τ_0 is computed by specifying the desired trajectory for $\dot{\theta}_0$ in Eq. (2.103). In the absence of any perturbed plant dynamics, τ_0 would cause the actual hub angle, θ, to precisely track the nominal trajectory θ_0. To achieve good tracking control in the presence of the plant perturbations (approximated by the linear model of Eq. (2.104)), a linear controller is implemented. This controller, (shown as a proportional plus derivative control in Figure 2.27), acts on the tracking error ($-\delta\theta$) and generates a perturbed control torque $\delta\tau$ that drives the tracking error to zero in a prescribed fashion. This scheme will only succeed when the range of operation of the nonlinear system is restricted to a region close to the operating point, because of the linearized approximation of the perturbed plant dynamics.

The motivation for developing the control scheme of Figure 2.27 is that it will be used to demonstrate the validity of Eq. (2.97). Specifically, if the coefficients in Eq. (2.104a) satisfy certain criteria, (which are defined below), and for $\dot{\theta}_0 = 0$, it will be

shown that the equations describing the closed-loop system of Figure 2.27 simplify to Eq. (2.94), the linear equation of motion upon which the state space representation of Eq. (2.97) is based.

As described above, the PD controller has been designed for the linearized perturbed dynamics of the nonlinear plant, and drives the perturbed hub angle to zero. The equations of motion for the perturbed closed-loop system will now be computed.

From inspection of Figure 2.27, torque $\delta\tau$ is written

$$\delta\tau = -K_p\delta\theta - K_d\delta\dot{\theta} \; . \tag{2.105}$$

Substituting Eq. (2.105) into Eq. (2.104a) and rearranging terms yields the closed-loop equations of motion

$$m_1(q_0)\,\delta\ddot{\theta} + \boldsymbol{m}_2^T\delta\ddot{\boldsymbol{q}} + \left[b + K_d + \frac{2kc_{coul}e^{-k\dot{\theta}_0}}{(1+e^{-k\dot{\theta}_0})^2}\right]\delta\dot{\theta} + K_p\delta\theta = 0 \tag{2.106a}$$

$$\boldsymbol{m}_2\delta\ddot{\theta} + \boldsymbol{M}_3\delta\ddot{\boldsymbol{q}} + \boldsymbol{C}_2\delta\dot{\boldsymbol{q}} + [\boldsymbol{K}_1 - \dot{\theta}_0^2\boldsymbol{K}_2]\delta\boldsymbol{q} = \boldsymbol{0} \; . \tag{2.106b}$$

Substituting $\dot{\theta}_0 = 0$ into Eq. (2.103) yields $\tau_0 = 0$. Equation (2.106) is rewritten as

$$m_1\delta\ddot{\theta} + \boldsymbol{m}_2^T\delta\ddot{\boldsymbol{q}} + \left[b + K_d + f_{coul}\right]\delta\dot{\theta} + K_p\delta\theta = 0 \tag{2.107a}$$

$$\boldsymbol{m}_2\delta\ddot{\theta} + \boldsymbol{M}_3\delta\ddot{\boldsymbol{q}} + \boldsymbol{C}_2\delta\dot{\boldsymbol{q}} + \boldsymbol{K}_1\delta\boldsymbol{q} = \boldsymbol{0} \tag{2.107b}$$

where $f_{coul} = 0.5kc_{coul}$ and the explicit dependence of m_1 on q_0 has been suppressed for brevity.

The closed-loop system of Figure 2.27 is described by Eq. (2.107) for $\dot{\theta}_0 = 0$. The next phase is to demonstrate that the closed-loop system can be described by Eq. (2.94), that is, to verify the progression from Eq. (2.107) to Eq. (2.94). This verification requires justifying that $\delta\theta$ and its derivatives may be considered as inputs. This assumption implies that the rigid body modes, (corresponding to $\delta\theta$ and $\delta\dot{\theta}$), are not influenced by the flexible modes, (corresponding to $\delta\boldsymbol{q}$ and $\delta\dot{\boldsymbol{q}}$). In other words, the rigid body modes and the flexible modes must be *decoupled.*

Rigid Body Dynamics

The numerical values for the parameters m_1, $\boldsymbol{m}_2^T$ and b of Eq. (2.107a) are determined from the parameter values of Section 2.4.2. Gains K_p and K_d were determined experimentally by applying a reference hub angle input to the closed-loop system. The gains were adjusted so that the hub angle output response was slightly overdamped. These specific values of K_p and K_d therefore result in good tracking of the reference hub angle trajectory and are able to decouple the rigid body modes from the flexible modes. Of the two parameters required to compute f_{coul}, c_{coul} is found in Section 2.4.2. In accordance with the experimental observations, the constant k was computed so that the eigenvalues corresponding to the rigid body modes of the linearized closed-loop system of Eq. (2.107) are slightly overdamped. The numerical values for these parameters are shown below.

$$m_1 = 0.996 \qquad \boldsymbol{m}_2 = [0.903 \;\; 0.181 \;\; -0.016 \;\; 0.097]^T$$
$$b = 1.37 \quad f_{coul} = 33.25 \quad k = 14.0 \quad K_d = 25 \quad K_p = 3000 \quad .$$

To investigate the conditions for which the assumption of decoupling is justified, we begin by substituting $f_v = (b + K_d + f_{coul})$ in Eq. (2.107a) to get

$$m_1 \delta\ddot{\theta} + \boldsymbol{m}_2^T \delta\ddot{\boldsymbol{q}} + f_v \delta\dot{\theta} + K_p \delta\theta = 0 \; . \tag{2.108}$$

It is obvious from Eq. (2.108) that the system is decoupled if the magnitude of the term $\boldsymbol{m}_2^T \delta\ddot{\boldsymbol{q}}$, (the inertia torque exerted on the hub by the flexible system modes), is sufficiently small with respect to the other terms. To quantify the situation, we introduce the positive scaling factor $\varepsilon \ll 1$ and rewrite the parameters m_1, f_v and K_p as functions of ε as follows:

$$m_1 = \frac{\overline{m}_1}{\varepsilon} \qquad f_v = \frac{\overline{f}_v}{\varepsilon^2} \qquad K_p = \frac{\overline{K}_p}{\varepsilon^4} \; . \tag{2.109}$$

Substituting Eq. (2.109) into Eq. (2.108) yields

$$\frac{\overline{m_1}}{\varepsilon}\delta\ddot{\theta} + \boldsymbol{m}_2^T\delta\ddot{\boldsymbol{q}} + \frac{\overline{f_v}}{\varepsilon^2}\delta\dot{\theta} + \frac{\overline{K_p}}{\varepsilon^4}\delta\theta = 0 . \tag{2.110}$$

Multiply both sides of Eq. (2.110) by ε^4 to give

$$\varepsilon^3\overline{m_1}\delta\ddot{\theta} + \varepsilon^4\boldsymbol{m}_2^T\delta\ddot{\boldsymbol{q}} + \varepsilon^2\overline{f_v}\delta\dot{\theta} + \overline{K_p}\delta\theta = 0 . \tag{2.111}$$

If ε is chosen so that $\overline{m_1}$, $\overline{f_v}$ and $\overline{K_p}$ are of the same order of magnitude, all terms of order ε^4 and higher in Eq. (2.111) are significantly smaller than the lower order terms. Equation (2.111) is approximated by

$$\varepsilon^3\overline{m_1}\delta\ddot{\theta} + \varepsilon^2\overline{f_v}\delta\dot{\theta} + \overline{K_p}\delta\theta = 0 . \tag{2.112}$$

Equation (2.112) is the scaled *rigid body* dynamics and can also be derived by multiplying Eq. (2.108) by ε^4 and subsequently discarding terms of order ε^4 and higher. What makes the particular format of Eq. (2.112) useful is that it quantifies the approximation process by portraying the coefficients of the perturbed state variables as products of a constant and a power of ε. Since all the constants are of the same order of magnitude, the decision as to which terms to neglect is based on ε. Furthermore, the accuracy of the approximation improves as the magnitude of ε is decreased.

The Laplace transform of Eq. (2.112) is

$$\varepsilon^3\overline{m_1}[s^2\Delta\Theta(s) - s\delta\theta(0) - \delta\dot{\theta}(0)] + \varepsilon^2\overline{f_v}[s\Delta\Theta(s) - \delta\theta(0)] + \overline{K_p}\Delta\Theta(s) = 0 \tag{2.113}$$

where $\Delta\Theta(s)$ is the Laplace transform of $\delta\theta(t)$. Solving for $\Delta\Theta(s)$ gives

$$\Delta\Theta(s) = \frac{\delta\theta(0)(\varepsilon^3\overline{m_1}s + \varepsilon^2\overline{f_v})}{\varepsilon^3\overline{m_1}s^2 + \varepsilon^2\overline{f_v}s + \overline{K_p}} + \frac{\delta\dot{\theta}(0)\varepsilon^3\overline{m_1}}{\varepsilon^3\overline{m_1}s^2 + \varepsilon^2\overline{f_v}s + \overline{K_p}} . \tag{2.114}$$

The roots of the denominator polynomial of Eq. (2.114) are the eigenvalues of the system of Eq. (2.112).

Choosing $\varepsilon = 0.1351$ and using the previously determined numerical values for m_1, f_v and K_p in Eq. (2.109) results in the following values for $\overline{m_1}$, $\overline{f_v}$ and $\overline{K_p}$:

$$\overline{m_1} = 0.1346 \quad \overline{f_v} = 1.0882 \quad \overline{K_p} = 0.9994 \quad . \tag{2.115}$$

Note that $\overline{f_v}$ and $\overline{K_p}$ are both of order 1 magnitude while $\overline{m_1}$ is of order ε. This disparity occurs because of the relatively small magnitude of m_1. Although the accuracy of the approximation is diminished, the analysis is continued because it will yield some useful results.

Solving for the roots of the denominator of Eq. (2.114) using $\varepsilon = 0.1351$ and Eq. (2.115) yields the poles of the rigid body dynamics of the decoupled system that approximates Eq. (2.107)

$$s_r = -29.9 \pm 46.0i \quad .$$

Flexible Dynamics

Assuming that the rigid body modes and the flexible modes are decoupled, the flexible dynamics do not affect the rigid body dynamics. The term $m_2\delta\ddot{\theta}$ in Eq. (2.107b) can then be considered as an input and brought to the right side of the equation. The resulting expression is equal to Eq. (2.94), the linear equation of motion upon which the state space representation of Eq. (2.97) is based. The poles of the flexible dynamics equal the poles of transfer function $G_i(s)$ listed in Table 2.2 and are repeated here for convenience:

$$s_f = -2.07 \pm 102.0i, \ -0.83 \pm 52.0i, \ -1.66 \pm 18.9i, \ -0.17 \pm 3.0i \quad .$$

Accuracy of the Decoupled Approximation of Equation 2.107

The full-order system of Eq. (2.107) has been approximated by decoupling the rigid body and flexible dynamics, yielding two reduced-order systems. The accuracy of this approximation can be assessed by measuring the similarity of the poles s_r and s_f, to the eigenvalues of Eq. (2.107).

Table 2.3 Poles of the full-order system of Eq. (2.107) and its decoupled approximation.

	System of Eq. (2.107)	Decoupled Approximation
Flexible Modes	-2.77 ± 101.9	-2.07 ± 102.0i
	-0.83 ± 52.0i	-0.83 ± 52.0i
	-1.66 ± 18.9i	-1.66 ± 18.9i
	-0.17 ± 3.0i	-0.17 ± 3.0i
Rigid Body Modes	-121.7 -86.8	-29.9 ± 46.0i

Table 2.3 reveals that the flexible modes are in relatively close agreement with the only noticeable discrepancy occuring for the real parts of the highest order modes. The rigid body modes, however, exhibit a gross deviation. Obviously, approximating the system of Eq. (2.107) by neglecting the coupling effect of the term $m_2^T \delta\ddot{q}$ does not yield an accurate description of the rigid body dynamics.

It is instructive to examine further the effect of m_2 on the accuracy of the approximation. Table 2.4 displays the poles of the full-order system of Eq. (2.107) for various values of m_2. As the magnitude of m_2 decreases, the poles of the full-order system approach the poles of the reduced-order flexible and rigid body systems.

Table 2.4 Poles of the full-order system of Eq. (2.107) for various values of m_2.

	m_2	$0.75m_2$	$0.5m_2$	$0.1m_2$
Flexible Modes	-2.76±101.9	-2.38±102.1i	-2.12±102.0i	-2.07±102.0i
	-0.83±52.0i	-0.83±52.0i	-0.83±52.0i	-0.83±52.0i
	-1.66±18.9i	-1.66±18.9i	-1.66±18.9i	-1.66±18.9i
	-0.17±3.0i	-0.17±3.0i	-0.17±3.0i	-0.17±3.0i
Rigid Body Modes	-121.7 -86.8	-49.8±50.5i	-33.2±47.4i	-30.0±46.0i

Since m_2^T is proportional to γ, (the density of the arm), the accuracy of the approximation

improves as the magnitude of γ decreases.

In view of the fact that the poles of the reduced-order rigid body system are substantially different from the rigid body modes of the full-order system, it may appear that there is no justification for decoupling the system and that Eq's. (2.94) and (2.97) are invalid. The significant factor is that although the approximation underestimates the magnitudes of the real parts of the rigid body poles and exaggerates their imaginary parts, the magnitudes of the real parts are still more than ten times those of any flexible mode. This means that the rigid body modes decay much more rapidly than the flexible modes, and are insignificant with respect to the transient response of the complete system. The full-order system can therefore be accurately approximated by the dominant, (i.e., flexible), modes of the system.

Inexact decoupling, however, may have a disturbance effect that can excite the flexible modes. If this disturbance effect is not suppressed by the controller, the result nay be a degradation of control performance.

Further Verification Using Simulated and Experimental Data

Further verification of the model of Eq. (2.97) is achieved by demonstrating that:

(i) it accurately approximates the complete nonlinear model of Eq. (2.89), and

(ii) its response agrees with that of the test-bed with hub position control, when both are subjected to the same hub angle trajectory.

Comparison of the Simulated Responses of Equations (2.89) and (2.97)

Step (i) is achieved by solving Eq. (2.89) for a reference input torque $\tau(t)$ and recording the resulting hub angle and the output (the net tip position) trajectories. The hub angle trajectory is used as input $\delta\theta$ in Eq. (2.97), which is then solved for the linear output trajectory. A good agreement between the linear and nonlinear output trajectories

indicates that Eq. (2.97) is a good approximation of the full-order, nonlinear model.

Figure 2.29 is the hub angle trajectory that results from solving Eq. (2.89) for the torque $\tau(t)$ shown in Figure 2.28. Figures 2.30 and 2.31 compare the net tip positions obtained from solving Eq. (2.97) and Eq. (2.89), respectively. The excellent agreement is evidence that Eq. (2.97) is a good approximation of Eq. (2.89).

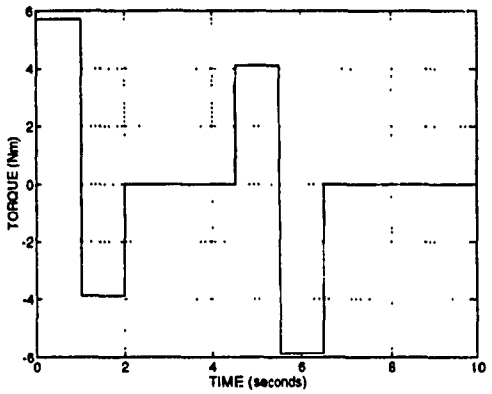

Figure 2.28 Input torque $\tau(t)$ applied to Eq. (2.89).

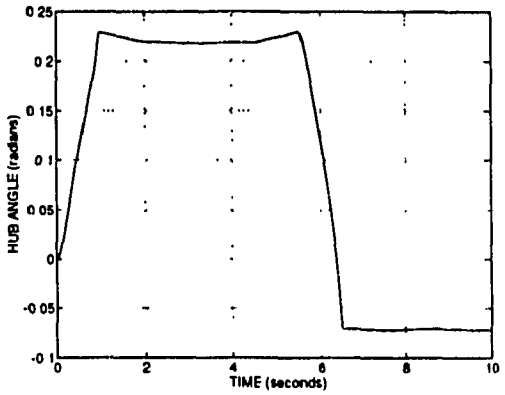

Figure 2.29 Hub angle $\theta(t)$ trajectory obtained from solving Eq. (2.89) and applied to Eq. (2.97).

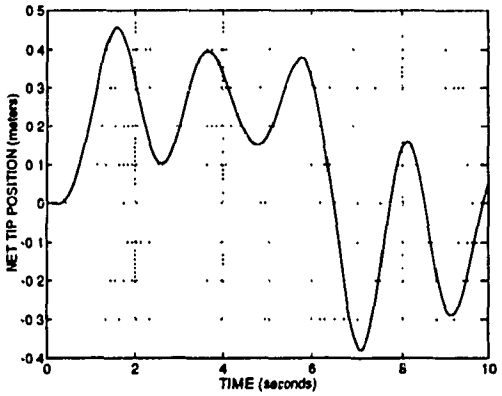

Figure 2.30 Net tip position $\delta y = h\delta\theta(t) + \delta w(h,t)$ obtained from solving Eq. (2.97).

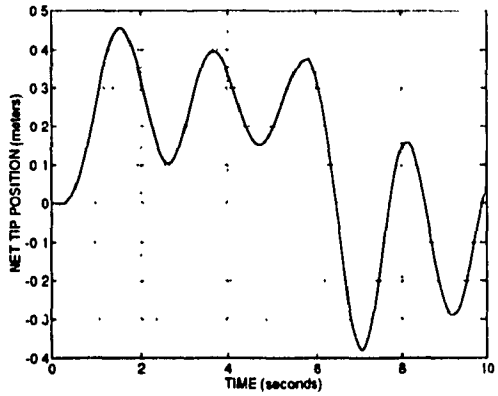

Figure 2.31 Net tip position $y = h\theta(t) + w(h,t)$ obtained from solving Eq. (2.89).

Comparison of the Simulated Response of Equation (2.97) With Experimental Data

Step (ii) involves verifying the accuracy of the model by comparing its response with that of the experimental test-bed using hub position control. Implementation of the

control scheme of Figure 2.27 on the test-bed with the specific time varying trajectories $\theta_0(t)$ and $\dot{\theta}_0(t)$ requires on-line computation of the feedforward element to generate τ_0. An accurate value for τ_0 is difficult to achieve because c_{coul} is not known with any degree of certainty. Another factor that complicates the direct realization of the controller is that the perturbed linearized model can no longer be considered a time invariant system, since it is a function of the time-varying quantity $\dot{\theta}_0(t)$. Gains K_p and K_d must, therefore, also vary with time in order maintain the system's poles at their desired locations. Although gain scheduling reduces the computational burden by storing gain values off line, the system's nominal trajectories must be known *a priori*. For the present application, the objective is to control the position of the tip. Trajectory $y_{ref}(t)$ is therefore known, but $\dot{\theta}_0(t)$ is not, and gain scheduling is not a viable option.

A simplifying assumption involves specifying $\dot{\theta}_0(t) = 0$ in Figure 2.27. The linearized perturbed system is then time-invariant, (resulting in constant gains K_p and K_d), and the nominal feedforward element is zero. The schematic diagram of Figure 2.32 illustrates the test-bed's PD hub position control system.

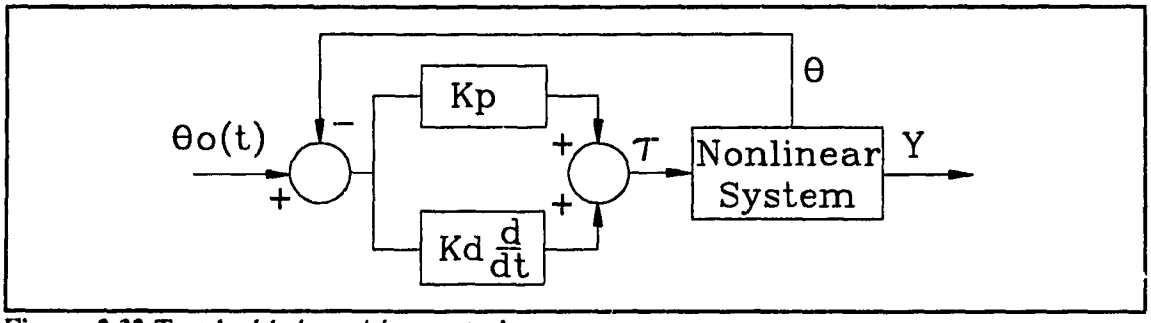

Figure 2.32 Test-bed hub position control system.

Effects of A Time-Varying Trajectory $\dot{\theta}_0(t)$

The simplifications inherent in Figure 2.32 may appear unreasonable because they are based on the assumption that $\dot{\theta}_0(t) = 0$ which implies that $\theta_0(t)$ is constant. As will be explained in Chapter 3, $\theta_0(t)$ cannot be directly specified *a priori* because it is

generated by an external control loop. No prior assumptions can therefore be made concerning $\theta_0(t)$, except that its first and second derivatives will be nonzero. It is therefore of interest to examination the ramifications of the nonzero trajectories $\dot{\theta}_0(t)$ and $\ddot{\theta}_0(t)$ for the control system of Figure 2.32.

From inspection of Figure 2.32, control torque $\tau(t)$ is written

$$\tau(t) = K_p[\theta_0(t) - \theta(t)] + K_d[\dot{\theta}_0(t) - \dot{\theta}(t)] \ . \tag{2.116}$$

Assuming that $\theta(t)$ and $\dot{\theta}(t)$ track $\theta_0(t)$ and $\dot{\theta}_0(t)$, respectively, with small perturbations, Eq. (2.116) becomes

$$\tau(t) = -K_p\delta\theta(t) - K_d\delta\dot{\theta}(t) \ . \tag{2.117}$$

As described in Appendix B, each term of the model of the nonlinear system of Figure 2.32, (Eq. 2.102), may be approximated as the sum of a nominal term and a linear, perturbed term. (Even though only $\theta_0(t)$ and its derivatives are expressly defined in Figure 2.32, their existence implies the existence of nominal trajectories $\boldsymbol{q}_0(t)$, $\dot{\boldsymbol{q}}_0(t)$ and $\ddot{\boldsymbol{q}}_0(t)$. The relationship between the nominal trajectories is defined by Eq. (B.11)). From Eq's. (B.11) and (B.12), the approximate equations of motion for the nonlinear system, (with $M_p = 0$), are:

$$\begin{aligned} m_1(\boldsymbol{q}_0)\delta\ddot{\theta} + \boldsymbol{m}_2^T\delta\ddot{\boldsymbol{q}} + \left[C_1(\boldsymbol{q}_0,\dot{\boldsymbol{q}}_0) + \frac{2kc_{coul}e^{-k\theta_0}}{(1+e^{-k\theta_0})^2}\right]\delta\dot{\theta} + 2\dot{\theta}_0\gamma\boldsymbol{q}_0^T\,\delta\dot{\boldsymbol{q}} \\ + 2\gamma(\ddot{\theta}_0\boldsymbol{q}_0^T + \dot{\theta}_0\dot{\boldsymbol{q}}_0^T)\delta\boldsymbol{q} + m_1(\boldsymbol{q}_0)\ddot{\theta}_0 + \boldsymbol{m}_2^T\ddot{\boldsymbol{q}}_0 + C_1(\boldsymbol{q}_0,\dot{\boldsymbol{q}}_0)\dot{\theta}_0 \\ + c_{coul}\left(\frac{2}{1+e^{-k\theta_0}} - 1\right) = \tau \end{aligned} \tag{2.118a}$$

$$m_2\delta\ddot{\theta} + M_3\delta\ddot{q} - 2\dot{\theta}_0 K_2 q_0 \delta\dot{\theta} + C_2\delta\dot{q} + [K_1 - \dot{\theta}_0^2 K_2]\delta q$$
$$+ m_2\ddot{\theta}_0 + M_3\ddot{q}_0 + C_2\dot{q}_0 + K_1 q_0 - \dot{\theta}_0^2 K_2 q_0 = 0 \quad . \tag{2.118b}$$

Substituting Eq. (2.117) into Eq. (2.118a) and rearranging terms yields the following expression for the closed-loop system of Figure 2.32:

$$m_1(q_0)\delta\ddot{\theta} + m_2^T\delta\ddot{q} + f_v(\dot{\theta}_0, q_0, \dot{q}_0)\delta\dot{\theta} + 2\dot{\theta}_0\gamma q_0^T\delta\dot{q} + 2\gamma(\ddot{\theta}_0 q_0^T + \dot{\theta}_0\dot{q}_0^T)\delta q$$
$$+ K_p\delta\theta = -\left[m_1(q_0)\ddot{\theta}_0 + m_2^T\ddot{q}_0 + C_1(q_0,\dot{q}_0)\dot{\theta}_0 + c_{coul}\left(\frac{2}{1+e^{-k\dot{\theta}_0}} - 1\right)\right] \tag{2.119a}$$

$$M_3\delta\ddot{q} + C_2\delta\dot{q} + [K_1 - \dot{\theta}_0^2 K_2]\delta q$$
$$= 2\dot{\theta}_0 K_2 q_0\delta\dot{\theta} - m_2\delta\ddot{\theta} - [m_2\ddot{\theta}_0 + M_3\ddot{q}_0 + C_2\dot{q}_0 + K_1 q_0 - \dot{\theta}_0^2 K_2 q_0] \tag{2.119b}$$

where

$$f_v(\dot{\theta}_0, q_0, \dot{q}_0) = K_d + C_1(q_0,\dot{q}_0) + \frac{2kc_{coul}e^{-k\dot{\theta}}}{(1+e^{-k\dot{\theta}})^2} \quad .$$

Following the same procedure as for Eq. (2.107a), Eq. (2.119a) may be scaled if the magnitudes of the coefficients $m_1(q_0)$, $f_v(\dot{\theta}_0, q_0, \dot{q}_0)$ and K_p are sufficiently large. Using the positive scaling factor $\varepsilon \ll 1$, rewrite Eq. (2.119a) as follows:

$$\varepsilon^3\overline{m_1}(q_0)\delta\ddot{\theta} + \varepsilon^2\overline{f_v}(\dot{\theta}_0, q_0, \dot{q}_0)\delta\dot{\theta} + \varepsilon^4 m_2^T\delta\ddot{q} + 2\varepsilon^4\dot{\theta}_0\gamma q_0^T\delta\dot{q} + 2\varepsilon^4\gamma(\ddot{\theta}_0 q_0^T + \dot{\theta}_0\dot{q}_0^T)\delta q$$
$$+ \overline{K_p}\delta\theta = -\varepsilon^3\overline{m_1}(q_0)\ddot{\theta}_0 - \varepsilon^4\left[m_2^T\ddot{q}_0 + C_1(q_0,\dot{q}_0)\dot{\theta}_0 + c_{coul}\left(\frac{2}{1+e^{-k\dot{\theta}_0}} - 1\right)\right] \tag{2.120}$$

where, as before,

$$m_1 = \frac{\overline{m}_1}{\varepsilon} \qquad f_v = \frac{\overline{f}_v}{\varepsilon^2} \qquad K_p = \frac{\overline{K}_p}{\varepsilon^4} \quad . \tag{2.121}$$

Discarding all terms of order ε^4 and higher yields

$$\varepsilon^3\overline{m_1}(q_0)\delta\ddot{\theta} + \varepsilon^2\overline{f_v}(\dot{\theta}_0, q_0, \dot{q}_0)\,\delta\dot{\theta} + \overline{K_p}\delta\theta = -\varepsilon^3\overline{m_1}(q_0)\ddot{\theta}_0 \quad . \tag{2.122}$$

Equation (2.122) demonstrates that the closed-loop rigid body dynamics are decoupled from the flexible dynamics. The fact that the equation is nonhomogeneous, however, means that $\delta\theta$ and its derivatives are nonzero. The hub angle $\theta(t)$ will not track the nominal trajectory $\theta_0(t)$ with zero error, except when $\ddot{\theta}_0(t) = 0$. Nevertheless, this error can be made small by restricting the magnitude of $\ddot{\theta}_0(t)$.

Coefficients $\overline{m_1}$ and $\overline{f_v}$ are functions of the time-dependent nominal trajectories $q_0(t)$, and $\dot{\theta}_0(t)$, $q_0(t)$ and $\dot{q}_0(t)$, respectively. Thus, Eq. (2.122) is time varying and the locations of the closed-loop poles of the rigid body dynamics change with time. Since the gains K_p and K_d have been designed for a time invariant system, the closed-loop hub angle tracking performance will not be consistent.

To examine the effects of the nonzero trajectories $\dot{\theta}_0(t)$ and $\ddot{\theta}_0(t)$ on the flexible dynamics, note that the bracketed term on the right-hand side of Eq. (2.119b) equals zero (as defined in Eq. (B.11b)). Assuming that the rigid body and flexible modes are decoupled, Eq. (2.119b) is rewritten as

$$M_3\delta\ddot{q} + C_2\delta\dot{q} + [K_1 - \dot{\theta}_0^2 K_2]\delta q = 2\dot{\theta}_0 K_2 q_0 \delta\dot{\theta} - m_2\delta\ddot{\theta} \quad . \tag{2.123}$$

This expression differs from Eq. (2.107b) by the coefficient $-\dot{\theta}_0^2 K_2$ and the input term $2\dot{\theta}_0 K_2 q_0 \delta\dot{\theta}$. In the context of the closed-loop system of Figure 2.32, the term $2\dot{\theta}_0 K_2 q_0 \delta\dot{\theta}$ acts as a disturbance input whose effect is minimal if the magnitudes of $\dot{\theta}_0(t)$ and q_0 are small. The coefficient $-\dot{\theta}_0^2 K_2$ exerts a time-varying influence upon the eigenvalues of the flexible dynamics. As the magnitude of $\dot{\theta}_0(t)$ increases, these eigenvalues become less damped and, ultimately, become unstable. This behaviour occurs

when the magnitudes of the elements of the centrifugal force vector $-\dot{\theta}_0^2 \boldsymbol{K}_2 \delta \boldsymbol{q}$ are larger than the magnitudes of the corresponding elements of the stiffness force vector $\boldsymbol{K}_1 \delta \boldsymbol{q}$. For the parameter values of Section 2.4.2, instability of the lowest order flexible mode occurs for $\dot{\theta}_0(t) \geq 3.0$ radians per second.

To recapitulate, when a time-varying nominal trajectory $\dot{\theta}_0(t)$ is input to the closed-loop system of Figure 2.32, accurate tracking of the hub angle is possible only for: (i) large values of the coefficients $m_1(\boldsymbol{q}_0)$, $f_v(\dot{\theta}, \boldsymbol{q}_0, \dot{\boldsymbol{q}}_0)$ and K_p, and (ii) small magnitudes of the nominal trajectory $\ddot{\theta}_0(t)$. Furthermore, the rigid body dynamics become time-varying and the constant gains K_p and K_d will not yield uniform tracking performance. As a result of centrifugal forces acting upon the arm, the flexible dynamics also become time-varying. For sufficiently large $\dot{\theta}_0(t)$, the flexible dynamics eventually become unstable. An input disturbance force proportional to the product $\dot{\theta}_0(t)\boldsymbol{q}_0(t)$ is also present. From this discussion, it is obvious that as the magnitude of $\dot{\theta}_0(t)$ increases: (i) hub angle tracking performance degrades, and (ii) the accuracy of the model of Eq. (2.107b), (and therefore Eq. (2.97)), declines.

Simulated and Experimental Results

The reference position trajectory, $\theta_0(t)$ (see Figure 2.33), consists of a set of linear paths with parabolic blends. Neither $\theta_0(t)$ nor $\dot{\theta}_0(t)$ possesses any discontinuities, so $\ddot{\theta}_0(t)$ remains finite as does the control torque, $\tau(t)$. Appropriate selection of controller gains K_p and K_d, as well as $\ddot{\theta}_0(t)$ for the various parabolic blends ensures that torque saturation does not occur. A proportional gain K_p of 3000 and a derivative gain K_d equalling 25 ensure slightly overdamped tracking of $\theta_0(t)$.

Figure 2.33 illustrates the close agreement between the simulated and experimental hub angles, thereby confirming the precision of the PD hub controller. The tip deflection is shown in Figure 2.34. Note that until $t \approx 7s$ the peak amplitudes of the experimental

curve are greater than those of the simulated plot. This behaviour is a result of the linearly decaying response that is characteristic of the Coulomb friction present in the test-bed and of the exponentially decaying response characteristic of the viscous damping used in the model. Good agreement for the output is demonstrated in Figure 2.35. The main reason for the relatively minor disparity is once again due to the different effects of Coulomb friction and viscous damping. The control torque $\tau(t)$ is shown in Figure 2.36 and is within the saturation limits of ±34.7 Nm.

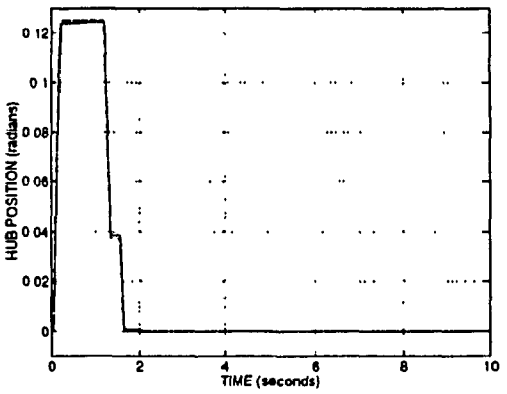

Figure 2.33 Desired hub angle $\theta_0(t)$ (dashed) and experimental hub angle $\theta(t)$ (solid).

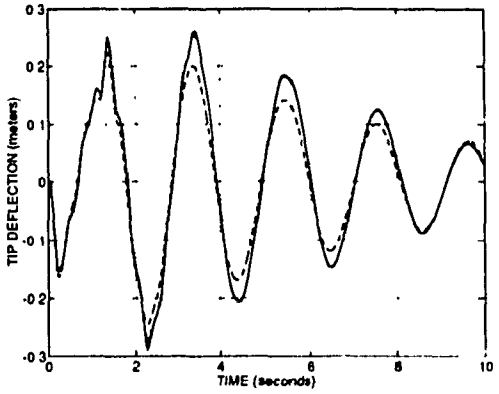

Figure 2.34 Simulated tip deflection $\delta w(h,t)$ (dashed) and experimental tip deflections $w(h,t)$ (solid).

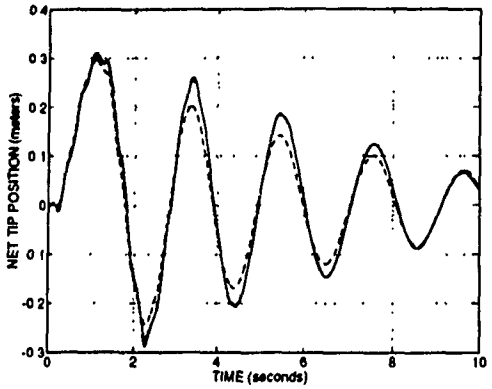

Figure 2.35 Simulated net tip position δy (dashed) and experimental net tip position y (solid).

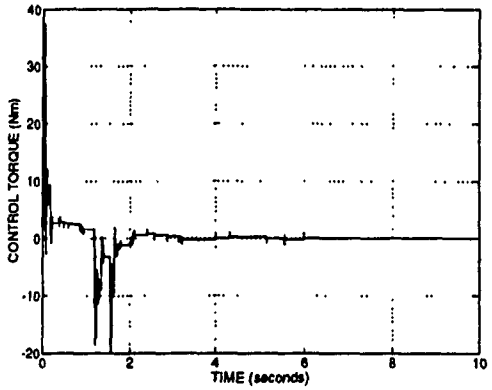

Figure 2.36 Experimental control torque $\tau(t)$.

The above analysis demonstrates that Eq. (2.97) reasonably approximates the actual system and is a suitable model for the design of a controller, which is the subject of the next chapter.

Chapter 3

Controller Design

3.1 Introduction

Development of a successful controller requires a sound understanding of the system to be controlled. To this end, the nonlinear model of Eq. (2.90) and its linearized perturbed form (Eq. (2.97)) will be analyzed from the standpoint of control system design.

Approximations Inherent in the Nonlinear Model

As discussed in the preceding chapters, numerous approximations have been made throughout the derivation of Eq. (2.90). Use of the Euler-Bernoulli PDE to model the vibration of the flexible arm restricts the magnitude of the deflection and neglects the lumped masses of the aluminum bridges and the diode mounted at the tip. Rotary inertia and shear deformation are ignored. The assumed modes method truncates the number of modes and discretizes the continuous model yielded by the Euler-Bernoulli PDE. Structural and Coulomb damping are modeled by viscous damping. Furthermore, although the hub position controller is good, it is certainly not ideal.

The accuracy of the nonlinear model is therefore not perfect and is a function of the accuracy of the preceding approximations.

Linear Versus Nonlinear Control

The concept of control design based on the nonlinear model is, initially, an attractive one. Working directly with the nonlinear model, after all, eliminates the task of linearization. Furthermore, a controller based on a locally linearized model will not perform as intended unless the range of operation is restricted to a region close to the system's operating

point. Nonlinear systems, though, are usually difficult to treat mathematically. A large number of techniques exist for the design and analysis of linear systems. For these reasons, the controllers designed in this chapter use the linearized model of the flexible manipulator.

Local Versus Global Linearization

As previously explained, the linearization performed is local in nature. Feedback linearization, on the other hand, is a nonlinear control technique that features the use of state space coordinate changes and control dependent coordinate changes to transform the nonlinear system into one that is *globally* linear, that is, it behaves in a linear fashion over its entire range of operation. Powerful linear control design techniques can then be applied.

Typically, the input signal is generated by feeding back all of the system's states. Consider the nonlinear plant with single input u and state vector z described by $\dot{z} = f(z,u)$. Input-state linearization is demonstrated in Figure 3.1 where $\dot{z} = f(z,u)$ is transformed into the equivalent linear time invariant form $\dot{x} = \boldsymbol{A}x + \boldsymbol{b}v$ by using the state transformation $x=w(z)$ and the input transformation $u=g(z,v)$. The inner loop achieves the linear relationship between the new input v and the transformed state vector x, while the outer loop implements a linear pole placement control using gain vector $\boldsymbol{k}$.

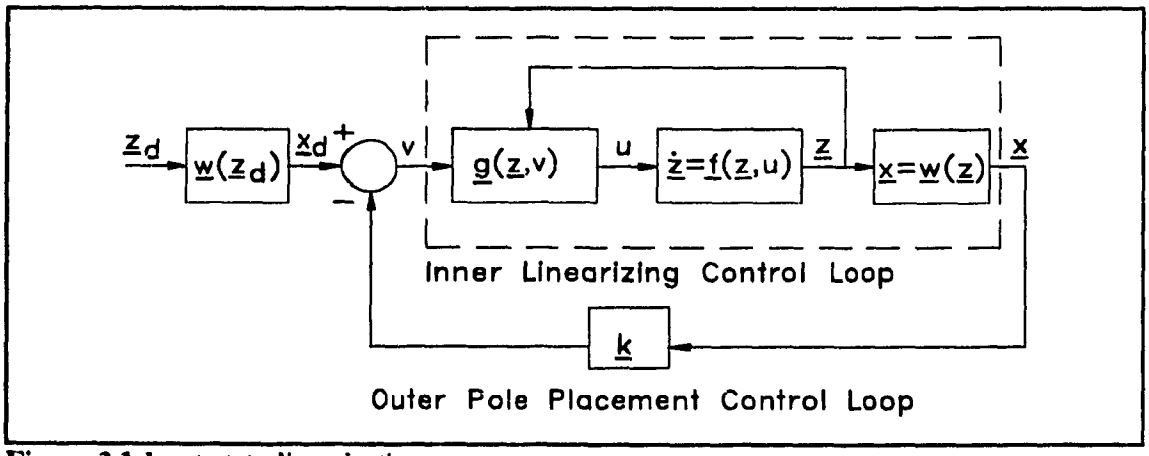

Figure 3.1 Input-state linearization.

Consider the scalar output y defined for the previous nonlinear system by the

expression $y = s(z)$. If it is desired to track a desired output trajectory y_d and if this trajectory can be defined in terms of a corresponding state vector trajectory z_d, then input-state linearization accompanied by linear pole placement as shown in Figure 3.1 will be successful. If it is not possible to generate the vector z_d, a direct, linear relationship must be found between a new input v and output y (or a higher order derivative of y). This method is termed *input-output* linearization. The output y is then furnished directly by the linearization process, and is available for use by an appropriate linear tracking controller as shown in Figure 3.2.

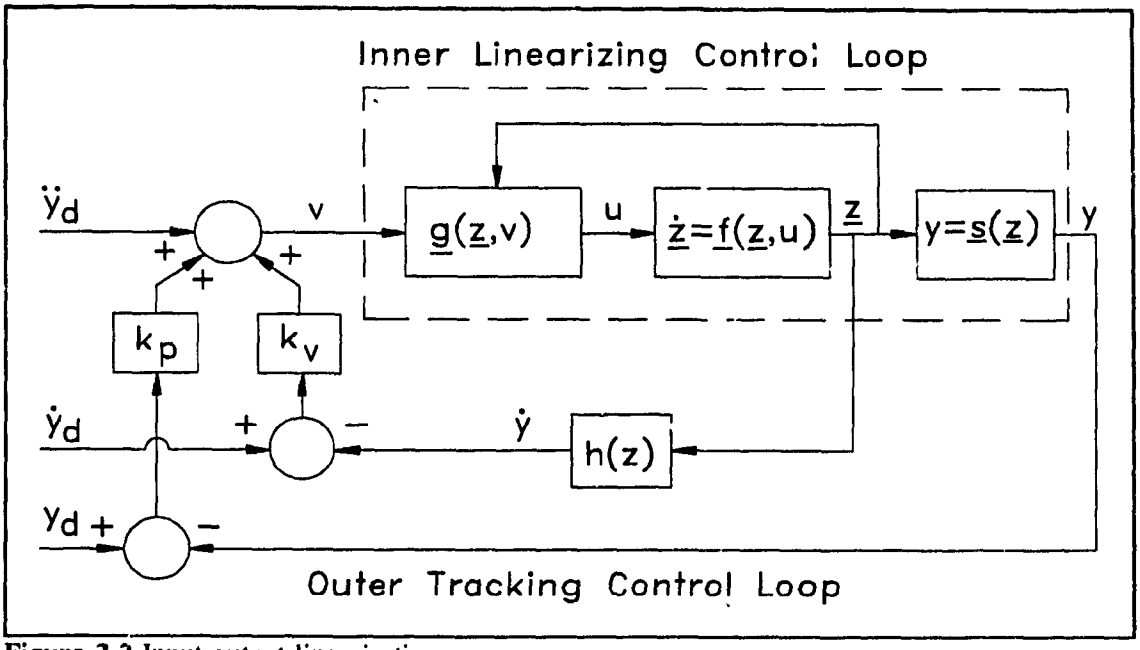

Figure 3.2 Input-output linearization.

Input-output linearization typically requires repeated differentiation of y to yield an equation that includes u, a higher order derivative of y and terms involving the system's states (some of which are nonlinear). The nonlinear terms can be cancelled by choosing u to be an appropriate function of the states and a new input v, that is, $u = g(z,v)$. The input v may then be designed using linear control techniques so that y tracks y_d. The procedure is illustrated in Figure 3.2 for a system requiring differentiation of y twice to yield a direct relationship between $\ddot{y}$ and u. (The system is said to be of relative degree two).

Full state feedback is required to generate the input transformation $u = g(z,v)$ and

to compute $\dot{y}$. A part of the nonlinear system's dynamics may be rendered unobservable during the input-output linearization; these dynamics cannot be discerned from the equation relating v and y. These *internal* dynamics must be stable for the input-output linearization to succeed.

Some insight into the stability of the internal dynamics is acquired by investigating the special case of the internal dynamics when the control input v is such that y is zero (i.e., the *zero* dynamics). Motivation for studying the zero dynamics is due to the fact that although the stability of the internal dynamics may depend upon the control input, the zero dynamics are an intrinsic property of the nonlinear system and are therefore much easier to obtain and evaluate. The limitation of analyzing the zero dynamics is that their stability implies only *local* stability of the internal dynamics. Only local stability can therefore be concluded for closed-loop systems based on input-output linearization, even though the zero dynamics are globally stable. One may then question the significance of input-output linearization when linear control techniques based on linearization and pole placement will also yield a locally stable closed-loop system. The value of input-output linearization is illustrated by the problem of stabilizing a nonlinear system about an unstable or marginally stable equilibrium point. Using a linear control approach, the nonlinear system is linearized about the equilibrium point, and pole placement is used to locally stabilize the system. This method will not succeed if the linearized system contains any uncontrollable modes that are marginally stable. If, on the other hand, the zero dynamics of the nonlinear system are asymptotically stable, pole placement of the external dynamics of the input-output linearized system will achieve local stabilization. A pole placement strategy based on the input-output linearized system will therefore succeed while pole placement based on the linearized approximation that contains uncontrollable but marginally stable modes will fail.

De Luca *et al.* (1988) have demonstrated that the stability of the zero dynamics of a simplified nonlinear model of a single-link flexible arm varies according to the position of the point along the arm defined as the output. The zero dynamics remain stable as the output position is shifted along the arm from the hub towards the tip until

a certain location is reached. As the output position is shifted beyond this critical point, the zero dynamics become unstable. Input-output linearization is therefore not feasible for the flexible manipulator if the output is chosen to be the tip position. Precise tracking control of the tip using this method cannot be achieved. (If the output is redefined to be a location along the arm that results in stable zero dynamics, precise tracking control of this location can be attained. A finite error for the tip position will of course be present.)

A potential difficulty concerning both types of feedback linearization techniques is the requirement for full state measurement. For the flexible manipulator, for example, the states are not all directly measurable. Construction of a state observer will solve this problem at the cost of additional complexity.

Nonminimum Phase Systems

A nonlinear system with unstable zero dynamics may yield a linearized system that is nonminimum phase. Such is the case for Eq. (2.97). Straightforward application of constant output feedback to this system will lead to system instability for a sufficiently large gain. Nebot *et al.* (1988) encountered this difficulty when applying proportional plus derivative control to the flexible manipulator control problem. The closed-loop system became unstable with small increases of the controller gain. To illustrate this behaviour, consider the constant output feedback control system shown in Figure 3.3.

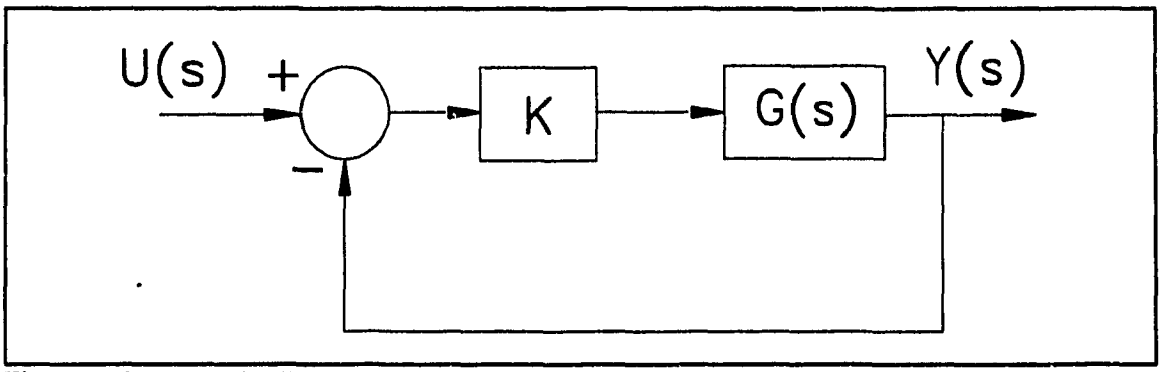

Figure 3.3 Output feedback control system.

Plant $G(s) = N(s)/D(s)$, where

$$N(s) = s^n + a_1 s^{n-1} + \ldots + a_{n-1} s + a_n$$

and

$$D(s) = s^m + b_1 s^{m-1} + \ldots + b_{m-1} s + b_m .$$

$G(s)$ is stable and nonminimum phase, the roots of $D(s)$ are all located in the left-half plane and $N(s)$ has one or more right-half plane roots.The transfer function of the closed-loop system is written

$$\frac{Y(s)}{U(s)} = \frac{G(s)}{1 + KG(s)} = \frac{N(s)}{KN(s) + D(s)} . \tag{3.1}$$

The poles of the closed-loop system are the roots of the denominator of Eq. (3.1). As K becomes very large, this denominator can be approximated by $KN(s)$. Since the roots of $N(s)$ are the zeros of plant $G(s)$ the roots of the closed-loop system gradually approach the zeros of the plant. Since $G(s)$ has right-half plane zeros, some of the closed-loop system poles migrate to the right-half plane causing instability.

3.1.1 Controller Constraints

The preceding discussion has identified certain properties of the nonlinear and linearized models of the flexible manipulator that affect the design of a controller. Specifically, a linearized model will be used to develop a controller because, (a) a wealth of methods exist in the literature that deal with linear systems and, (b) the nonlinear system is difficult to handle mathematically. Moreover, the linearization will be local in nature because global linearization requires the use of state feedback which is hampered by the requirement of access to the system's states. The application of input-output feedback linearization is also impeded by the unstable zero dynamics. The unavailability of the states motivates the use of an output feedback control strategy. The control design will have to deal with the fact that the locally linearized model is nonminimum phase.

3.1.2 Controller Design: Objective and Strategy

Based on the previous constraints, the objective is to design a controller that

(i) tracks a constant or step reference $y_{ref}(t)$ (set-point tracking), and

(ii) ensures that the closed-loop system remains stable in spite of the destabilizing influence of the open-loop right-half plane zeros.

This two-fold objective leads naturally to a two-part controller, in which one part stabilizes the system while the other achieves set-point tracking. Figure 3.4 illustrates the topology of the proposed controller.

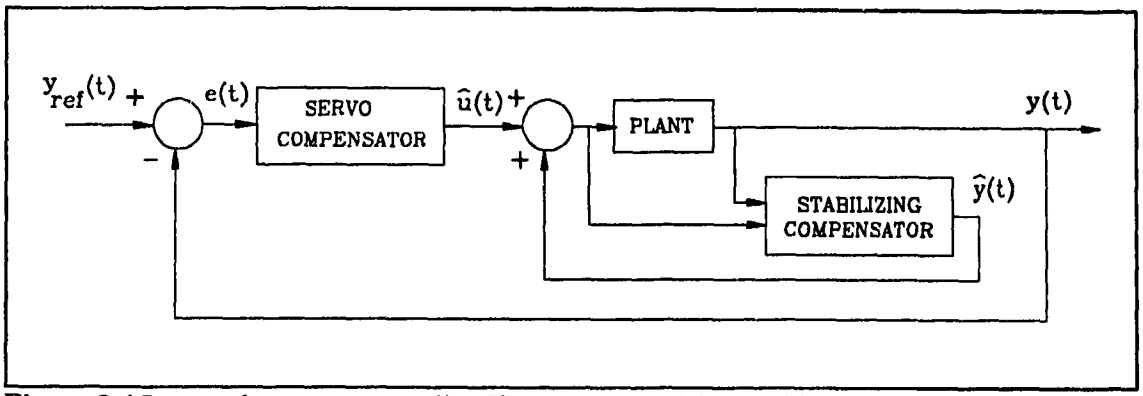

Figure 3.4 Proposed two-part controller. The outer (servo) loop achieves set-point tracking while the inner (stabilization) loop stabilizes the system.

The outer loop controller compares output $y(t)$ with $y_{ref}(t)$. The servo compensator acts upon the resulting error $e(t)$ and produces output $\hat{u}(t)$ which drives $e(t)$ to zero in a prescribed fashion. The inner loop consists of the system defined from input $\hat{u}(t)$ to output $y(t)$ and includes the plant and a stabilization compensator. One way to design the compensator is based on assigning the transmission zeros of the system defined from input $\hat{u}(t)$ to output $\hat{y}(t)$, to desired locations in the complex plane. Although the system under discussion is SISO, the control theory being applied was originally developed for multiple-input and/or multiple-output (multivariable) systems. When the inner loop is closed, (with a specified feedback gain), the inner loop poles approach the assigned transmission zeros. In this manner, by assigning the transmission zeros to appropriate locations in the left-half plane, the pole locations of the inner loop may be placed further within the left-half plane than the poles of the plant. When the outer loop is closed and

the poles of the complete closed-loop system begin to migrate toward the right-half plane zeros of the plant, the added margin of stability generated by the inner loop ensures the stability of the closed-loop system.

3.2 Design of the Inner Stabilization Loop

Two approaches for designing the inner loop using transmission zero assignment are considered. For comparison, a third method using state feedback is also developed.

3.2.1 Transmission Zero Assignment Using Feedthrough Compensation

Consider the inner loop block diagram of Figure 3.5.

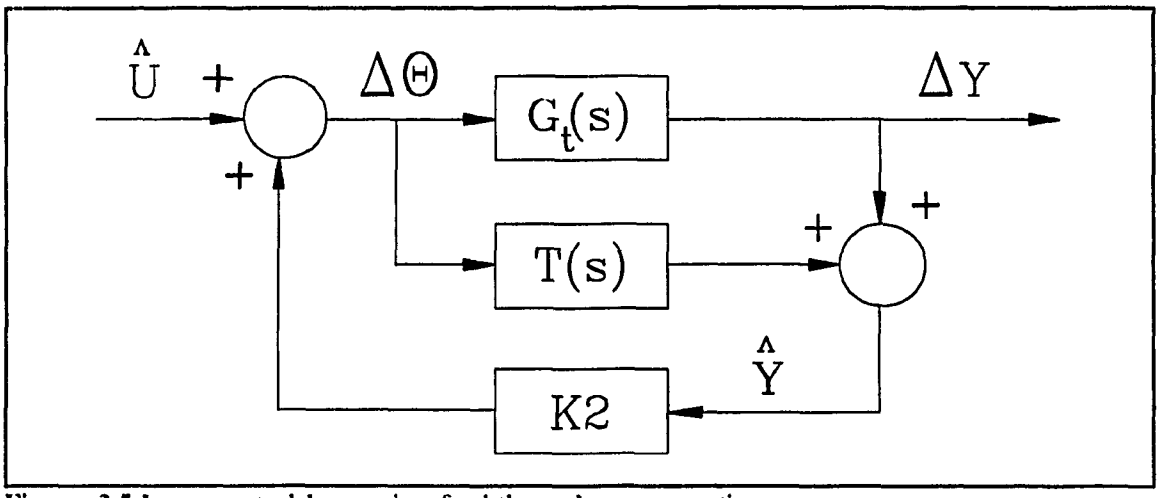

Figure 3.5 Inner control loop using feed-through compensation.

As defined in Eq. (2.98), $G_t(s)$ is the transfer function representation of the linear perturbed state space equation of motion,

$$G_t(s) = \frac{\Delta Y(s)}{\Delta\Theta(s)} = \frac{p(s)}{q(s)} . \qquad (2.98)$$

$T(s)$ is the feed-through compensator and K_2 is a constant gain. Let $T(s) = \frac{p_t(s)}{q_t(s)}$ and define the augmented plant $\hat{G}(s)$ as

$$\hat{G}(s) = G_t(s) + T(s) = \frac{q_t(s)p(s) + p_t(s)q(s)}{q_t(s)q(s)} .$$

Let

$$\begin{aligned} G_o(s) &= \frac{\Delta Y(s)}{\hat{U}(s)} = \frac{G_t(s)}{1 - K_2\hat{G}(s)} \\ &= \frac{q_t(s)p(s)}{q_t(s)q(s) - K_2[q_t(s)p(s) + p_t(s)q(s)]} . \end{aligned} \tag{3.2}$$

The objective is to design $T(s)$ such that some or all of the transmission zeros of $\hat{G}(s)$ are at desired locations in the complex plane (Patel and Misra, 1992). When the inner loop is closed with an appropriate value for gain K_2, the poles of $G_o(s)$ are further within the left-half plane than the poles of $G_t(s)$. Equation (3.2) is simplified by choosing $q_t(s) = q(s)$:

$$G_o(s) = \frac{p(s)}{q(s) - K_2[p(s) + p_t(s)]} . \tag{3.3}$$

Table 3.1 shows the pole-zero locations of plant $G_t(s)$, augmented plant $\hat{G}(s)$ and the inner loop system $G_o(s)$. These values are based on the values of $p(s)$ and $q(s)$ that

Table 3.1 Pole-zero locations.

	ZEROS					POLES			
$G_t(s)$	-1.8 ±77.0i	-1.1 ±47.9i	-20.1	-8.0	14.3 ±4.0i	-2.1 ±102.0i	-0.8 ±52.0i	-1.7 ±18.9i	-0.2 ±3.0i
$\hat{G}(s)$	-8.0 ±102.0i	-8.5 ±52.0i	-8.0 ±19.0i	-11.0 ±3.0i		-2.1 ±102.0i	-0.8 ±52.0i	-1.7 ±18.9i	-0.2 ±3.0i
$G_o(s)$	-1.8 ±77.0i	-1.1 ±47.9i	-20.1	-8.0	14.3 ±4.0i	-7.95 ±102.0i	-8.44 ±52.1i	-7.97 ±19.1i	-10.8 ±3.2i

have been defined in Eq. (2.99) and for $K_2 = -100$. The polynomial $p_t(s)$ is selected so that the roots of $p_t(s) + p(s)$ (the zeros of $\hat{G}(s)$) are as shown in Table 3.1.

$$\begin{aligned} p_t(s) = {} & 7.7150\times10^{-1}s^8 + 6.9762\times10^{1}s^7 + 1.3894\times10^{4}s^6 + 7.7362\times10^{5}s^5 \\ & + 4.7886\times10^{7}s^4 + 1.4632\times10^{9}s^3 + 3.0882\times10^{10}s^2 \\ & + 3.3931\times10^{11}s + 1.4959\times10^{12} \ . \end{aligned} \tag{3.4}$$

The decision to select a particular set of zero locations for $\hat{G}(s)$ is influenced by the pole locations of $G_t(s)$ as follows. The imaginary parts of the zero locations of $\hat{G}(s)$ are set equal to the imaginary parts of the poles of $G_t(s)$, while the magnitudes of the real parts of the zeros of $\hat{G}(s)$ are greater than the magnitudes of the real parts of the poles of $G_t(s)$. This arrangement ensures that the poles of $G_o(s)$ are adequately damped and that the demanded control torque is not excessive. A large shift of the closed-loop poles away from the open-loop locations results in a large amplitude of the control signal that is applied to the plant. This large amplitude may result in actuator saturation and excessive wear of the system components. Note that the poles of $G_o(s)$ are more heavily damped than those of $G_t(s)$. As expected, the zeros of $G_o(s)$ are the same as those of $G_t(s)$.

Internal Stability

It is obvious that the transfer functions in Table 3.1 are stable. In the context of

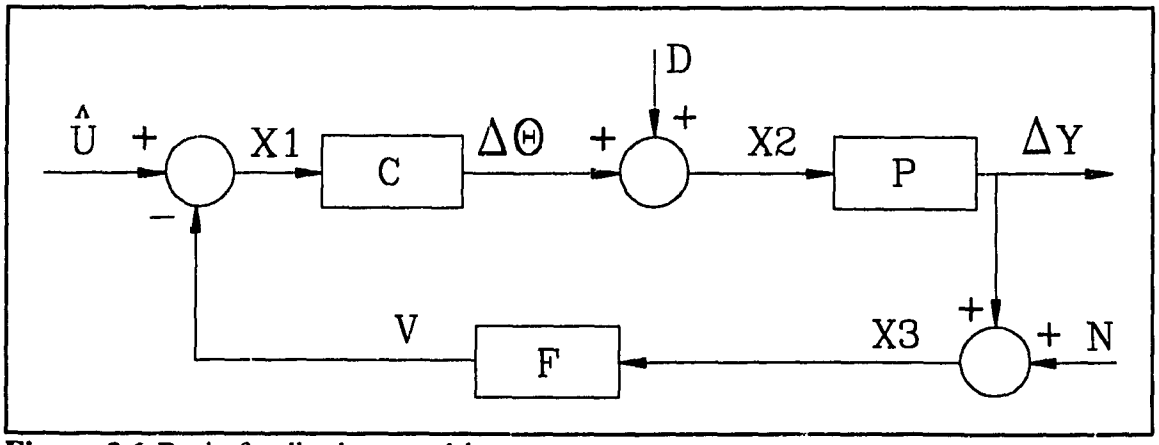

Figure 3.6 Basic feedback control loop.

the basic feedback loop shown in Figure 3.6, however, nine transfer functions exist that relate each of the three inputs (reference $\hat{U}$, disturbance D and sensor noise N) to the internal signals $X1$, $X2$, $X3$, $\Delta\Theta$, ΔY and V. The blocks P, C and F are the transfer functions representing the plant, controller and feedback element, respectively.

It is possible for the transfer function describing the input-output behaviour of the system ($\Delta Y/\hat{U}$) to be stable, and one or more of the eight remaining transfer functions may be unstable (Doyle, Francis and Tannenbaum, 1992). For internal stability, the following two requirements must be satisfied:

1) The transfer function $1+PCF$ has no zeros in **Re** $s\geq 0$. and
2) No pole-zero cancellations occur in **Re** $s\geq 0$ when PCF is formed.

Before applying these requirements, the block diagram of Figure 3.5 (repeated for convenience in Figure 3.7) must be reduced to the form of the basic feedback loop of Figure 3.6. This procedure will allow for the identification of expressions that equate to the transfer functions P, C and F. Figures 3.7 through 3.9 illustrate the reduction process.

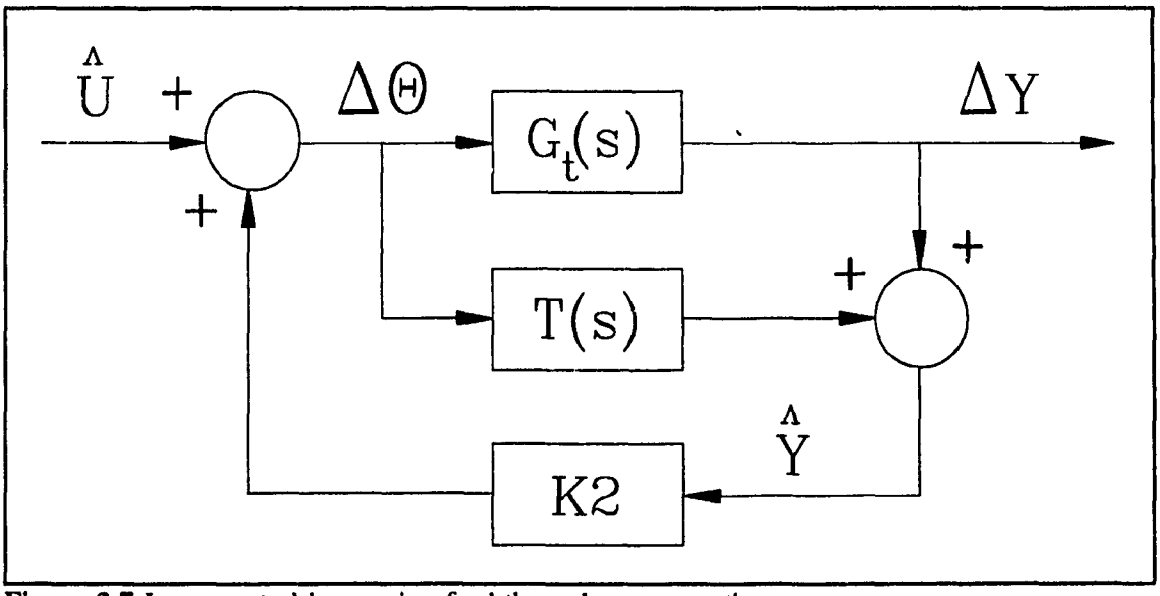

Figure 3.7 Inner control loop using feed-through compensation.

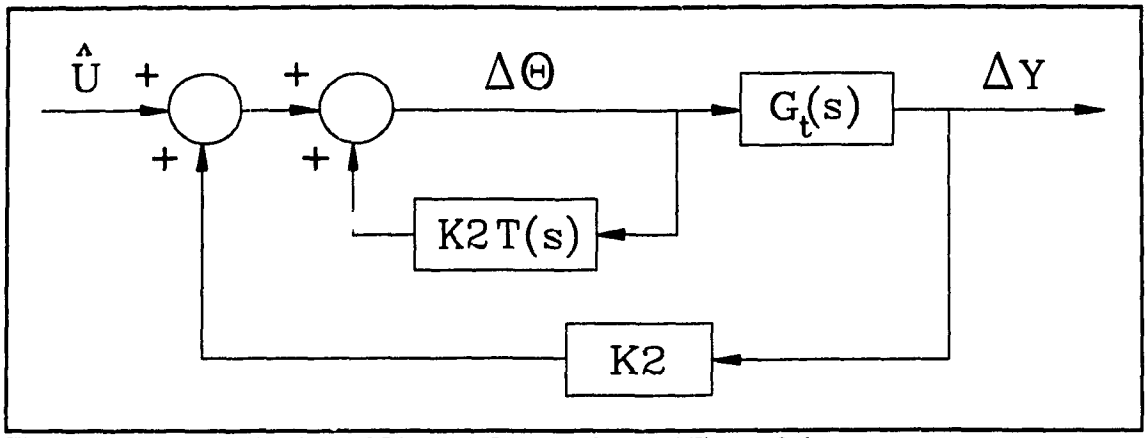

Figure 3.8 Partial reduction of Figure 3.7 to the form of Figure 3.6.

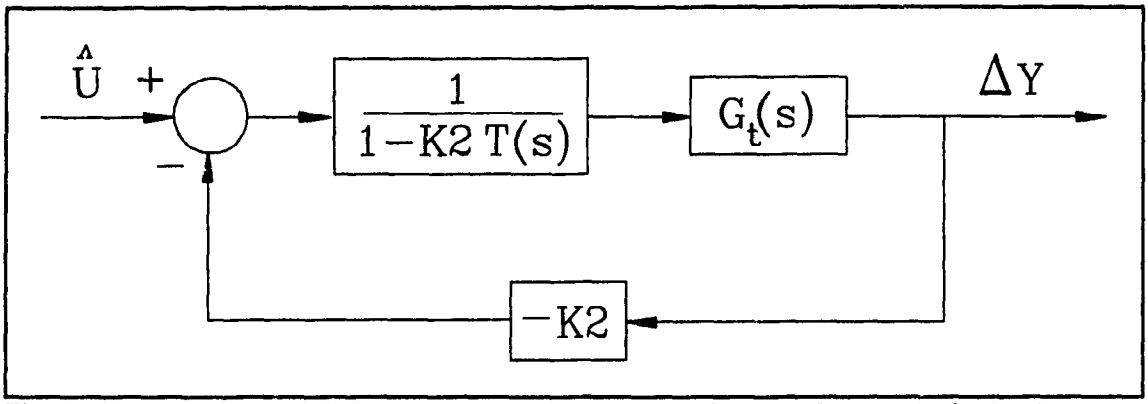

Figure 3.9 Control loop of Figure 3.5 reconfigured in the format of the basic feedback control loop of Figure 3.6.

Inspection of Figure 3.9 yields

$$P = G_t(s) = \frac{p(s)}{q(s)} \qquad C = \frac{1}{1-K_2T(s)} = \frac{q(s)}{q(s)-K_2p_t(s)} \qquad F = -K_2 \ .$$

The product *PCF* can be written as

$$PCF = \frac{p(s)}{q(s)} \times \frac{q(s)}{q(s)-K_2p_t(s)} \times -K_2 \ .$$

Requirement 2 is therefore satisfied.

The transfer function $1+PCF$ can be written as

$$1 + PCF = \frac{q(s) - K_2[p(s) + p_t(s)]}{q(s) - K_2 p_t(s)} \quad .$$

The zeros of $1+PCF$ are the roots of the numerator polynomial. Using the expressions for $p(s)$ and $p_t(s)$ given in Eq's. (2.99) and (3.4) and for $K_2 = -100$, the zeros of $1+PCF$ are

$$[\,-8.0\pm102.0i \quad -8.4\pm52.1i \quad -8.0\pm19.1i \quad -10.8\pm3.2i\,] \quad .$$

Since all zeros of $1+PCF$ are within the left-half plane, the first requirement is also satisfied and the inner control loop is internally stable.

3.2.2 Transmission Zero Assignment Based On Redefining the Output

Consider the linearized model of Eq. (2.97).

$$\begin{pmatrix} \dot{v}_1 \\ \dot{v}_2 \end{pmatrix} = \begin{pmatrix} -M_3^{-1}C_2 & I_N \\ -M_3^{-1}K_1 & 0_N \end{pmatrix} \begin{pmatrix} v_1 \\ v_2 \end{pmatrix} + \begin{pmatrix} M_3^{-1}C_2M_3^{-1}m_2 \\ M_3^{-1}K_1M_3^{-1}m_2 \end{pmatrix} \delta\theta$$

$$\delta y = [\Phi(h) \quad 0_{1xN}] \begin{pmatrix} v_1 \\ v_2 \end{pmatrix} + (h - \Phi(h)M_3^{-1}m_2)\delta\theta \quad . \tag{2.97}$$

Define the system matrix A, the input vector b, the output vector c and the input-output interaction scalar d as:

$$A = \begin{pmatrix} -M_3^{-1}C_2 & I_N \\ -M_3^{-1}K_1 & 0_N \end{pmatrix} \quad b = \begin{pmatrix} M_3^{-1}C_2M_3^{-1}m_2 \\ M_3^{-1}K_1M_3^{-1}m_2 \end{pmatrix} \tag{3.5}$$

$$c = [\Phi(h) \quad 0_{1xN}] \quad d = (h - \Phi(h)M_3^{-1}m_2) \quad .$$

By substituting Eq. (3.5), we can write Eq. (2.97) as

$$\begin{aligned} \dot{v} &= A\,v + b\delta\theta \\ \delta y &= c\,v + d\delta\theta \end{aligned} \tag{3.6}$$

where $v = [v_1^T \; v_2^T]^T$ and $\dot{v} = [\dot{v}_1^T \; \dot{v}_2^T]^T$.

The objective is to design a modified system whose transmission zeros are freely assignable (see Misra, 1992). Figure 3.10 illustrates the procedure. Define *pseudo* output $\hat{y}$ as

$$\hat{y} = \hat{c}v + \hat{d}\delta\theta \; . \tag{3.7}$$

The dynamics of the modified system are written as

$$\dot{v} = A\,v + b\delta\theta \tag{3.8a}$$

$$\hat{y} = \hat{c}v + \hat{d}\delta\theta \; . \tag{3.8b}$$

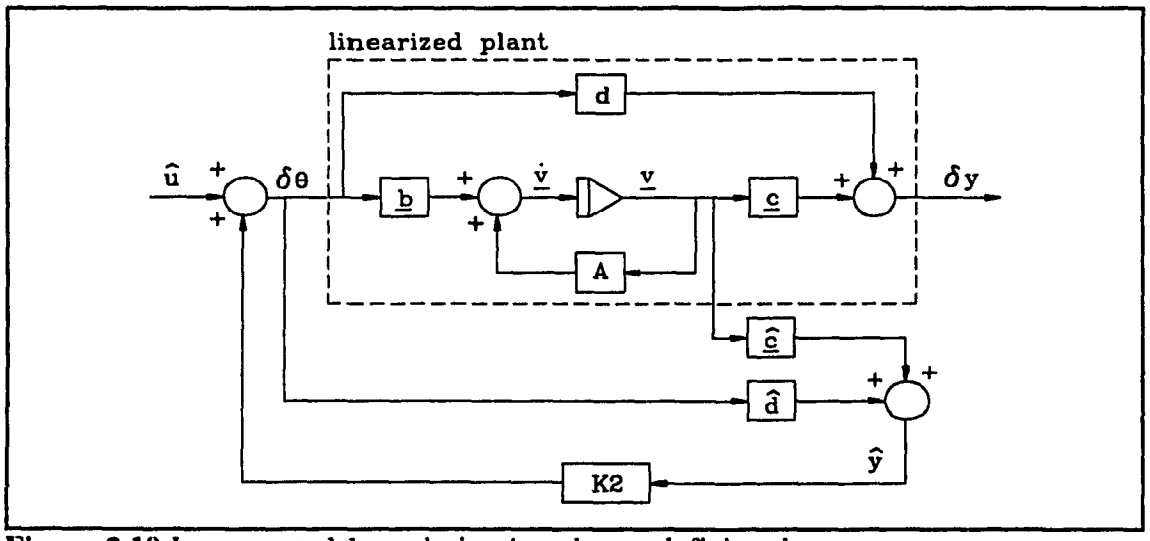

Figure 3.10 Inner control loop design based on redefining the output.

The zero dynamics of the modified system are found by setting $\hat{y} = 0$ in Eq. (3.8b) and solving for $\delta\theta$ in terms of v:

$$\delta\theta = -\hat{d}^{-1}\hat{c}\,v \; . \tag{3.9}$$

Substituting Eq. (3.9) into Eq. (3.8a) yields the zero dynamics of the modified system:

$$\dot{v} = \left[A - b\hat{d}^{-1}\hat{c}\right]v \; . \tag{3.10}$$

The transmission zeros of $(A, b, \hat{c}, \hat{d})$ are the eigenvalues of $\left[A - b\hat{d}^{-1}\hat{c}\right]$ and can be

specified by solving a state-feedback eigenvalue assignment problem to choose appropriate values for $\hat{c}$ for a given value of $\hat{d}$ (see Appendix C). Choose $\hat{d}=1$ for simplicity and let the desired transmission zero locations be as specified for $\hat{G}(s)$ in Table 3.1. The vector $\hat{c}$ is found to be

$$\hat{c} = [20.677 \quad 5.467 \quad -16.099 \quad 0.833 \quad 3.910 \quad 0.082 \quad -0.361 \quad 0.012] \ .$$

Choosing K_2=-100 then yields an inner stabilization loop with the same dynamics as transfer function $G_o(s)$.

This approach requires access to the states of the system to generate $\hat{y}$. Since the states are not available, a practical implementation dictates the use of an observer to obtain an estimate of the states (see Appendix D for details of the observer design). Choosing the eigenvalues of matrix $\boldsymbol{E}$ to be -[15 15.5 16 16.5 17 17.5 18 18.5] ensures that the observer dynamics do not significantly alter the dynamics of the system. Figure 3.11 illustrates the implementation using a full-order observer to generate $\boldsymbol{x}$, an estimate of state vector $\boldsymbol{v}$.

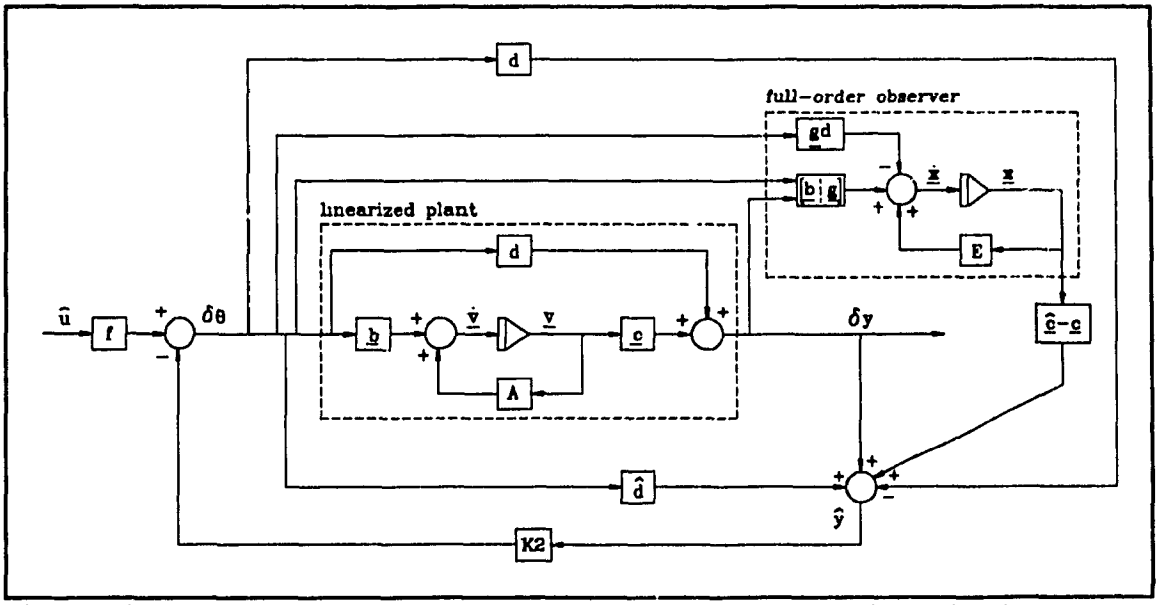

Figure 3.11 Practical implementation of the inner control loop using a full-order observer.

From Figure 3.11, $\hat{y}$ is expressed as

$$\begin{aligned} \hat{y} &= \delta y + \hat{d}\delta\theta + \hat{c}\boldsymbol{x} - \boldsymbol{c}\boldsymbol{x} - d\delta\theta \\ &= \boldsymbol{c}(\boldsymbol{v}-\boldsymbol{x}) + \hat{c}\boldsymbol{x} + \hat{d}\delta\theta \ . \end{aligned} \tag{3.11}$$

In the limit, as $\boldsymbol{x}$ approaches $\boldsymbol{v}$, Eq. (3.11) approaches Eq. (3.7).

3.2.3 Stabilization Via Pole Placement State Feedback

Figure 3.12 illustrates the use of state feedback to place the poles of the system defined by input $\hat{u}(t)$ and output $\delta y(t)$.

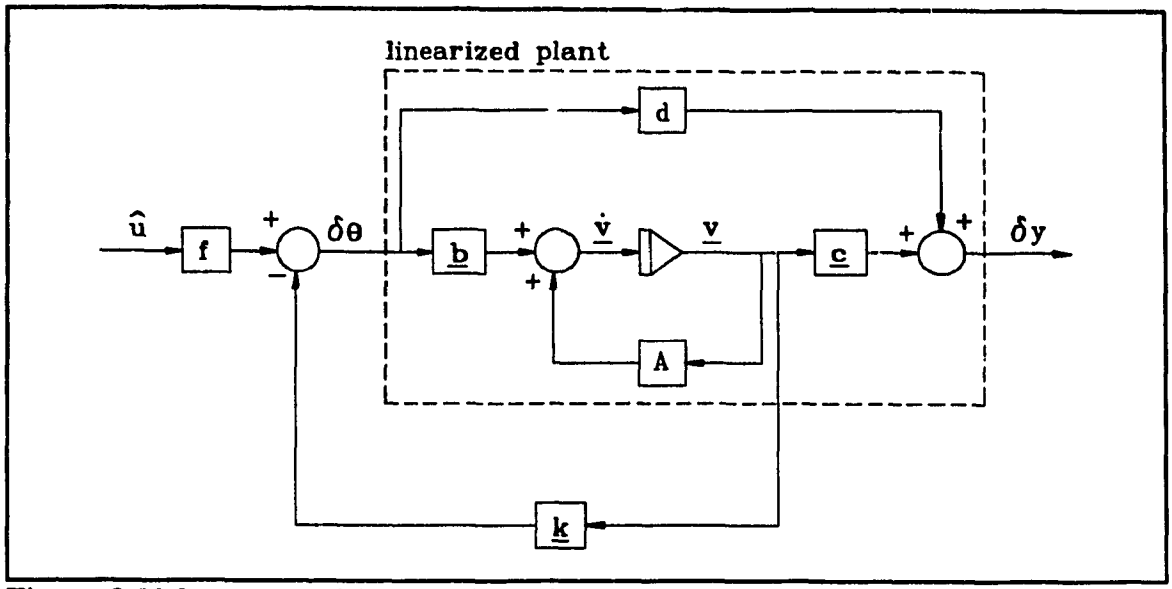

Figure 3.12 Inner control loop design using state feedback pole placement.

The closed-loop system equation is

$$\begin{aligned} \dot{\boldsymbol{v}} &= (\boldsymbol{A} - \boldsymbol{b}\boldsymbol{k})\boldsymbol{v} + \boldsymbol{b}f\hat{u} \\ \delta y &= (\boldsymbol{c} - \boldsymbol{d}\boldsymbol{k})\boldsymbol{v} + df\hat{u} \end{aligned} \tag{3.12}$$

where $\boldsymbol{k}$ is the feedback gain vector that determines the closed-loop pole locations and f is a scalar gain. The transfer function representation of Eq. (3.12) is

$$H(s) = \frac{(\boldsymbol{c} - \boldsymbol{d}\boldsymbol{k})\,\mathrm{Adj}[s\boldsymbol{I}_n - (\boldsymbol{A} - \boldsymbol{b}\boldsymbol{k})]\boldsymbol{b}f + df\Delta(s)}{\Delta(s)} \tag{3.13}$$

where n is the order of the system, and $\Delta(s)$ is the characteristic equation. From Eq. (3.13), it is evident that f determines the gain of the transfer function $H(s)$. The object is to choose $\boldsymbol{k}$ and f so that the gain and poles of $H(s)$ match those of $G_o(s)$. The vector $\boldsymbol{k}$ and the gain f are found to be

$$f = 0.0099$$

$$\boldsymbol{k} = [20.472 \quad 5.413 \quad -15.940 \quad 0.824 \quad 3.871 \quad 0.081 \quad -0.357 \quad 0.012] \; .$$

Figure 3.13 illustrates the practical implementation of the state feedback approach with an observer to obtain an estimate of the states. The observer parameters are identical to those specified in section 3.2.2.

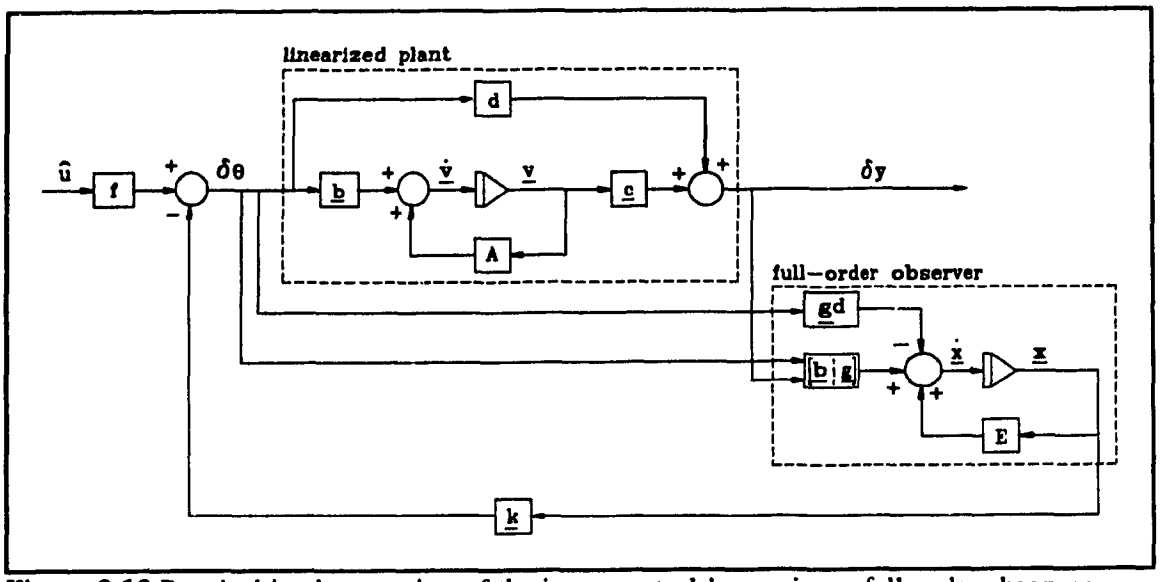

Figure 3.13 Practical implementation of the inner control loop using a full-order observer.

3.3 Design of the Outer Servo Loop

The overall closed-loop system is represented as shown in Figure 3.14, where $S(s)$ is the transfer function of the servo compensator that must be determined. For the operating point $\theta_0 = \dot{\theta}_0 = 0$ and $\boldsymbol{q}_0 = \dot{\boldsymbol{q}}_0 = \ddot{\boldsymbol{q}}_0 = \mathbf{0}$, the inner loop is characterized by the transfer function $G_o(s)$ regardless of which of the three inner loop design methods is used.

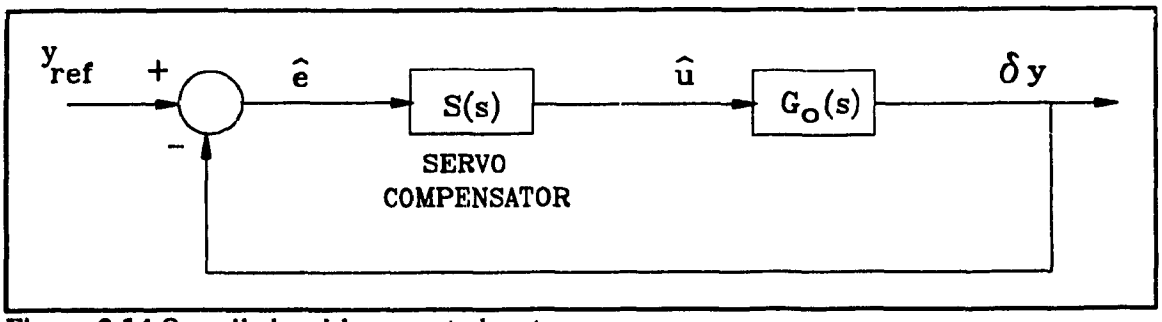

Figure 3.14 Overall closed-loop control system.

To eliminate any confusion caused by the appearance of the perturbed variable $\delta y(t)$ at the output, recall that $\delta y(t)$ can be written as

$$\delta y(t) = h\delta\theta(t) + \Phi(h)\delta q \ . \tag{3.14}$$

As explained in section 2.4.4, there is no restriction on the magnitude of $\delta\theta(t)$. In fact, the linearized perturbed model of Eq. (2.97), (upon which the design of $G_o(s)$ is based), remains valid for any value of $\delta\theta(t)$ that results in acceptably small regions of operation for $\delta\dot{\theta}(t)$ and $\delta\ddot{\theta}(t)$. With no restriction on the magnitude of $\delta\theta(t)$, we are free to let $\delta\theta(t)$ equal the actual hub angle $\theta(t)$. Bearing this in mind, $\delta y(t)$ is a perturbed variable strictly as a result of the influence of $\delta q(t)$: $\delta y(t)$ does include the full rigid-body range of motion $h\theta(t)$. For small deflections, the variable $\delta y(t)$ therefore closely approximates $y(t)$.

Outer Control Loop Design Objectives

The inner control loop has improved the stability of the plant. The purpose of the outer servo loop is to track a constant or step reference $y_{ref}(t)$ with no overshoot.

Asymptotic Tracking

As shown in Figure 3.14, the tracking error $\hat{e}(t)$ is defined as

$$\hat{e}(t) = y_{ref}(t) - \delta y(t) \ .$$

Realistically, perfect tracking, i.e., $\hat{e}(t) = 0 \ \forall \ t \geq 0$, is not in general achievable. A more reasonable specification is *asymptotic* tracking, i.e., $\hat{e}(t) \rightarrow 0$ as $t \rightarrow \infty$. To quantify the problem, define the *steady-state* error as

$$\hat{e}_{ss} = \lim_{t \rightarrow \infty} \hat{e}(t) \ .$$

From Figure 3.14, the Laplace transform of the error is

$$\hat{E}(s) = \frac{Y_{ref}(s)}{1 + L(s)} \tag{3.15}$$

where the loop transfer function $L(s) = S(s)\, G_o(s)$. The transfer functions $S(s)$ and $G_o(s)$ are ratios of coprime polynomials, i.e., polynomials with no common factors, and no pole-zero cancellations occur in **Re** $s \geq 0$ when the product $S(s)\, G_o(s)$ is formed.

The final value theorem yields the following expression for the steady-state error

$$\hat{e}_{ss} = \lim_{t\to\infty} \hat{e}(t) = \lim_{s\to 0} s\hat{E}(s) = \lim_{s\to 0} s\frac{Y_{ref}(s)}{1+L(s)} \tag{3.16}$$

where $s\hat{E}(s)$ must not have any poles in **Re** $s\geq 0$.

To continue the design of the servo compensator $S(s)$, we write $L(s)$ and $Y_{ref}(s)$ as

$$L(s) = \frac{p_L(s)}{q_L(s)} \tag{3.17}$$

and

$$Y_{ref}(s) = \frac{p_{ref}(s)}{q_{ref}(s)} . \tag{3.18}$$

Assume that both $L(s)$ and $Y_{ref}(s)$ are proper. Although $Y_{ref}(s)$ will later be restricted to the Laplace transform of a step function, the current analysis uses the more general form of Eq. (3.18). Substituting Eq.'s (3.17) and (3.18) into Eq. (3.16) yields

$$\hat{e}_{ss} = \lim_{s\to 0} \frac{s\,p_{ref}(s)}{q_{ref}(s)} \times \frac{q_L(s)}{p_L(s)+q_L(s)} . \tag{3.19}$$

Eq. (3.19) must be interpreted in light of the restriction that $s\hat{E}(s)$ must not have any poles in **Re** $s\geq 0$. The poles of $s\hat{E}(s)$ are the roots of the denominator of Eq. (3.19), that is, the roots of $q_{ref}(s)[p_L(s)+q_L(s)]$. The polynomial $p_L(s)+q_L(s)$, however, is the denominator of the error transfer function $\frac{1}{1+L(s)}$. By definition, the error dynamics must be stable, so all the roots of $p_L(s)+q_L(s)$ must therefore be in the left-half plane. The remaining factor in the denominator is $q_{ref}(s)$ which has roots on the imaginary axis for many reference signals of interest. If, however $q_L(s)$ also contains these same roots, these roots cancel and $s\hat{E}(s)$ has no poles in **Re** $s\geq 0$. Furthermore, the numerator of $s\hat{E}(s)$ then contains the factor s and in the limit, when $s\to 0$, $s\hat{E}(s)\to 0$. In other words, $q_L(s)$ must contain those roots of $q_{ref}(s)$ in **Re** $s\geq 0$ to ensure that $\hat{e}_{ss}=0$.

The preceding results are now applied to design $S(s)$. For a reference step input

of amplitude Y_{ref}, $Y_{ref}(s)$ is written as

$$Y_{ref}(s) = \frac{Y_{ref}}{s} . \tag{3.20}$$

Let $G_o(s)$ be as specified in Eq. (3.3):

$$G_o(s) = \frac{p(s)}{q(s) - K_2[p(s) + p_t(s)]} . \tag{3.3}$$

We proceed by letting the denominator of Eq. (3.3) equal $q_o(s)$. Equation (3.3) is then rewritten as

$$G_o(s) = \frac{p(s)}{q_o(s)} . \tag{3.21}$$

Write $S(s)$ as the ratio of polynomials

$$S(s) = \frac{p_s(s)}{q_s(s)} . \tag{3.22}$$

Substitute equations (3.20), (3.21) and (3.22) into Eq. (3.19):

$$\hat{e}_{ss} = \lim_{s \to 0} \frac{s\, Y_{ref}}{s} \times \frac{q_s(s)\, q_o(s)}{p_s(s)\, p(s) + q_s(s)\, q_o(s)} . \tag{3.23}$$

As shown in Table 3.1, the eight roots of polynomial $q_o(s)$ occur as complex conjugate pairs in **Re** $s<0$. From the preceding discussion, $q_s(s)$ should therefore be specified so as to cancel the pole at the origin in Eq. (3.23). Initially, this appears unnecessary since this pole is already cancelled by the factor s that occurs in the numerator. If both $p_s(s)$ and $q_s(s)$ are properly chosen, then, Eq. (3.23) has no poles in **Re** $s \geq 0$. However, due to the fact that $L(s)$ (and therefore $\frac{1}{1+L(s)}$, the second term of Eq. (3.23)) is proper, $\hat{e}_{ss}$ is infinite or, at best, finite, but definitely not zero. To ensure that $\hat{e}_{ss}=0$, $q_s(s)$ must cancel the pole at the origin. The simplest polynomial that achieves this cancellation is $q_s(s)=s$. With $q_s(s)$ known, $p_s(s)$ remains to be specified to complete the

design of $S(s)$. To accomplish asymptotic tracking, $p_s(s)$ must be chosen to ensure that the roots of $p_s(s)p(s)+q_s(s)q_o(s)$ are within the left-half plane. However, the selection of $p_s(s)$ also influences the transient response of $\hat{e}(t)$, a topic that will be addressed in the following section.

Transient Response

Servo compensator $S(s)$ has been designed so that the steady state error is zero for a reference step input, that is, $\delta y(t)$ tracks $y_{ref}(t)$ with no error as $t \to \infty$. Constraints must also be placed on the transient response to ensure that both the amplitude and the time duration of the transient response are kept within tolerable limits. The transient behaviour of $\delta y(t)$ can be assessed by analyzing the poles and zeros of the closed-loop transfer function $\frac{\Delta Y(s)}{Y_{ref}(s)}$. From Figure 3.14, the expression for $\frac{\Delta Y(s)}{Y_{ref}(s)}$ is written as

$$\frac{\Delta Y(s)}{Y_{ref}(s)} = \hat{E}(s)\, S(s)\, G_o(s) \ . \tag{3.24}$$

Substituting Eq's. (3.15), (3.21) and (3.22) into Eq. (3.24) and choosing $q_s(s)=s$ yields

$$\Delta Y(s) = \frac{Y_{ref}(s)\, s q_o(s)}{p_s(s)p(s)+s q_o(s)} \times \frac{p_s(s)}{s} \times \frac{p(s)}{q_o(s)} = \frac{Y_{ref}(s)\, p_s(s)p(s)}{p_s(s)p(s)+s q_o(s)} \ . \tag{3.25}$$

The closed-loop transfer function is

$$\frac{\Delta Y(s)}{Y_{ref}(s)} = \frac{p_s(s)p(s)}{p_s(s)p(s)+s q_o(s)} \ . \tag{3.26}$$

By choosing the simplest possible form for $p_s(s)$, that of a constant, (say K_1), Eq. (3.26) becomes

$$\frac{\Delta Y(s)}{Y_{ref}(s)} = \frac{K_1 p(s)}{K_1 p(s)+s q_o(s)} = \frac{n_1 s^8+n_2 s^7+\ldots+n_8 s+n_9}{d_1 s^9+d_2 s^8+\ldots d_9 s+d_{10}} \ . \tag{3.27}$$

As shown in Figure 3.15, plotting the root-locus for the system of Eq. (3.27)

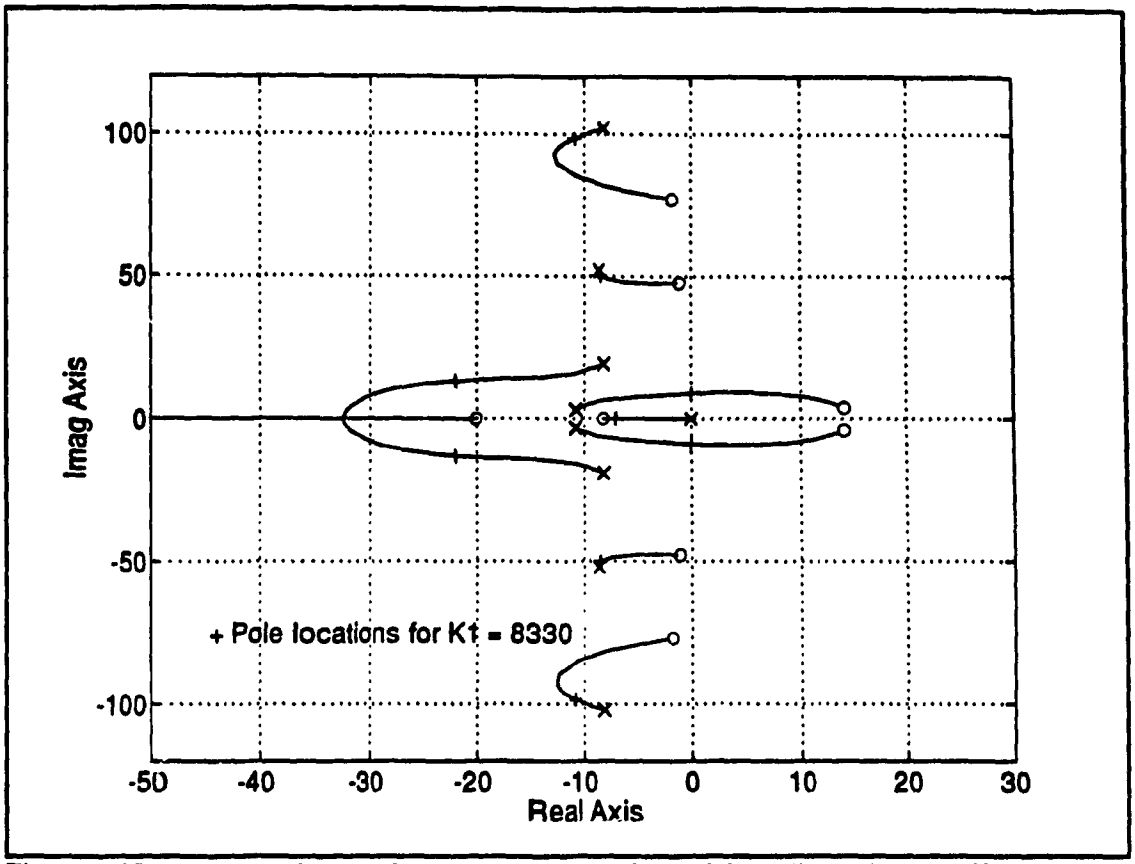

Figure 3.15 Root-locus for the closed-loop system of Eq. (3.27), illustrating the effect of K_f on the pole locations.

shows the effect of gain K_f on the pole locations. As K_f is increased from 0, the closed-loop poles move from the open-loop pole locations toward the open-loop zero locations (the open-loop transfer function is $\frac{1}{s} \times G_o(s)$). This pole-shifting behaviour has been described in Section 3.1. For $0 \leq K_1 < 8330$, the closed-loop poles are in **Re** $s \leq 0$. For $K_1 \geq 8330$, however, the complex conjugate pair of poles corresponding to the first elastic mode crosses the imaginary axis into the right-half plane, resulting in an unstable system.

Pole Placement Design

Poles that are situated well within the left-half plane produce transient responses that decay relatively quickly. Poles that are located close to the imaginary axis in the left-half plane (dominant poles), however, yield transient responses that decay relatively slowly. The design process can be simplified by choosing K_1 so as to limit the number of dominant poles and to place these poles in locations to achieve a desired transient response.

Choosing K_1 = 1850 results in the closed-loop pole-zero locations plotted in Figure 3.16 and shown in Table 3.2. The dominant pole is located at s=-1.62 s^{-1} and the transient response is essentially that of a first order system with a time constant equal to $\frac{1}{1.62}$ s.

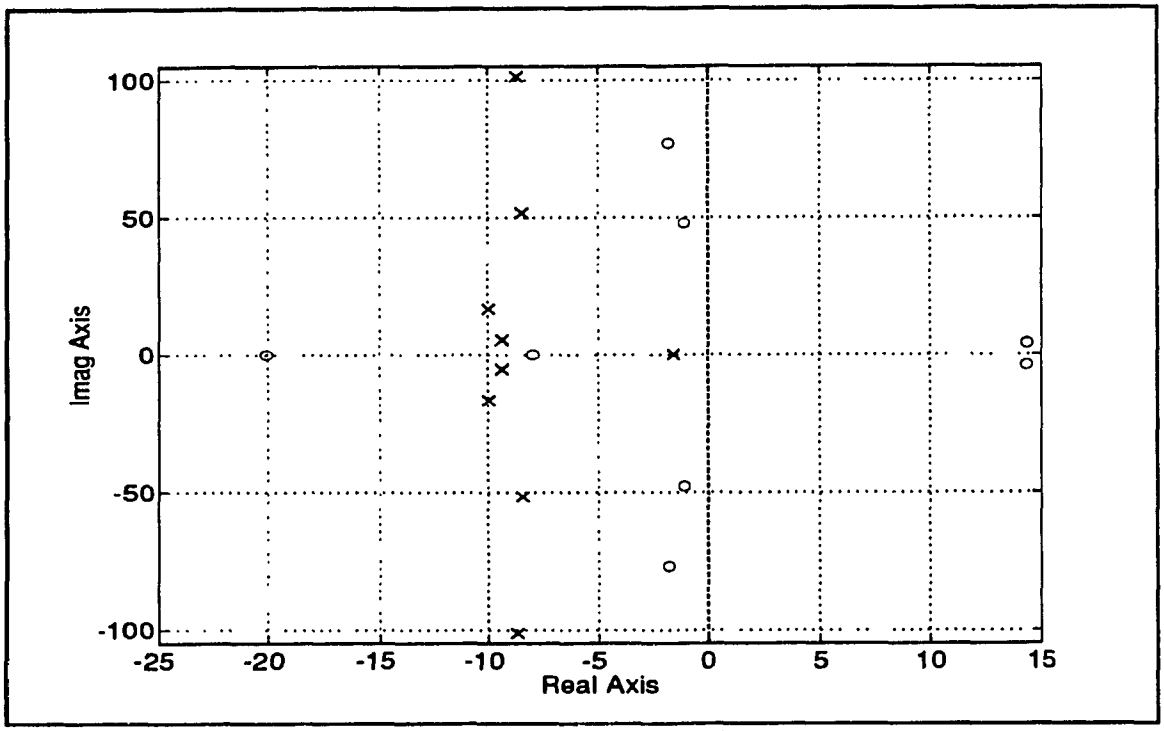

Figure 3.16 Pole-zero map of closed-loop system for K_1=1850.

Table 3.2 Closed-loop pole-zero locations for K_1=1850.

ZEROS					POLES				
-1.8 ±77.0i	-1.1 ±47.9i	-20.1	-8.0	14.3 ±4.0i	-8.71 ±101.3i	-8.47 ±51.7i	-9.96 ±16.6i	-9.35 ±5.4i	-1.62

The closed-loop numerator and denominator polynomials are shown in Eq's. (3.28) and (3.29), respectively.

$$\begin{aligned} K_1 p(s) = {} & 4.229\times10^{2}s^{8}+2.291\times10^{3}s^{7}+3.298\times10^{6}s^{6}+6.904\times10^{6}s^{5} \\ & +4.288\times10^{9}s^{4}-1.463\times10^{9}s^{3}-2.284\times10^{12}s^{2} \\ & +9.539\times10^{12}s+2.031\times10^{14} \end{aligned} \tag{3.28}$$

$$\begin{aligned} K_1 p(s)+sq_o(s) = {} & 1.010\times10^{2}s^{9}+7.532\times10^{3}s^{8}+1.584\times10^{6}s^{7}+8.111\times10^{7}s^{6}+5.060\times10^{9}s^{5} \\ & +1.506\times10^{11}s^{4}+2.974\times10^{12}s^{3}+3.217\times10^{13}s^{2} \\ & +1.702\times10^{14}s+2.031\times10^{14}\ . \end{aligned} \tag{3.29}$$

Effect of Zeros on the Closed-Loop System

Equation (3.27) can be expanded as

$$\frac{\Delta Y(s)}{Y_{ref}(s)} = \frac{n_9}{d_1 s^9+d_2 s^8+\ldots+d_{10}}+\frac{n_8 s}{d_1 s^9+d_2 s^8+\ldots+d_{10}}+ \frac{n_7 s^2}{d_1 s^9+d_2 s^8+\ldots+d_{10}}+\ldots+\frac{n_1 s^8}{d_1 s^9+d_2 s^8+\ldots+d_{10}}\ . \tag{3.30}$$

For a given input $y_{ref}(t)$, let the response of the output that corresponds to the first term on the right-hand side of Eq. (3.30) equal $\delta y_1(t)$. The output $\delta y(t)$ can be written as

$$\delta y(t) = \delta y_1(t)+\frac{n_8}{n_9}\times\frac{d\delta y_1(t)}{dt}+\frac{n_7}{n_9}\times\frac{d^2\delta y_1(t)}{dt^2}+\ldots+\frac{n_1}{n_9}\times\frac{d^8\delta y_1(t)}{dt^8}\ . \tag{3.31}$$

Although the pole at s=-1.62 s^{-1} is dominant for the system of Eq. (3.30), the remaining poles influence the transient response to some extent, particularly for short time durations after discontinuities in $y_{ref}(t)$. For a transfer function containing a pair of complex conjugate poles situated at $s = -\alpha\pm jw$, for example, oscillations in the transient response occur with a frequency w and decay at a rate proportional to $e^{-\alpha t}$. As shown in Eq. (3.31), $\delta y(t)$ equals the sum of $\delta y_1(t)$ and its higher derivatives, weighted by the coefficients $\frac{n_i}{n_9}$, $i=1,2,\ldots,8$. Since $\delta y_1(t)$ contains rapidly decaying oscillations, its

higher-order derivatives are characterized by extreme fluctuations. Although the amplitudes of these fluctuations are reduced by the small magnitude of the coefficients, (n_9 is at least an order of magnitude larger than the remaining polynomial coefficients of Eq. (3.28)), $\delta y(t)$ will still exhibit some high frequency vibrations in response to abrupt transitions of $y_{ref}(t)$.

Once the rapidly decaying oscillations of $\delta y_f(t)$ have died out and its variation becomes more gradual, the lower-order derivative terms, (whose coefficients are of larger magnitude than the higher-order terms), play a predominant role in influencing $\delta y(t)$. Specifically, the derivative terms with positive coefficients act to decrease the rise time of $\delta y(t)$, while the derivative terms with negative coefficients (a result of the right-half plane zeros) serve to increase the rise time of δy(t). For the system of Eq.'s (3.27) and (3.28) the magnitudes of negative coefficients $\frac{n_6}{n_9}$ and $\frac{n_7}{n_9}$ are smaller than the magnitude of positive coefficient $\frac{n_8}{n_9}$. It is therefore theorized that, once the high frequency vibrations have decayed, the net effect of the zeros is to decrease the rise time of $\delta y(t)$.

Chapter 4

Simulations

4.1 Introduction

This chapter presents three sets of closed-loop simulations, each set corresponding to one of the three inner stabilization loop configurations described in the previous chapter. The outer servo loop parameters are identical for each case. Any differences in the results are therefore caused by different characteristics of the inner loop configurations.

Chapter 5 displays experimental results for the closed-loop system that incorporates an inner loop designed using feedthrough compensation. Consequently, the simulations corresponding to this particular inner loop compensator are more extensive than for the two remaining types.

All simulations are conducted using **SIMULINK**.

4.2 Closed-Loop System With An Inner Loop Design Based On Feedthrough Compensation

The control system has been designed based on the linear plant model with ideal hub position control of Eq. (2.97). To assess the inevitable degradation in performance when the control system is applied to the nonlinear model with PD hub position control, three different series of simulations are performed. Each series incorporates a different plant model. The models used are:

(i) the linear plant model with ideal hub position control of Eq. (2.97),

(ii) the nonlinear plant model with ideal hub position control of Eq. (2.92), and

(iii) the nonlinear plant model of Eq. (2.89) together with the PD hub position controller.

Varying the plant model highlights those plant characteristics primarily responsible for performance degradation.

$y_{ref}(t) = 0.1\ m$

Figures 4.1 through 4.6 show the responses to a reference step input $y_{ref}(t) = 0.1$ m.

The net tip position for the linear plant model of Eq. (2.97) appears in Figure 4.1a. Its value is initially negative, then positive as it attempts to follow the step input. This behaviour is a result of the excessive phase delay characteristic of nonminimum-phase systems. Since the phase delay becomes larger with increasing frequency, the transient portion of the plot, (which contains the highest frequency components), experiences the maximum effect of the delay.

As discussed in Section 3.3, the time constant corresponding to the dominant pole is $\frac{1}{1.62}$ s. When Figure 4.1a is compared with the 0.1 m step response of a first order system with the same time constant, the first order system's reponse is faster. This observation appears to contradict the prediction of Section 3.3 that the effect of the zeros on the closed-loop system is to *decrease* the rise time. This discrepancy is due to the negative-going excursion shown in Figure 4.1a that effectively delays the response by 0.205 s. If the plot of Figure 4.1a is shifted to the left by this amount of time and subsequently compared with the first order system's reponse, the predicted decreased rise time is observed.

The main feature that differentiates Figure 4.1b from Figure 4.1a is a damped 3 rad/s oscillation. To investigate the probable cause of this oscillation, refer to the hub velocity of Figure 4.4b and the tip deflection of Figure 4.5b. The hub velocity $\dot{\theta}(t)$ ranges from 2.16 rad/s to -0.18 rad/s during the first 0.26 s of the simulation. The tip deflection, and therefore the vector $\boldsymbol{q}(t)$, also reach their maximum magnitudes during this same time interval. Since both $\dot{\theta}(t)$ and $\boldsymbol{q}(t)$ are relatively large, the effect of the nonlinear centrifugal force vector $-\dot{\theta}^2 \boldsymbol{K}_2 \boldsymbol{q}$ is no longer negligible. The design of the controller,

however, is based on the linearized plant model for which $\dot{\theta}_0(t)=0$. As explained in Section 2.4.5, as $\dot{\theta}_0(t)$ varies, the term $-\dot{\theta}_0^2(t)\boldsymbol{K}_2$ exerts a time-varying influence upon the eigenvalues of the flexible dynamics. These eigenvalues become less damped as the magnitude of $\dot{\theta}_0(t)$ increases.

In a similar fashion, the flexible dynamics of the nonlinear plant become less damped as $\dot{\theta}(t)$ increases. As shown in Figure 4.5b, the tip deflection, (which is a function of the flexible dynamics), is the source of the oscillation. Specifically, the lowest flexible mode is the cause since its natural frequency of 3 rad/s equals that of the oscillation. Presumably, the relatively large magnitudes of $\dot{\theta}(t)$ caused by the step change in $y_{ref}(t)$ cause a reduction in the damping of the flexible dynamics, especially for the lowest flexible mode. The controller has not been designed for the reduced damping: this incompatibility manifests itself as an oscillation of the tip deflection that also appears in the net tip position. Another way of considering this situation is as a closed-loop system whose linear plant model contains damping coefficients that vary with time. The controller, however, has been designed for the linear plant model that is time invariant. From the controller's standpoint, the damping coefficient variation causes a disturbance effect upon the tip deflection.

Note that the controller does not respond quickly to eliminate these oscillations in the output and that they therefore decay relatively slowly. This can be corrected by designing the servo compensator to suppress disturbances from the tip deflection to the output, in addition to achieving its principal objective of tracking a step reference $y_{ref}(t)$ with no overshoot.

Figure 4.1c shows the effects of the PD hub position controller on the net tip position. The same decaying 3 rad/s oscillation observed in Figure 4.1b is also present, although its amplitude is slightly larger. At approximately 7 s into the simulation, the amplitude increases. These amplitude differences are due to hub position tracking errors. Figure 4.3c shows the commanded and actual hub positions for the time interval from 0

to 1 s. In spite of the relatively high gains of the PD controller, the large amount of Coulomb friction introduces a steady state hub tracking error. PID control would suppress this steady state error at the cost of slowing the response. The hub error most likely results in an increased disturbance effect upon the tip deflection, and consequently, upon the net tip position.

This hub tracking error persists until approximately 7 s at which time the integral action of the outer control loop causes the hub to move. This motion causes the amplitude of the tip deflection oscillation, which up to this point has been decaying, to suddenly increase. Essentially, the imperfect hub tracking due to Coulomb friction results in limit cycling of the hub, tip deflection and net tip position.

Figure 4.6 displays the control torques for the three plant models. All three plots exhibit discontinuities at the beginning of the simulation due to the step reference input.

The steady state torque value for the linear plant model of Figure 4.6a is zero. This is to be expected since the nonlinear Coulomb friction has been approximated by the linearized perturbed term $\frac{k\,c_{coul}}{2}\delta\dot{\theta}$.

In Figure 4.6b, once the transients have decayed, the torque value for the nonlinear plant model remains constant at a value slightly greater than 4.75 Nm. This allows the hub position to just overcome the effects of Coulomb friction and gradually approach its steady state value at a rate governed by the single dominant closed-loop pole. The abrupt transitions between +4.75 Nm and -4.75 Nm that begin to occur at approximately 8.5 s into the simulation are caused by simulation errors rather than by the actual dynamics of the system. The numerical integration proceeds at small but finite time steps and essentially approximates the continuous time system by a discrete time system. This discrete time approximation results in small discontinuities for the calculated hub position values. Since the hub velocity is generated by numerically differentiating the hub position, a certain amount of "noise" is caused by the discontinuities. When the mean value of the hub velocity is close to zero, which occurs toward the end of the simulation when the hub position nears its steady state value, the hub velocity noise dominates. Since the control torque is computed using Eq. (2.89a), small variations in the sign of the velocity result

in large swings of the control torque due to the term $c_{coul}\text{sign}(\dot{\theta})$. (Since the plant input is hub position and not torque, these torque variations do not influence the dynamics of the simulation.)

From 0 to 7 s, the plot of Figure 4.6c is similar to that of Figure 4.6b. The hub position error, which has been relatively constant at 1.7×10^{-3} radians from 2 to 7 s, has resulted in a mean net tip position error of 2 mm for this same time interval. At 7 s, the integral action of the servo compensator has increased the commanded hub position to a value that, in turn, causes the PD hub controller to increase the control torque. The torque increase results in overshoots of both the hub position and the net tip position, and has a disturbance effect upon the tip deflection. This disturbance effect is the cause of the increased amplitude of the 3 rad/s oscillation of the net tip position in Figure 4.1c. The servo compensator then responds to the overshoot of the net tip position by decreasing the commanded hub position which, in turn, causes a decrease in the control torque. The net result is a limit cycle.

$y_{ref}(t) = 0.2\ m$

Figures 4.7 through 4.12 show the responses to a reference step input $y_{ref}(t) = 0.2\,\text{m}$.

The plots corresponding to the linear plant model and the nonlinear plant model with ideal hub position control are very similar to their counterparts for $y_{ref}(t) = 0.1\,\text{m}$, the major differences being a doubling of magnitudes for all quantitities. (This is to be expected since the reference input has been increased by a factor of 2.) The increased magnitudes of $q(t)$, $\dot{q}(t)$, $\ddot{q}(t)$, and $\dot{\theta}(t)$ compromise the performance of the controller since they involve a greater departure of the plant from the operating point.

Some notable differences occur for the nonlinear plant model that includes PD hub position control. The actual hub position overshoots the commanded position during the first 0.3 s of the simulation, as shown in Figure 4.9c. No such overshooting occurs for the 0.1 m input. The frequency of the hub position limit cycle observed beyond 5 s in

Figure 4.8c is greater than for the limit cycle in Figure 4.2c.

$y_{ref}(t) = 0.3\ m$

Figure 4.13 shows the responses to a reference step input $y_{ref}(t) = 0.3\,\text{m}$ for the nonlinear plant model of Eq. (2.89) with PD hub control. Note the increased amplitude of the 3 rad/s oscillation for the net tip position compared to that for the 0.2 m reference input of Figure 4.7a. This is most likely due to the increased disturbance effects of greater hub tracking overshoot and a larger hub velocity magnitude. The maximum magnitude of the tip deflection approaches 0.2 m, which may conflict with the Euler-Bernoulli requirement for small deflections. (Such a conflict will lead to simulation results that will not agree with the actual test-bed responses).

A further increase in the magnitude of the reference input will result in an even greater increase in the overshoot of the commanded hub position. This overshoot will have a greater disturbance effect upon the tip deflection and further increase the amplitude of the 3 rad/s oscillation observed at the net tip position. As the reference input becomes even larger, the combined effects of decreased damping of the flexible dynamics caused by large values of hub velocity, and increased hub position overshoot and larger deflections will probably lead to instability. (Eventually, the magnitude of the deflection will rise to a level that will be in gross violation of the Euler-Bernoulli constraint and will render the simulation meaningless).

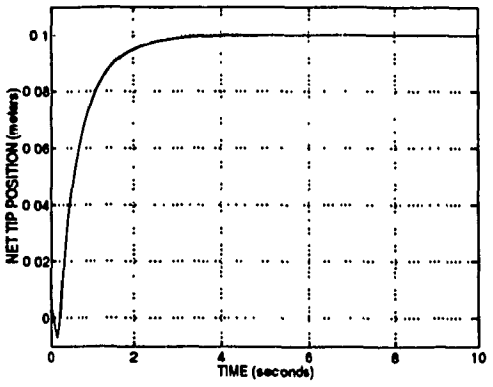

(a)

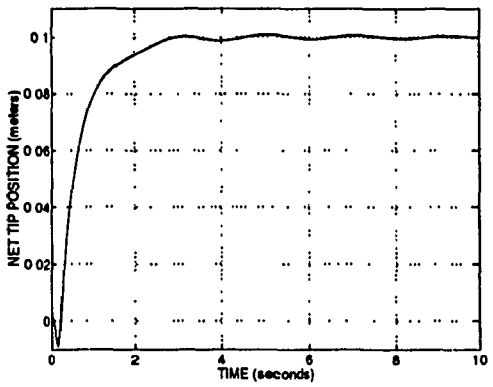

(b)

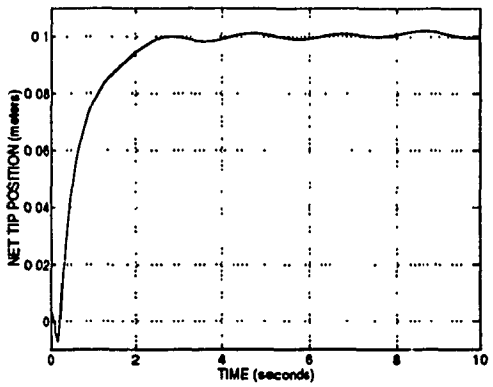

(c)

Figure 4.1 Response of net tip position to 0.1 m step reference. (a) Linear plant, (b) nonlinear plant with ideal hub control, (c) nonlinear plant with PD hub control.

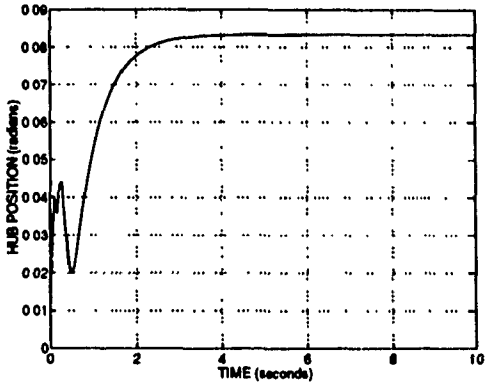

(a)

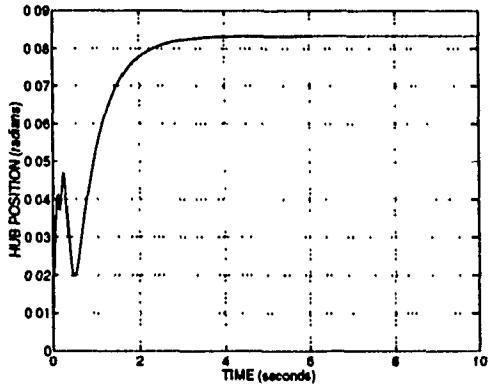

(b)

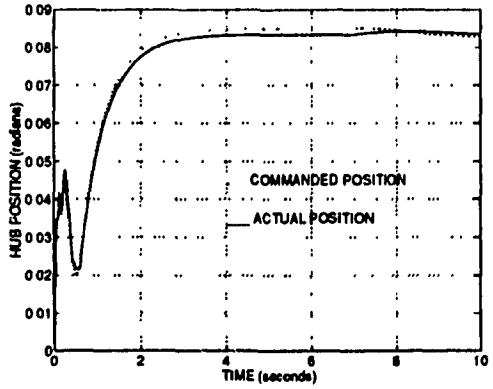

(c)

Figure 4.2 Response of hub position to 0.1 m step reference input. (a) Linear plant, (b) nonlinear plant with ideal hub control, (c) nonlinear plant with PD hub control.

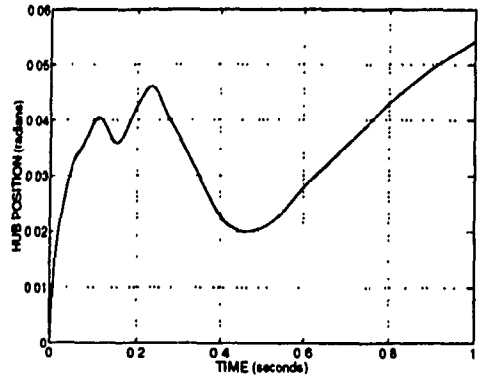

(a)

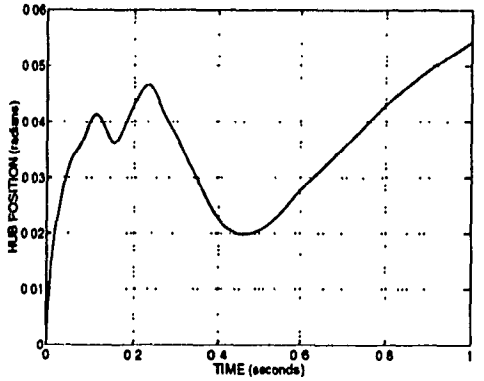

(b)

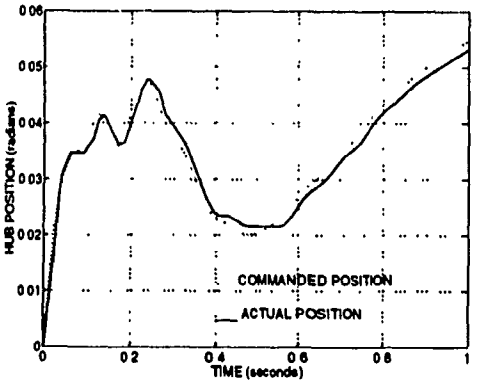

(c)

Figure 4.3 Response of hub position to 0.1 m step input. (a) Linear plant, (b) nonlinear plant with ideal hub control, (c) nonlinear plant with PD hub control.

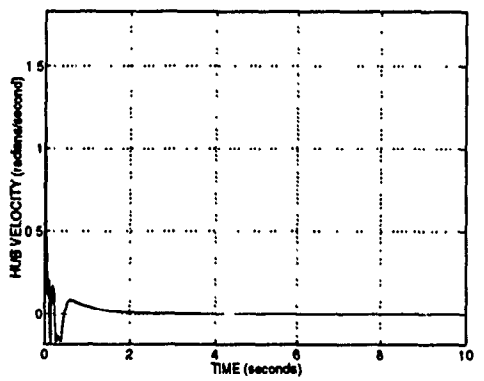

(a)

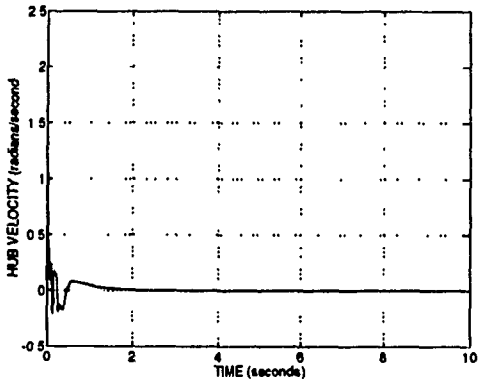

(b)

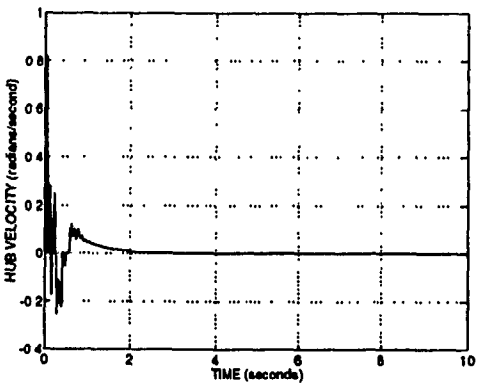

(c)

Figure 4.4 Response of hub velocity to 0.1 m step input. (a) Linear plant, (b) nonlinear plant with ideal hub control, (c) nonlinear plant with PD hub control.

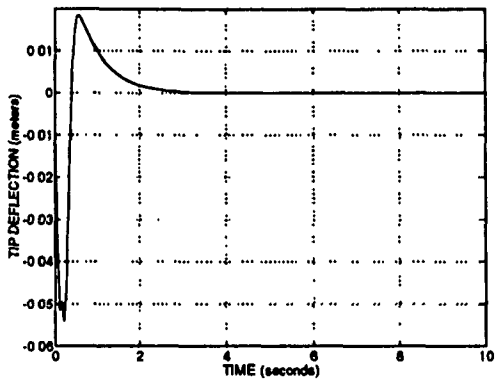

(a)

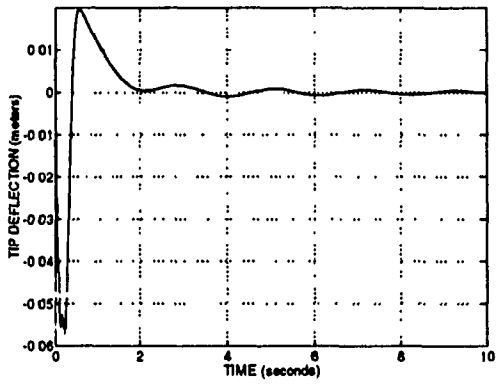

(b)

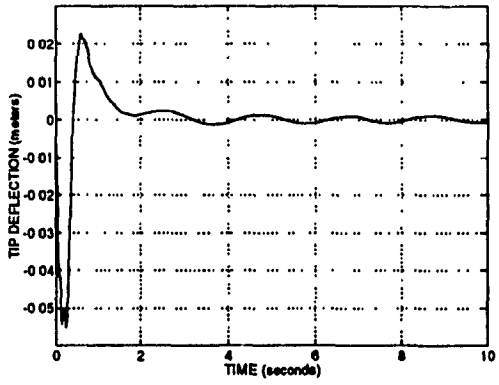

(c)

Figure 4.5 Response of tip deflection to 0.1 m step input. (a) Linear plant, (b) nonlinear plant with ideal hub control, (c) nonlinear plant with PD hub control.

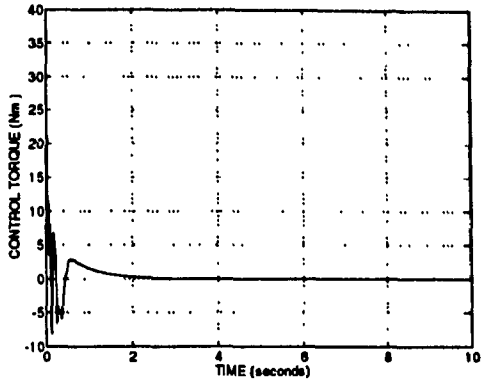

(a)

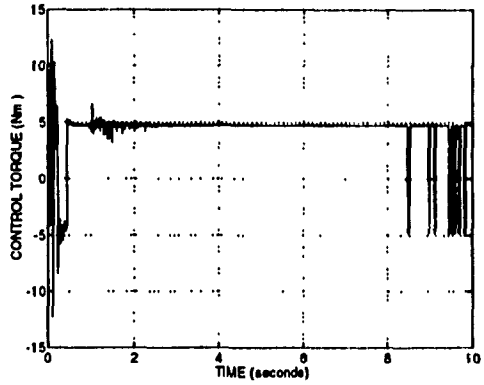

(b)

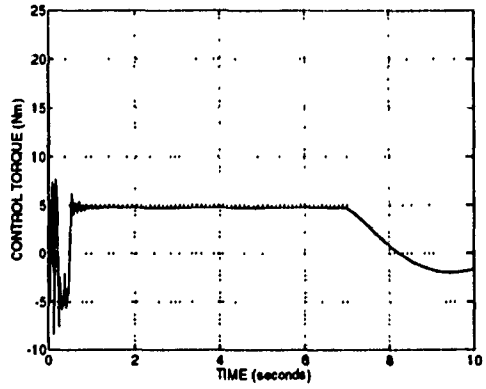

(c)

Figure 4.6 Control torque for 0.1 m step input. (a) Linear plant, (b) nonlinear plant with ideal hub control, (c) nonlinear plant with PD hub control.

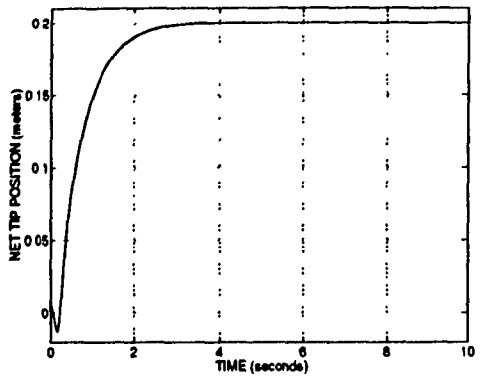

(a)

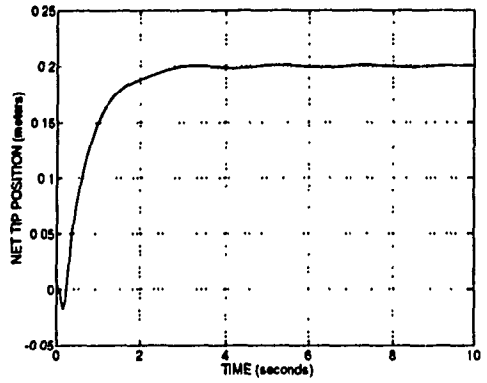

(b)

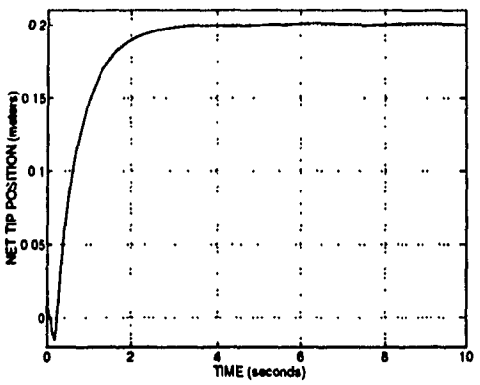

(c)

Figure 4.7 Response of net tip position to 0.2 m step reference. (a) Linear plant, (b) nonlinear plant with ideal hub control, (c) nonlinear plant with PD hub control.

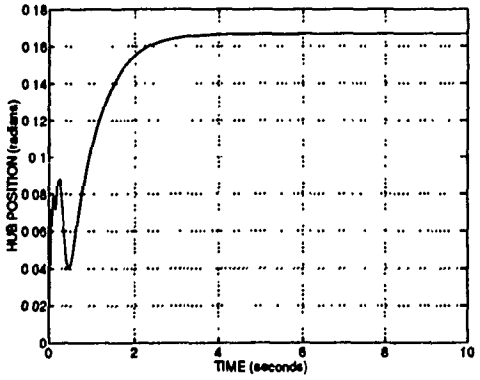

(a)

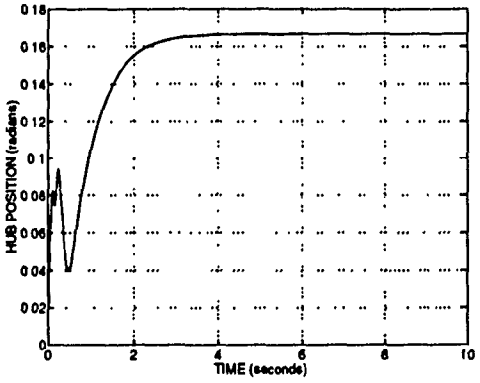

(b)

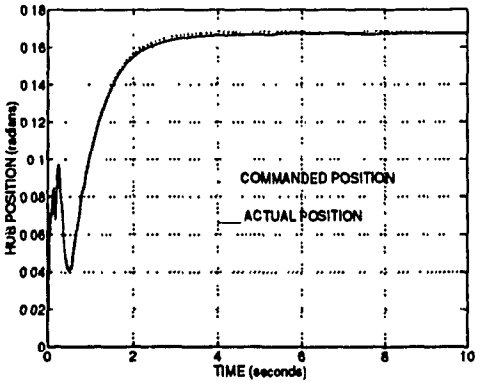

(c)

Figure 4.8 Response of hub position to 0.2 m step reference input. (a) Linear plant, (b) nonlinear plant with ideal hub control, (c) nonlinear plant with PD hub control.

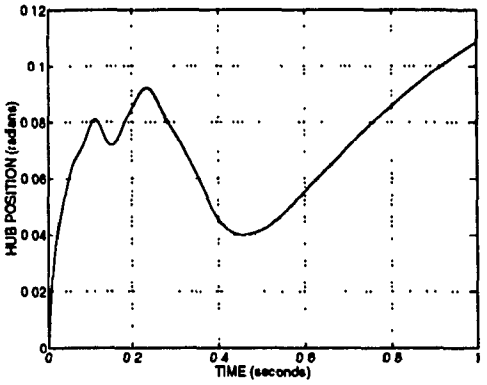

(a)

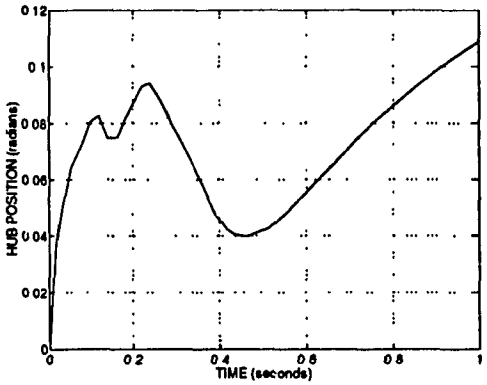

(b)

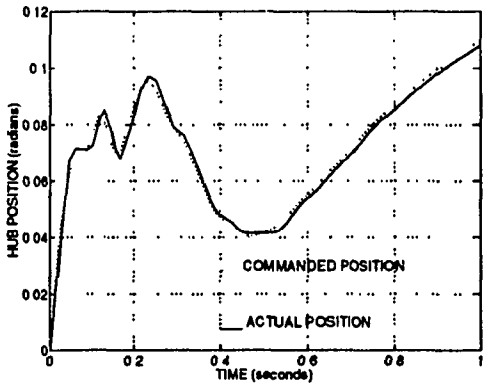

(c)

Figure 4.9 Response of hub position to 0.2 m step input. (a) Linear plant, (b) nonlinear plant with ideal hub control, (c) nonlinear plant with PD hub control.

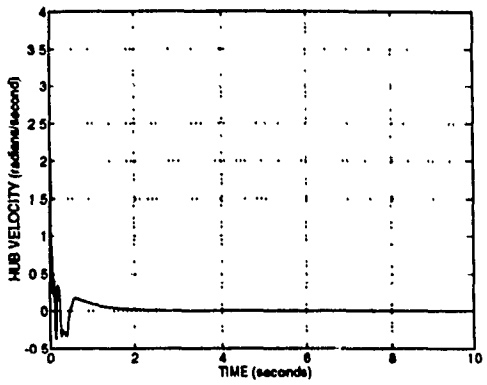

(a)

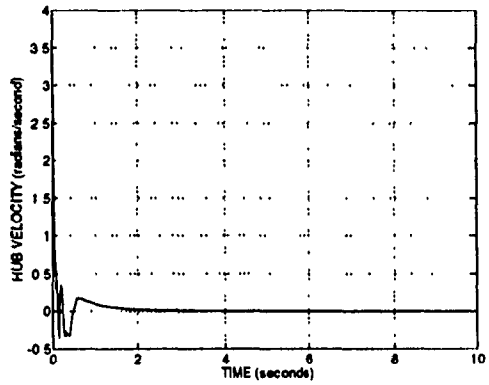

(b)

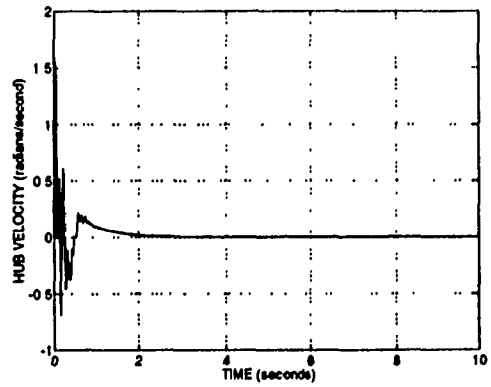

(c)

Figure 4.10 Response of hub velocity to 0.2 m step input. (a) Linear plant, (b) nonlinear plant with ideal hub control, (c) nonlinear plant with PD hub control.

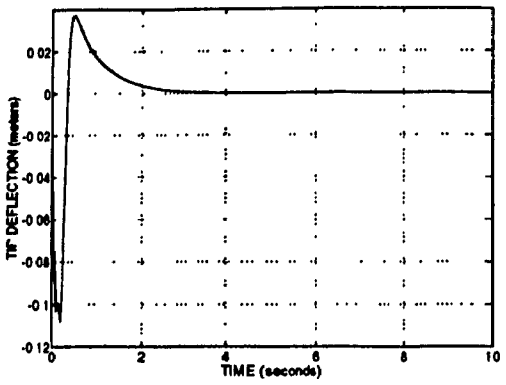

(a)

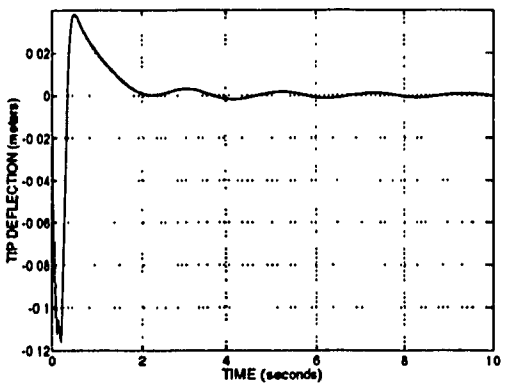

(b)

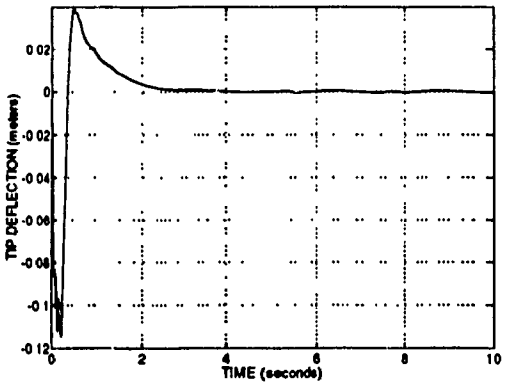

(c)

Figure 4.11 Response of tip deflection to 0.2 m step input. (a) Linear plant, (b) nonlinear plant with ideal hub control, (c) nonlinear plant with PD hub control.

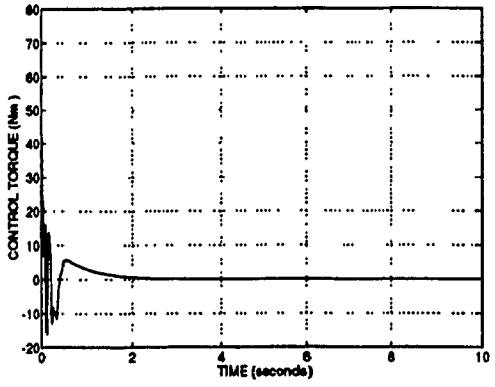

(a)

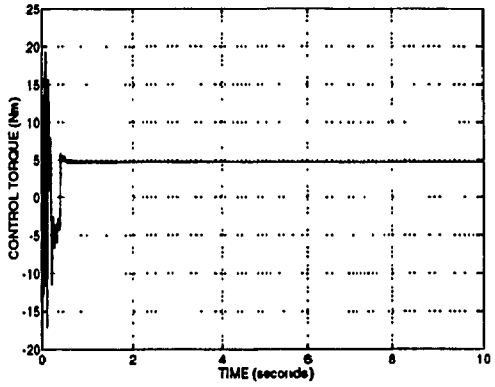

(b)

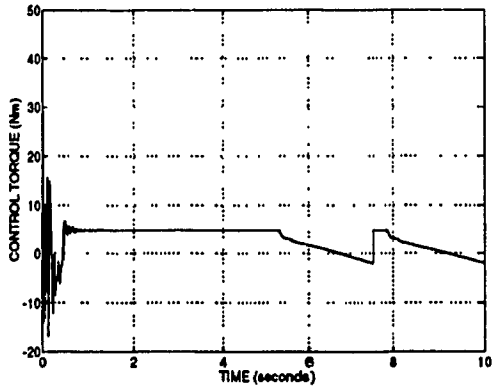

(c)

Figure 4.12 Control torque for 0.2 m step input. (a) Linear plant, (b) nonlinear plant with ideal hub control, (c) nonlinear plant with PD hub control.

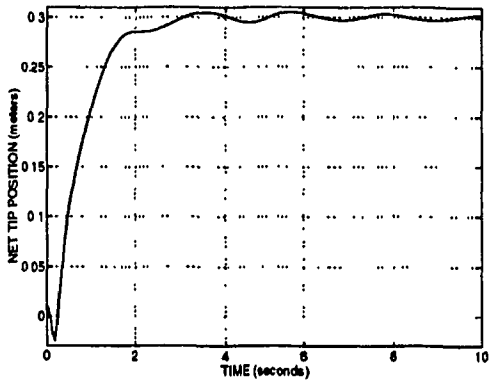

(a) Net tip position.

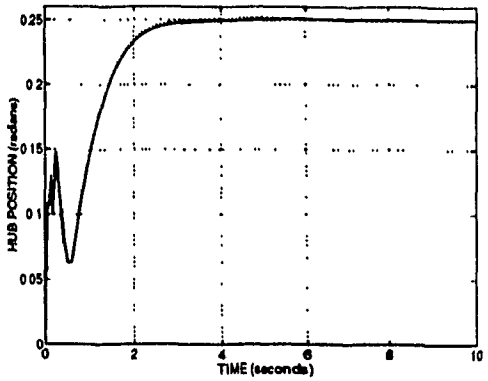

(b) Hub position.

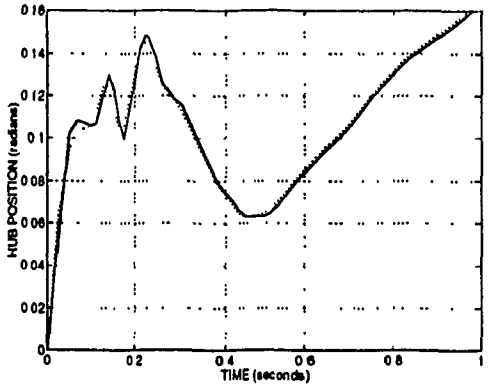

(c) Hub position.

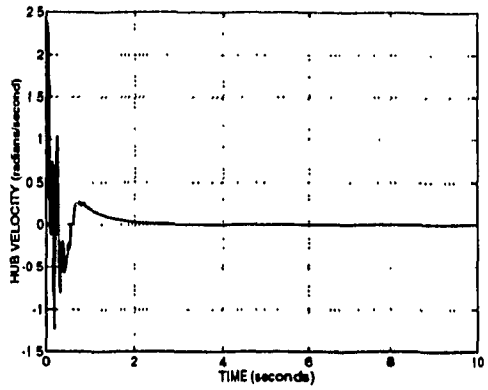

(d) Hub velocity.

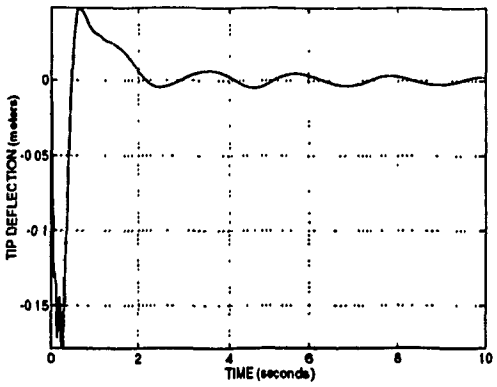

(e) Tip deflection.

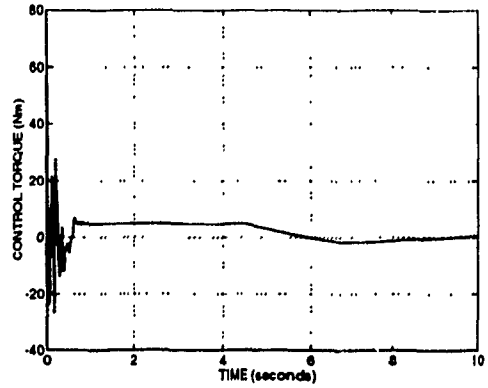

(f) Control torque.

Figure 4.13 Responses to 0.3 m step reference input for nonlinear plant with PD hub control.

4.3 Closed-Loop System With An Inner Loop Design Based On Redefining The Output

This simulation illustrates the performance of the closed-loop system with an inner loop designed according to Section 3.2.2. The inner loop configuration is as shown in Figure 3.11 and uses a full-order observer to obtain an estimate of the states.

Figure 4.14 shows the responses to a reference step input $y_{ref}(t) = 0.1\,\mathrm{m}$ for the linear plant model with ideal hub position control of Eq. (2.97). Not surprisingly, the responses are almost identical to those of the linear plant simulations for the feedthrough compensator of Section 4.2. This similarity is to be expected because (i) the parameters $\hat{c}$, $\hat{d}$ and K_2 have been chosen to yield an inner loop with the same dynamics as transfer function $G_o(s)$, and (ii) the eigenvalues of the observer matrix $\boldsymbol{E}$ have been selected so as not to significantly alter the dynamics of the closed-loop system. A notable difference for the control torques during the transient portion of the simulations. The peak torques for Figures 4.6a and 4.14f are 38.4 Nm and 50.9 Nm, respectively. The larger value of Figure 4.14f is probably due to the transient effect of the observer.

When simulations are conducted using the nonlinear plant model of Eq. (2.89) with PD hub position control, the responses immediately become unstable. The simulations are repeated without the observer, using the actual states of the nonlinear plant as shown in Figure 4.15, to determine whether or not the observer contributes to the instability. (Nonsingular transformation W converts the nonlinear plant state variables $[\,\theta\ \boldsymbol{q}^T\ \dot{\theta}\ \dot{\boldsymbol{q}}^T\,]$ to the state vector $\boldsymbol{v}$ as described in Section 2.4.5. This transformation is required by the design procedure of Section 3.2.2.) The same instability is observed. If the instability had ceased, the observer would obviously be the source of the problem. Since the instability remains, however, the observer may or may not contribute to the instability.

The question arises as to why instability should occur for this particular configuration of inner loop compensation and not for the feedthrough compensator. The reason is probably because the feedthrough compensator uses a dynamical system, $T(s)$,

in the feedforward path to help generate $\hat{y}$. The poles of $T(s)$ are the same as those of the linearized plant $G_l(s)$. The use of $T(s)$ yields a set of zero locations for the augmented plant $\hat{G}(s)$ that have a certain degree of robustness with respect to nonlinearities of the open-loop plant. No such feedforward dynamical system is present, however, for the system of Figure 4.15. Rather, static gain $\hat{d}$ and static gain vector $\hat{c}$ multiply θ_0 and v, respectively. These products are subsequently summed to produce $\hat{y}$. Obviously, the zero locations for the system defined by input θ_0 and output $\hat{y}$ in Figure 4.15 are more sensitive to open-loop plant nonlinearities than are the zeros of $\hat{G}(s)$.

Although simulation of the closed-loop system of Figure 3.11 yields unstable results, the observer might be modified to correct the problem. The observer, after all, is a dynamical system designed to estimate the states of the open-loop linearized plant. Gains $\hat{d}$ and $\hat{c}$ act upon these estimated states to yield $\hat{y}$. Similarly, $T(s)$ incorporates the poles of this same linearized plant, and has been designed to generate $\hat{y}$ as well. The only difference between these two configurations is that $T(s)$ has precisely the same poles as the linearized plant, while the observer attempts to *estimate* the states of the system characterized by these poles. The transient behaviour of the observer differs from that of $T(s)$. Since it is during the initial, transient, portion of the simulation that instability occurs, it seems likely that the transient response of the observer contributes to the problem. Although the observer was redesigned with poles located further within the left-half plane to increase the rate at which the observer transients decay, the same instability persisted. Application of robust observer design techniques may resolve the problem.

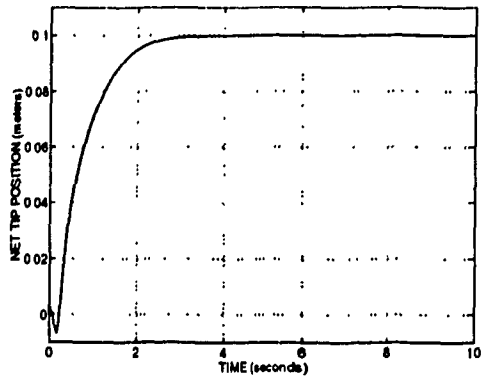

(a) Net tip position.

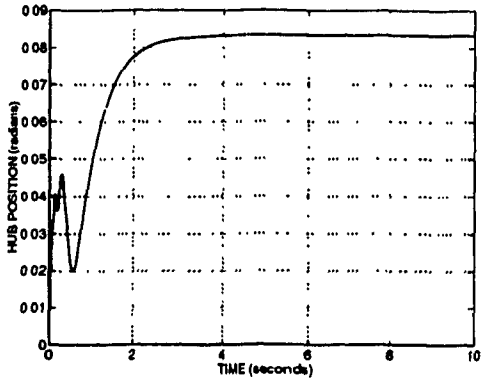

(b) Hub position.

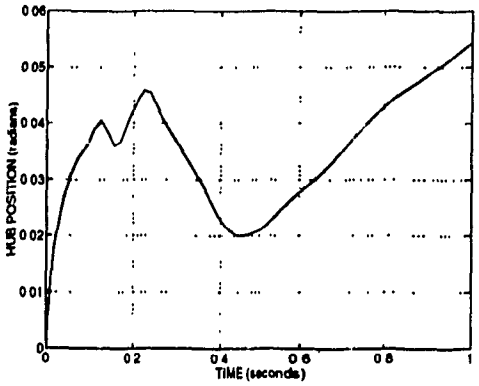

(c) Hub position.

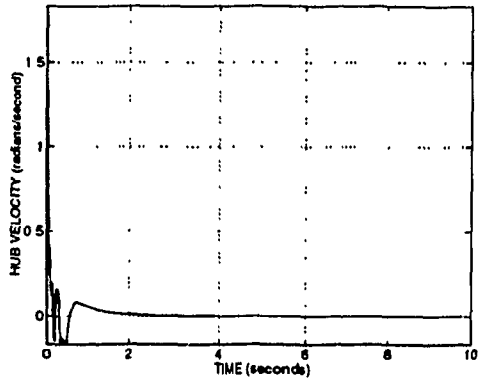

(d) Hub velocity.

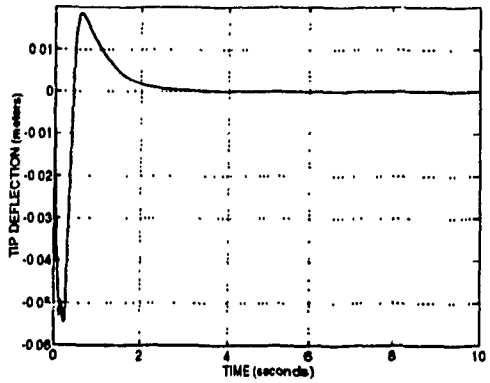

(e) Tip deflection.

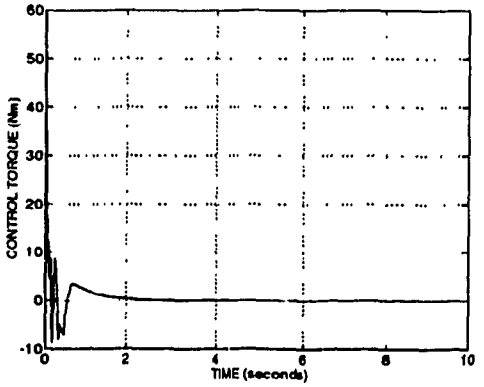

(f) Control torque.

Figure 4.14 Responses to 0.1 m step reference input for closed-loop system with an inner loop design based on redefining the output. The linearized plant model of Eq. (2.97) is used.

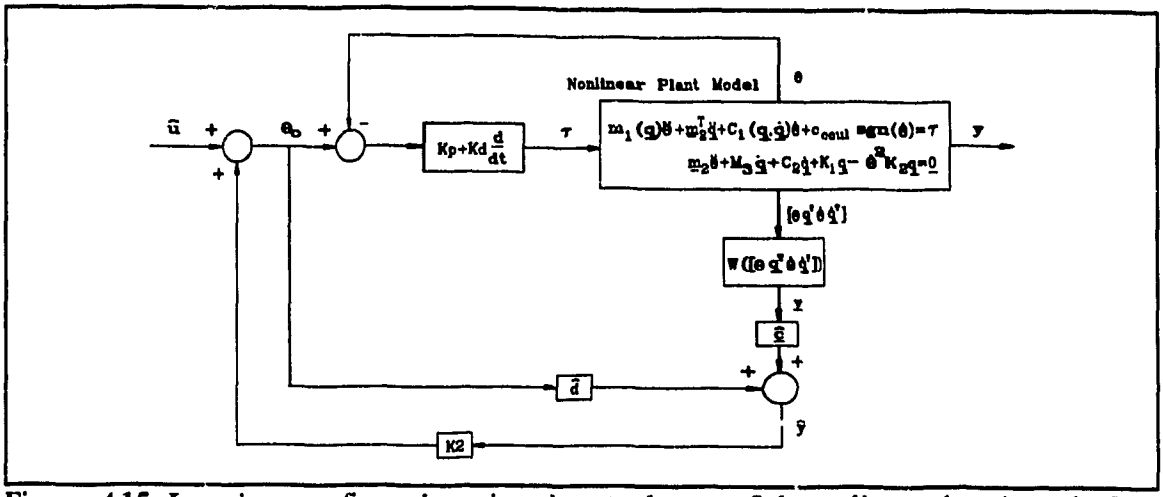

Figure 4.15 Inner loop configuration using the actual states of the nonlinear plant instead of the estimated states generated by the observer.

4.4 Closed-Loop System With An Inner Loop Design Based On Pole Placement State Feedback

This simulation illustrates the performance of the closed-loop system with an inner loop designed according to Section 3.2.3. The inner loop configuration is as shown in Figure 3.13 and uses a full-order observer to obtain an estimate of the states.

Figure 4.16 shows the responses to a reference step input $y_{ref}(t) = 0.1\,\text{m}$ for the linear plant model with ideal hub position control of Eq. (2.97). The responses are almost identical to those of the linear plant simulations of Sections 4.2 and 4.3. This similarity occurs because (i) the parameters f and k have been chosen to yield an inner loop with the same dynamics as transfer function $G_o(s)$, and (ii) the eigenvalues of the observer matrix E have been selected so as not to significantly alter the dynamics of the closed-loop system. As for Section 4.3, the peak control torque is larger than for the feedthrough compensator during the transient period. Again, this is probably caused by the transient effect of the observer.

As is the case for Section 4.3, the simulation becomes unstable when the linearized plant model is replaced with the nonlinear plant model with PD hub position control. Once again, the instability occurs during the initial (transient) period.

A possible cause of instability is the transient response of the observer. Plant model nonlinearities and imperfect hub position tracking may cause errors in the estimated states that, during the transient period, result in an unstable inner loop. As is

suggested in Section 4.3, application of robust observer design techniques may resolve the problem.

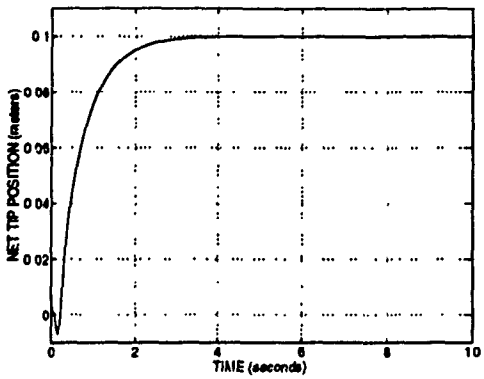

(a) Net tip position.

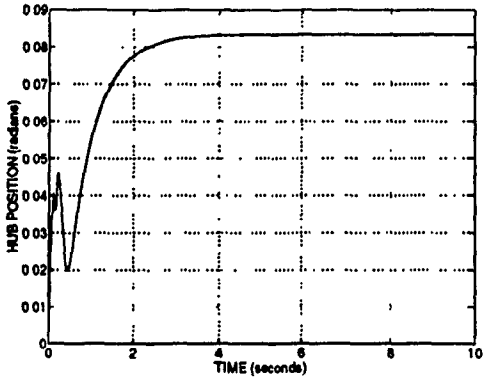

(b) Hub position.

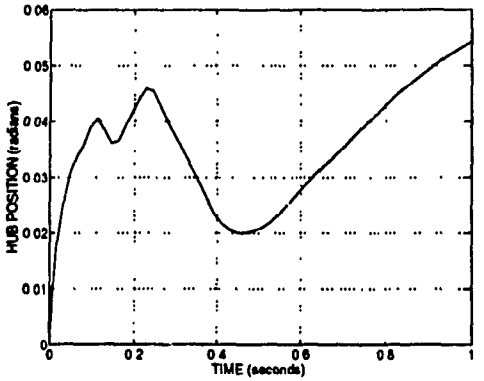

(c) Hub position.

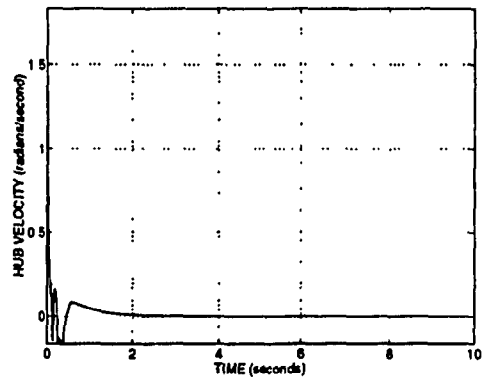

(d) Hub velocity.

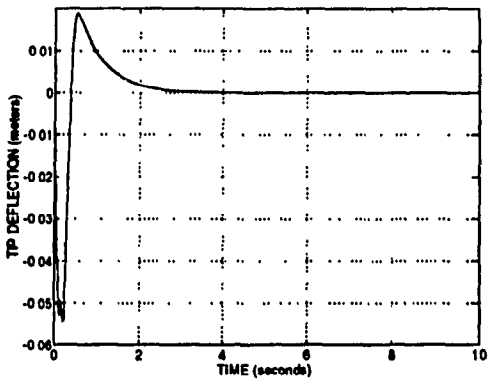

(e) Tip deflection.

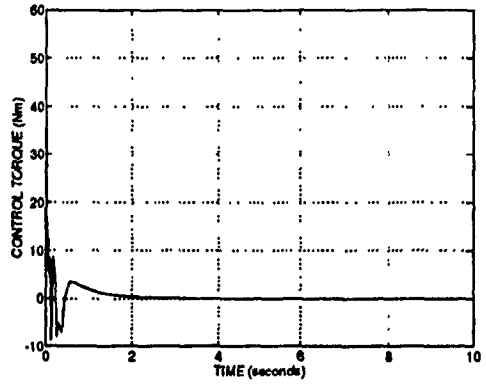

(f) Control torque.

Figure 4.16 Responses to 0.1 m step reference input for closed-loop system with an inner loop design on pole placement state feedback. The linearized plant model of Eq. (2.97) is used.

Chapter 5

Experimental Results

5.1 Introduction

This chapter consists of three sections. Section 5.2 describes the test-bed in detail. Section 5.3 converts the continuous-time control scheme designed in the previous chapter to a discrete-time controller that can be implemented with the Spectrum C30 system card. Section 5.4 presents the closed-loop responses to a variety of reference inputs.

5.2 The Test-Bed

Figure 5.1 is a schematic diagram of the test-bed and control system. The principal components of the system are as follows:

Spectrum TMS320C30 Real-Time System Board

This board implements the control algorithm. It contains a Texas Instruments TMS320C30 Digital Signal Processor (DSP) chip that operates from a 33.3 MHz clock and achieves a performance of 16.7 million instructions per second.

Two separate analog input and output channels are included. Each analog input contains a fourth order lowpass filter to limit noise and provide anti-aliasing protection, a sample and hold amplifier, and a 16-bit analog to digital converter (ADC). Each analog output consists of a 16-bit digital to analog converter (DAC) and a fourth order lowpass filter to smooth the otherwise stepped DAC output signal. The full scale analog input and output ranges are ±3 volts.

The board is mounted in a 16-bit expansion slot within the Compaq 386 20/e host

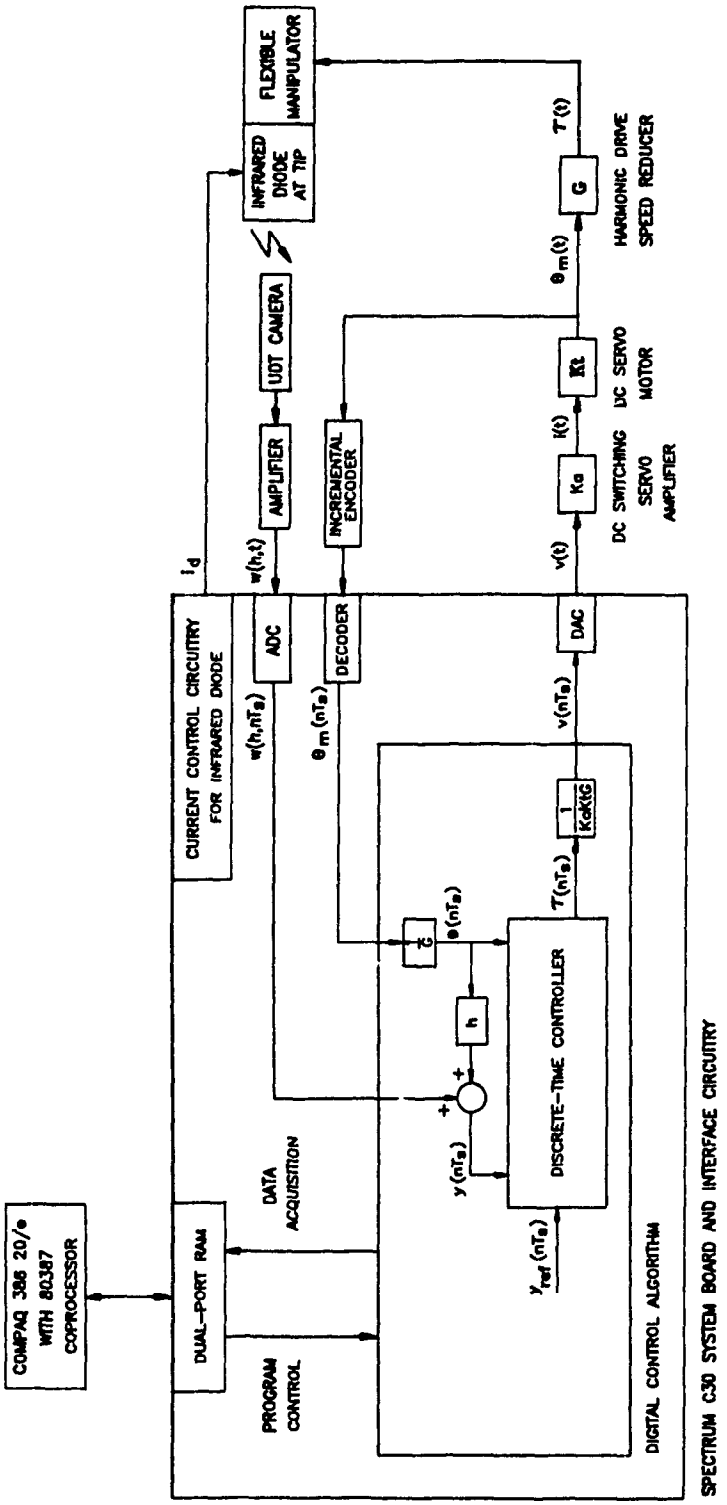

Figure 5.1 Experimental test-bed.

computer. Data is exchanged between the host and the C30 board by 64K x 32 bit words of dual-port RAM.

The TMS320C30 DSP chip includes an expansion bus that is used to connect to a separate interface board. This interface board contains programmable timing circuitry and high current sources that control the pulsed current which drives the infrared diode mounted at the flexible arm's tip. The interface board also incorporates circuitry that decodes the motor position information.

Compaq 386 20/e Host Computer

The host serves as a platform for the C30 board and allows the user to interact with the control program implemented on the C30 board. Experimental data is transferred from the C30 board to the host's memory for subsequent analysis.

DC Switching Servo Amplifier

The Copley Controls Corp. Model 215 is a pulse-width modulated switching amplifier designed to drive DC motors. The Model 215 is configured as a transconductance amplifier for which a voltage $v(t)$ at the input results in a proportional output current $i_a(t) = K_a v(t)$, independently of the output impedance. (An internal control loop senses the output current and maintains the fixed proportionality factor K_a = 2.0). The full scale DAC voltage range of ±3 volts results in a maximum current range of ±6 amperes. The 3-dB bandwidth of the amplifier is 1000 Hz.

DC Servo Motor

As described in Section 2.4.2, the EG&G Torque Systems Model MH3310-055G1 permanent magnet, brush type DC servo motor develops a torque $\tau_m(t) = K_t i_a(t)$, where $K_t = 0.1175$ Nm/A. With an armature current range of ±6 amperes, the maximum torque range generated by the motor is ±0.705 Nm.

Incremental Encoder

The Motion Control Devices, Inc. Model M21 is an optical encoder that provides incremental resolutions of 500 cycles per revolution of the motor shaft on each of two quadrature (A & B) signals.

Decoder

The Hewlett Packard HCTL-2020 is an integrated circuit that performs quadrature decoder, counter, and bus interface functions. The two incoming quadrature signals from the encoder are decoded. The resolution of 500 cycles per revolution is multiplied by a factor of four to yield a resolution of 2000 cycles per revolution of the motor shaft. An on-chip 16-bit binary up/down counter allows for software computation of absolute position.

Speed Reducer

Since the motor is a high-speed, relatively low-torque actuator, it is geared down to provide sufficient torque to drive the load. The HD Systems, Inc. Model RH20-CC harmonic drive speed reducer connects the motor shaft to the flexible manipulator's hub. A gear ratio of 50:1 ensures that sufficient torque is available to accelerate the hub. The speed reducer amplifies the motor torque by a factor of 50 and yields an output torque range of ±35.25 Nm. Harmonic drive gearing results in minimal backlash which is essential for reducing position error at the manipulator's tip. The positional resolution of 2000 cycles per revolution of the motor shaft is equivalent to $50 \times 2000 = 100000$ cycles per revolution of the speed reducer's output shaft. However, the counter of the decoder is limited to 16 bits, corresponding to a maximum count of 65535 cycles. With one complete revolution of the output shaft equivalent to 100000 cycles, the decoder can accommodate $\frac{65535}{100000} \times 2\pi = 1.31\pi$ radians of rotation before overflowing.

Infrared Emitting Diode

The positional resolution of the tip's deflection is proportional to the signal to noise ratio (S/N) of the received signal at the output of the UDT camera. One way of maximizing the S/N is to use a high powered light source. The Opto Diode OD-50L Super High-Power GaAlAs infrared emitting diode supplies up to 0.6 watts of peak optical power at a wavelength of 880 nm. An infrared light source, when used with a camera that incorporates a visible light blocking filter, reduces the interference from ambient light. Due to thermal limitations, the maximum amount of power is attainable only when the diode current is pulsed and its duty cycle is minimized. The current control circuitry on the interface board allows adjustment of the peak current level and the duty cycle.

UDT Camera

The United Detector Technology Model 274 camera consists of a wide angle lens and a lateral-effect photodiode detector assembly. The 12.5 mm C-mount lens has a 55° field of view and includes a visible light blocking filter. The lens focuses the image of the infrared diode onto an SC-10D photodiode detector. The diode appears as a spot of light on the detector's surface and induces currents at each of the contacts of the detector. Since the magnitude of the current at a particular contact is proportional to the contact's proximity to the spot of light, the relative magnitudes of the currents are used to determine the absolute position of the spot. By an appropriate calibration procedure, the absolute position of the infrared diode and the deflection of the tip are also calculated.

UDT Amplifier

The United Detector Technology Model 301DIV signal conditioning amplifier interfaces the SC-10D photodiode detector to the ADC on the C30 board. The amplifier converts the incoming low-level currents to a position-related analog output voltage. The amplifier is adjusted so that maximum tip deflections of ±0.25 m correspond to output voltages of ±3 volts. The 55° field of view of the lens should allow measurement of tip deflections in excess of ±0.5 m. As the magnitude of the tip deflection increases, however, so does

the magnitude of the slope of the arm evaluated at the tip, $\left|\frac{\partial w(h,t)}{\partial x}\right|$. This slope causes a rotation of the diode when viewed from the camera's frame of reference. The increasing slope, when coupled with the narrow beamwidth of the infrared diode results in a reduction of the optical power received at the lens. Beyond a deflection of ±0.25 m, the diode cannot be accurately detected by the camera even though it is still within the lens's field of view.

Noise and nonlinearities within the photodiode detector result in a measurement error of ±2.5 mm within a deflection range of ±0.01 m. As the deflection increases to a maximum of ±0.25 m, the error increases to ±10 mm.

5.3 Digital Implementation of the Controller

Figure 5.2 shows the closed-loop system in which the inner control loop has been

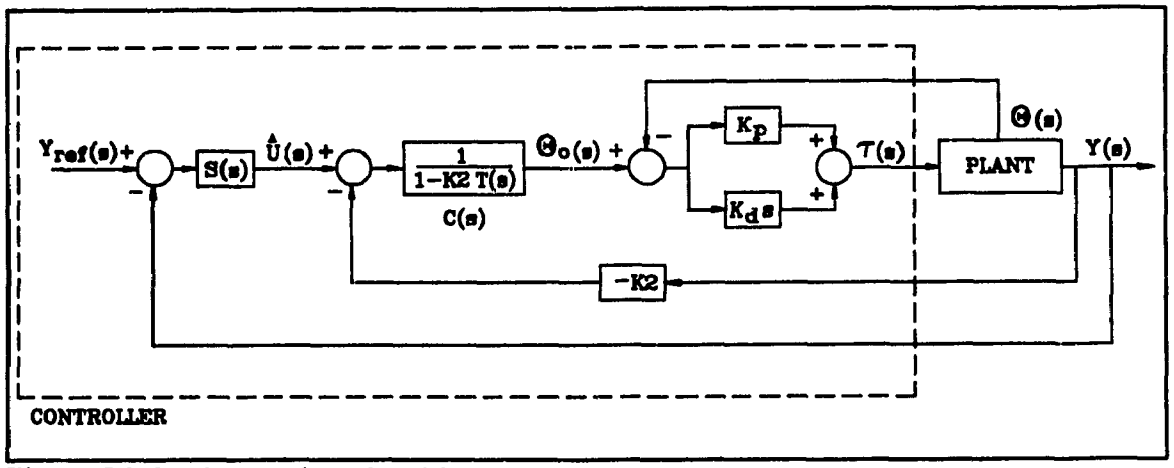

Figure 5.2 Continuous time closed-loop system.

reconfigured in the format of the basic feedback control loop of Figure 3.6. The servo amplifier, servo motor, speed reducer, plant, infrared emitting diode, UDT camera and UDT amplifier constitute a continuous-time system. The DSP, on the other hand, is discrete-time in nature. For implementation on the C30 board, the continuous-time controller must be converted to a discrete-time controller.

As a first step toward implementing a discrete-time controller, write the open-loop equation of the controller relating $Y_{ref}(s)$, $Y(s)$ and $\Theta(s)$ to $\tau(s)$:

$$\tau(s) = \left\{ \left[\left(Y_{ref}(s) - Y(s) \right) S(s) + K_2 Y(s) \right] C(s) - \Theta(s) \right\} \quad . \tag{5.1}$$

Rewrite Eq. (5.1) by substituting $C(s) = \dfrac{q(s)}{q(s) - K_2 p_t(s)}$ and $S(s) = \dfrac{K_1}{s}$:

$$\tau(s) = Y_{ref}(s) \left[\frac{K_1 q(s) [K_p + sK_d]}{s[q(s) - K_2 p_t(s)]} \right] - \Theta(s) \left(K_p + sK_d \right) + Y(s) \left[\frac{[s^2 K_d K_2 + s(K_p K_2 - K_1 K_d) - K_1 K_p] q(s)}{s[q(s) - K_2 p_t(s)]} \right] . \tag{5.2}$$

In vector notation, Eq. (5.2) becomes

$$\tau(s) = g(s) \begin{pmatrix} Y_{ref}(s) \\ \Theta(s) \\ Y(s) \end{pmatrix} \tag{5.3}$$

where $g(s) = \left[g_1(s) \;\; g_2(s) \;\; g_3(s) \right]$, and

$$g_1(s) = \frac{K_1 q(s) [K_p + sK_d]}{s[q(s) - K_2 p_t(s)]} \tag{5.4a}$$

$$g_2(s) = -(K_p + sK_d) \tag{5.4b}$$

$$g_3(s) = \frac{[s^2 K_d K_2 + s(K_p K_2 - K_1 K_d) - K_1 K_p] q(s)}{s[q(s) - K_2 p_t(s)]} \quad . \tag{5.4c}$$

The controller defined by Eq's. (5.1) through (5.4) is a multivariable system with the three inputs $Y_{ref}(s)$, $\Theta(s)$, and $Y(s)$, and a single output $\tau(s)$.

The problem at hand is to emulate the system of Eq. (5.3) on the C30 board, a task represented by Figure 5.3.

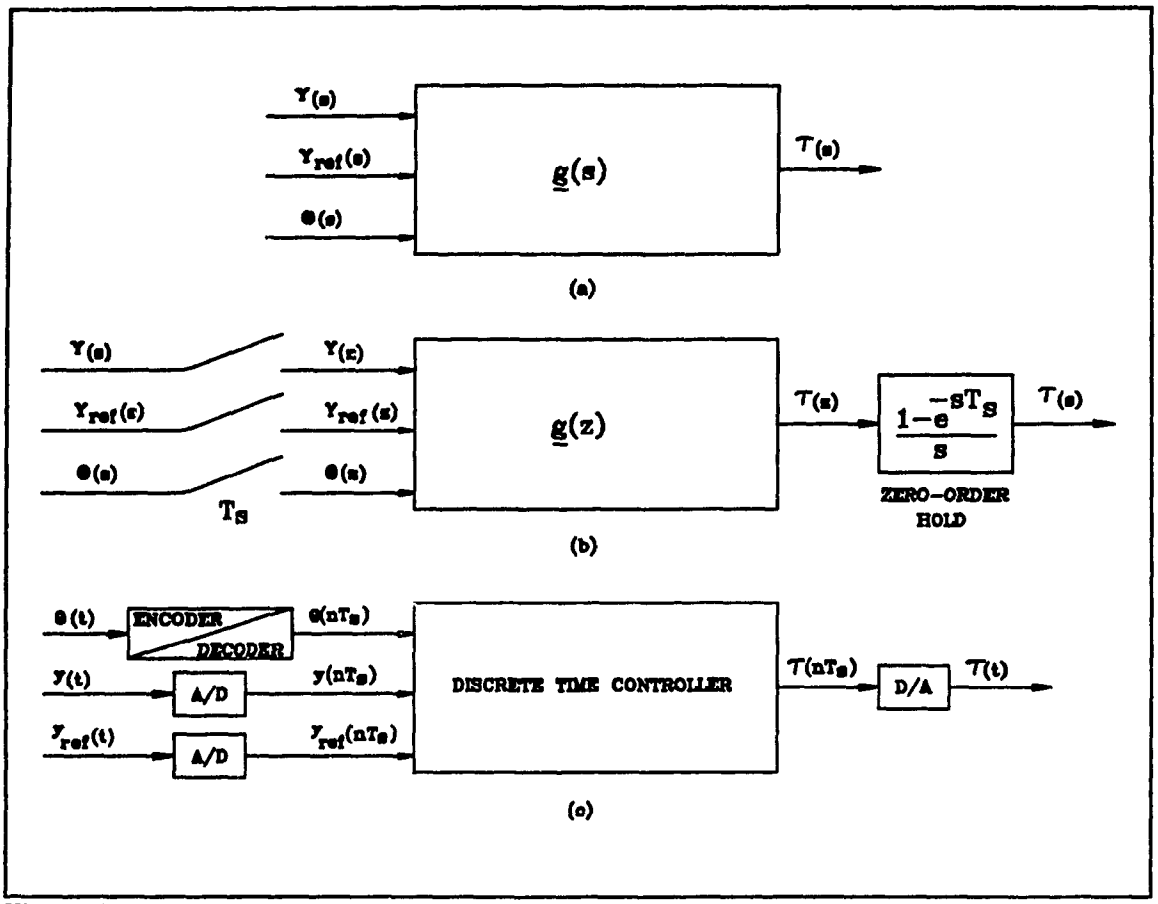

Figure 5.3 Transforming the continuous controller: (a) continuous design of Eq. (5.3); (b) *z*-domain approximation; (c) digital implementation.

The bilinear *z*-transform is used to obtain a discrete-time equivalent of $g(s)$ as follows:

$$g(z) = g(s)\Big|_{s=\frac{2}{T_s}\frac{1-z^{-1}}{1+z^{-1}}} .$$

This transformation maps the left half of the *s*-plane, band limited by the sampling frequency $\frac{1}{T_s}$, into the unit circle in the *z*-plane. It is therefore important to choose a sampling period T_s sufficiently small so that all the *s*-domain poles are included. The bilinear *z*-transform always generates stable poles in the *z*-domain if the original *s*-plane poles are stable.

Nyquist's sampling theorem requires that a signal be sampled at a frequency equal to at least twice its highest frequency component. Subsequent *ideal* low-pass filtering will

allow the recovery of the original signal with no loss of information. Since such an ideal filter is not realizable, practical sampling is performed at frequencies higher than the Nyquist frequency. In the context of the problem at hand, this means that the sampling frequency, $f_s = \frac{1}{T_s}$, should theoretically equal at least twice the maximum closed-loop frequency component. In practice, though, f_s should be substantially higher.

In Section 3.3, the largest closed-loop frequency was found to be 101.3 rad/s (16.1 Hz). The closed-loop system, however, neglects the effects of the hub position controller. Analysis of the simulated hub position responses of Chapter 4 provides some indication of the frequency components found in the hub position signal. The fastest hub response, shown in Figure 4.13c, occurs for the case of a 0.3 m step reference input. The highest frequency components occur during the portion of the curve with the fastest rise time, that is, during the time interval from 0 to 0.058 s. During this interval, the hub position varies from 0 to 0.107 rad. The rise time for this interval is defined as the time required for the hub position to rise from 10% to 90% of its final value of 0.107 rad, and is calculated to be 0.040 s. One criterion for sample period selection is to choose T_s to be less than one-tenth of the system rise time, that is, less than 0.004 s.

The value selected for T_s is 0.002 s. T_s corresponds to a sampling frequency of 500 Hz which is more than thirty times greater than the largest closed-loop frequency of 16.1 Hz found in Section 3.3.

Direct application of the bilinear z-transform to the high order transfer functions $g_1(s)$ and $g_3(s)$ is a numerically ill conditioned approach that may yield inaccurate results. A better technique involves a partial fraction expansion of each transfer function. Each partial fraction is then transformed into the z-domain.

Expansion of $g_1(s)$ and $g_3(s)$ yields:

$$g_1(s) = \sum_{i=1}^{4} \frac{a_{i_0}s^2 + a_{i_1}s + a_{i_2}}{s^2 + b_{i_1}s + b_{i_2}} + \frac{a_5}{s} + a_6 \tag{5.5}$$

$$g_3(s) = \sum_{i=1}^{4} \frac{c_{i_0}s^2 + c_{i_1}s + c_{i_2}}{s^2 + b_{i_1}s + b_{i_2}} + \frac{c_5}{s} + c_6 s + c_7 \ . \tag{5.6}$$

The second-order polynomials in Eq's. (5.5) and (5.6) all have complex-conjugate roots.

Note the occurrence of the derivative term s in Eq's. (5.4b) and (5.6). At high frequencies, the gain corresponding to this term becomes very large and leads to amplification of high-frequency noise. A good approximation to the term s for signals whose frequency contents are below $\frac{2}{T_s}$ rad/s, that minimizes the noise problem is

$$s \approx \frac{s}{1 + sT_s/2} \ .$$

Introduction of the pole at $s = -\frac{2}{T_s}$ s^{-1} limits the maximum gain to $\frac{2}{T_s}$.

Application of the bilinear z-transform to Eq's. (5.4b), (5.5) and (5.6), with the previous approximation to the term s, yields the following expressions for $g_1(z)$, $g_2(z)$ and $g_3(z)$:

$$g_1(z) = \sum_{i=1}^{4} \frac{d_{i_0} + d_{i_1}z^{-1} + d_{i_2}z^{-2}}{1 + e_{i_1}z^{-1} + e_{i_2}z^{-2}} + \frac{d_5 + d_6 z^{-1}}{1 - z^{-1}} + d_7 \tag{5.7}$$

$$g_2(z) = -\left(K_p + \frac{K_d[1 - z^{-1}]}{T_s} \right) \tag{5.8}$$

$$g_3(z) = \sum_{i=1}^{4} \frac{f_{i_0} + f_{i_1}z^{-1} + f_{i_2}z^{-2}}{1 + e_{i_1}z^{-1} + e_{i_2}z^{-2}} + \frac{f_5 + f_6 z^{-1}}{1 - z^{-1}} + \frac{f_7[1 - z^{-1}]}{T_s} + f_8 \ . \tag{5.9}$$

Taking the z-transform of Eq. (5.3) yields

$$\tau(z) = g(z)\begin{pmatrix} Y_{ref}(z) \\ \Theta(z) \\ Y(z) \end{pmatrix} . \tag{5.10}$$

Expanding Eq. (5.10) gives

$$\tau(z) = g_1(z)\,Y_{ref}(z) + g_2(z)\,\Theta(z) + g_3(z)\,Y(z) . \tag{5.11}$$

To implement the discrete time controller shown in Figure 5.3c, Eq. (5.11) is expressed in the time domain as a series of difference equations that relate $y_{ref}(nT_s)$, $\Theta(nT_s)$ and $y(nT_s)$, (and their values at sample times $(n-1)T_s$ and $(n-2)T_s$), to $\tau(nT_s)$.

5.4 Experimental Responses

Except where otherwise noted, all responses are obtained using a controller that digitally implements a continuous-time controller with the same parameters used to generate the simulations of Figures 4.1 through 4.13. Specifically, K_1=1850, K_2=-100, K_p=3000 and K_d=25. The numerator and denominator polynomials of the feed-through compensator $T(s)$ are as defined in Section 3.2.1.

The control torque plots represent the values demanded by the controller. When within the saturation limits of ±34.7 Nm imposed by the system hardware, the plots accurately represent the actual torque applied to the hub. When the plots exceed the saturation limits, the actual torque is restricted to ±34.7 Nm.

$y_{ref}(t) = 0.1$ m

Figure 5.4 shows the responses of the closed-loop system to a reference step input $y_{ref}(t)$=0.1 m. The simulated responses for the nonlinear plant with PD hub control are included for comparison purposes, and are represented by the dashed plots. The net tip

position of Figure 5.4a reaches its steady-state value in slightly more than 2 s, which is close to the value observed for the simulation of the nonlinear plant with PD hub control. A major difference between the two plots, though, is that while the simulation exhibits a 3 rad/s oscillation that persists well after 2 s, the experimental response does not. Conversely, the experimental response contains a 19 rad/s oscillation during the first two seconds, an oscillation that is not present for the simulation.

Examination of the hub position in Figure 5.4c reveals that for $0 \leq t \leq 0.05$ s, the hub position remains at 0 rad. This delay is caused by hub stiction. The integrating action of the servo compensator causes an increase of the control torque. The net result is a disturbance effect at the hub that introduces a 19 rad/s oscillation of the tip deflection during first 2 seconds, (shown in Figure 5.4e), an oscillation that appears in the net tip position. This oscillation is caused by excitation of the second flexible mode that has a natural frequency of 19 rad/s. No such delay occurs for the simulation, and therefore no such oscillation is induced.

The absence of any oscillation in the experimental net tip position after 2 s is most likely caused by the additional damping effect of Coulomb friction inherent in the flexible arm. No oscillation appears in the experimental tip deflection during this time interval, in contrast to the simulated tip deflection of Figure 4.5c. Since Coulomb friction in the arm is not incorporated into the plant model, the oscillation is not suppressed in the simulated tip deflection.

In contrast to the nominal steady state value of 0 mm for the simulated tip deflection, a steady state experimental tip deflection of 6.6 mm is observed. This nonzero value is caused by Coulomb friction in the arm. The controller compensates by maintaining the steady state hub position at 0.078 rad instead of the value of 0.083 rad for the simulated hub position.

Control torque saturation occurs, as evidenced by the maximum demanded torque value of over 100 Nm in Figure 5.4f. A significant amount of noise is also present, which is caused by the derivative approximation term in $g_3(z)$. By acting upon $Y(z)$, which is a function of the hub angle and the tip deflection, this term amplifies the noise inherent in

the UDT camera and amplifier. Friction and inertia of the hub attenuate this high frequency noise so that its effect on the hub position, tip deflection and net tip position is minimal.

$y_{ref}(t) = 0.2$ m

The experimental net tip position of Figure 5.5a shows an faster rise time and an increased amplitude of the 19 rad/s oscillation during the first 2 s than observed for Figure 5.4a. This frequency is superimposed upon a 3 rad/s oscillation whose amplitude decays to zero at approximately 3 s. The larger value for $y_{ref}(t)$, when combined with the integral action of the servo compensator and the delay of the hub position response, results in a larger peak value of the demanded control torque. Although the actual applied torque is limited to a maximum of 34.7 Nm for both cases, integrator windup causes the applied torque to remain at its saturated value for a greater period of time. This creates a greater disturbance effect upon the tip deflection, (that excites the first two flexible modes), than occurs for $y_{ref}(t) = 0.1$ m.

$y_{ref}(t) = 0.3$ m

As shown in Figure 5.6a, the amplitudes of the 3 rad/s and 19 rad/s oscillations are even larger than for $y_{ref}(t) = 0.2$ m. Once again, integrator windup amplifies the disturbance effect caused by stiction-induced delay of the hub response.

$y_{ref}(t) = 0.2$ m, $K_1 = 1150$

From the previous discussion, controller performance degrades as the magnitude of the step reference input increases. As a solution to this problem, consider reducing servo gain K_1. While such a gain reduction has the effect of increasing the rise time of

the output, it should also bound the demanded control torque and curb the problem of integrator windup.

Figure 5.7 shows the responses to a reference step input $y_{ref}(t) = 0.2$ m for a servo gain $K_1 = 1150$. All other controller parameters are unchanged. The time to steady state of the output in Figure 5.7a is about 4 s, approximately double that of the response to $y_{ref}(t) = 0.1$ m in Figure 5.4a. The amplitudes of the 3 rad/s and 19 rad/s are substantially less than for $y_{ref}(t) = 0.2$ m and $K_1 = 1850$. Note that the peak demanded control torque of Figure 5.7f is slightly less than 100 Nm, while the peak torque value of Figure 5.5f is 200 Nm. Thus, integrator windup and disturbance effects are reduced.

A New Reference Input: Ramp To Constant Position

An important contributing factor to the problem posed by integrator windup and disturbance effects is the nature of the reference input. The selection of a step signal for $y_{ref}(t)$ implies an infinitely fast transient response of the output that can result in large demanded control torques. Selection of another type of reference input that does not contain large step discontinuities reduces the torque requirement and improves the performance.

Such an input is shown as the dotted curve in Figure 5.8a. It consists of a ramp that increases to a value of 0.5 m in 0.25 s, at which point it remains constant. The objective here is not to track the ramp portion of the input, but rather to achieve set-point tracking of $y_{ref}(t) = 0.5$ m.

The net tip position reaches and remains at the 0.5 m steady state value within 4 s. The largest amplitude reference step input that can be reached in this same amount of time, with no subsequent deviation, is 0.2 m. As shown in Figure 5.8f, the peak demanded control torque is 50 Nm which is less than half the value observed for a reference step input of 0.1 m.

Hub Control

For comparison purposes, Figure 5.9 shows the results of applying a step input to a system that implements only a PD control of the hub position. The proportional and derivative gains are identical to those used for the hub position control loop implemented as part of the net tip position controller: specifically, $K_p = 3000$ and $K_d = 25$. Such a controller can be effectively used for a rigid arm since the net tip position is equal to the hub position multiplied by the (constant) length of the arm. Good control of the hub is therefore equivalent to good control of the net tip position.

Figure 5.9a shows that the overshoot of the net tip position response exceeds 100%. A steady-state value is reached at approximately 7 s. Figures 5.9b and 5.9c show that the hub position overshoots its steady state value by 26%. Obviously, this behaviour contributes to the net tip position overshoot. The significant fact is that the net tip position controller is a significant improvement upon a controller that fails to compensate for the nonminimum phase characteristics of the plant.

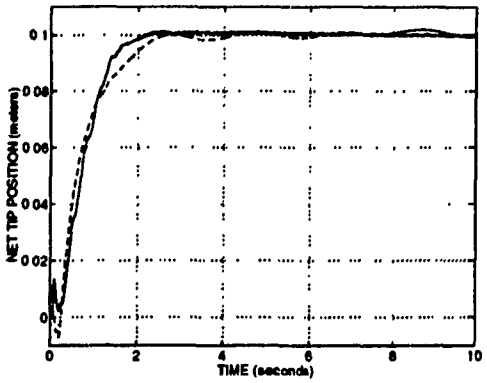

(a) Net tip position.

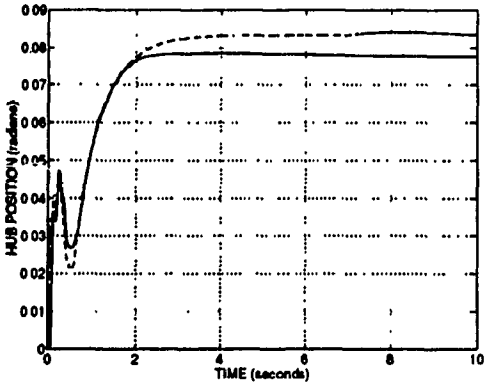

(b) Hub position.

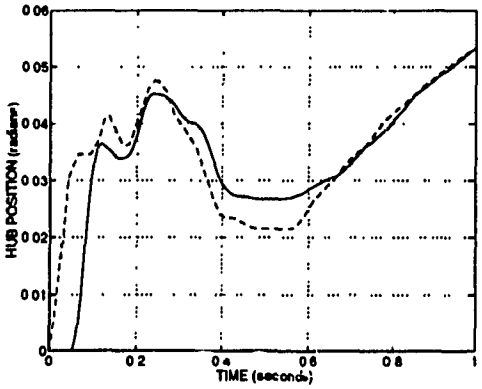

(c) Hub position.

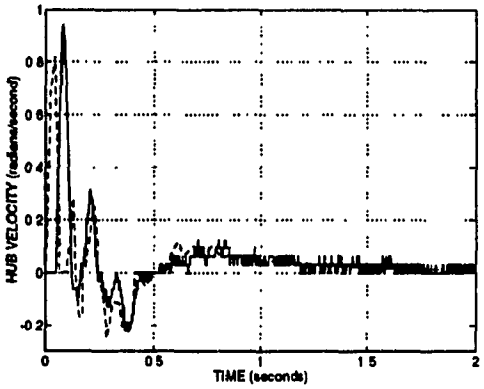

(d) Hub velocity.

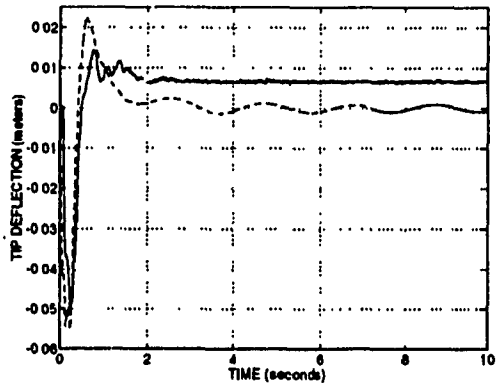

(e) Tip deflection.

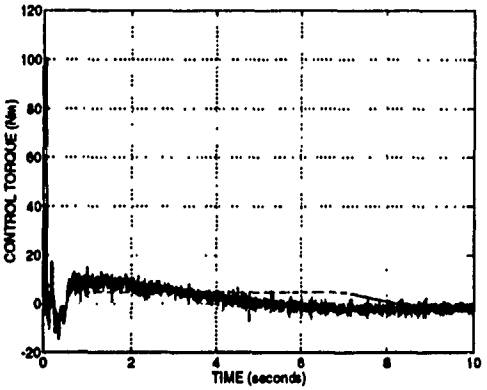

(f) Control torque.

Figure 5.4 Experimental responses (solid line) and simulated responses for nonlinear plant with PD hub control (dashed line), to 0.1 m step reference input.

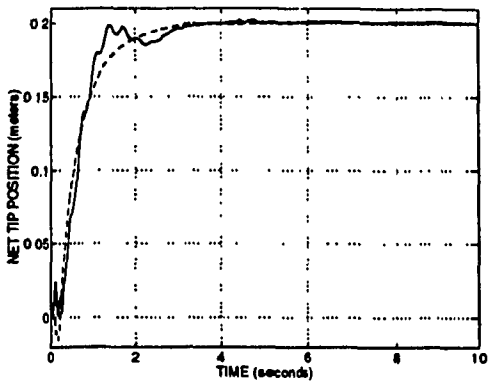

(a) Net tip position.

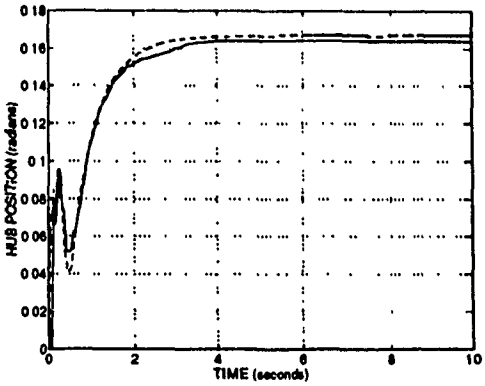

(b) Hub position.

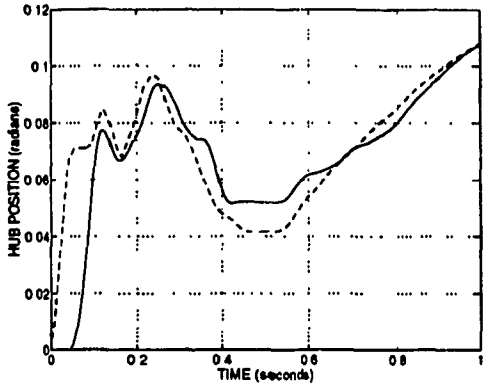

(c) Hub position.

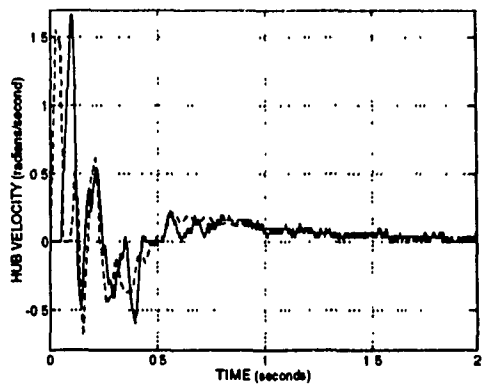

(d) Hub velocity.

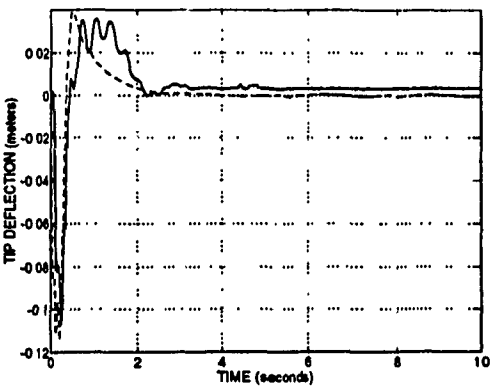

(e) Tip deflection.

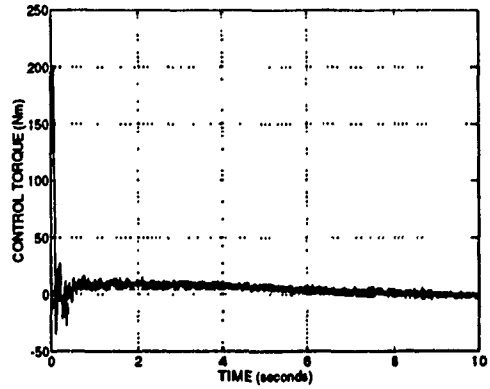

(f) Control torque.

Figure 5.5 Experimental responses (solid line) and simulated responses for nonlinear plant with PD hub control (dashed line), to 0.2 m step reference input.

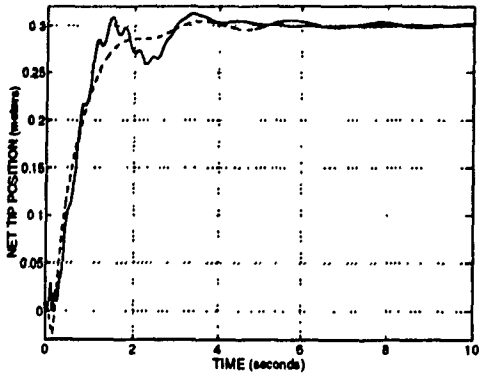

(a) Net tip position.

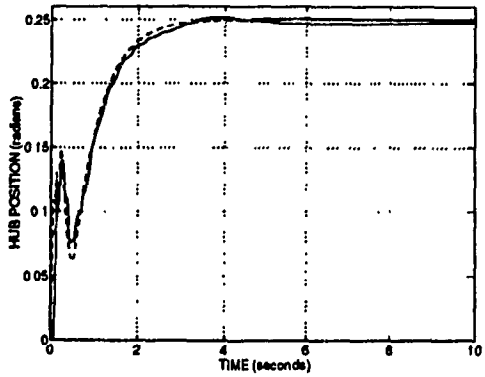

(b) Hub position.

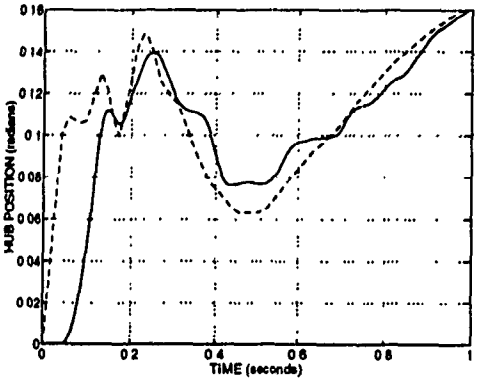

(c) Hub position.

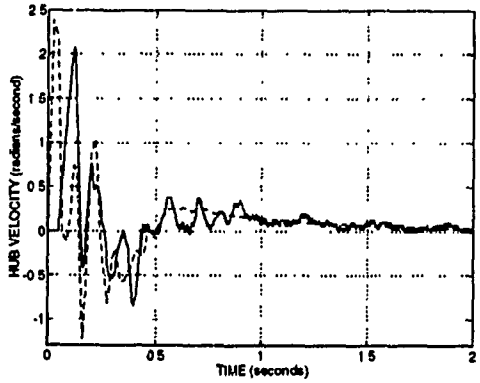

(d) Hub velocity.

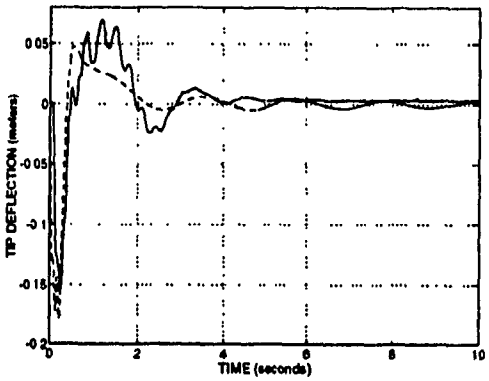

(e) Tip deflection.

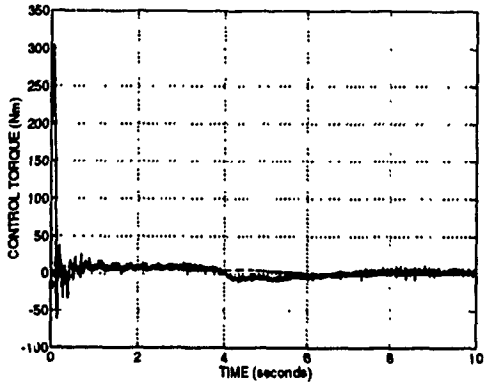

(f) Control torque.

Figure 5.6 Experimental responses (solid line) and simulated responses for nonlinear plant with PD hub control (dashed line), to 0.3 m step reference input.

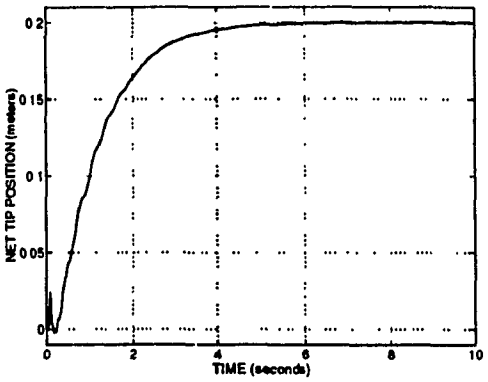

(a) Net tip position.

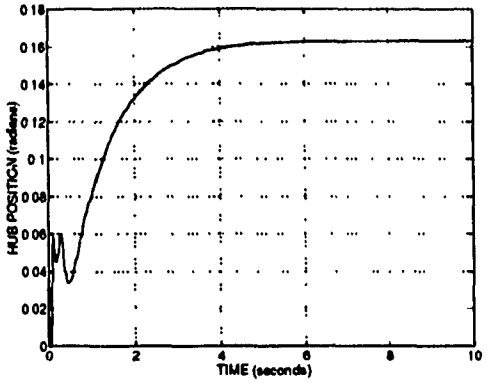

(b) Hub position.

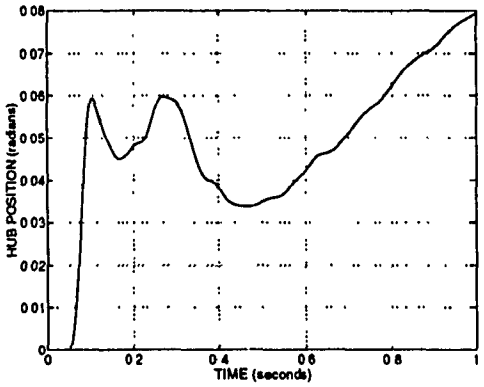

(c) Hub position.

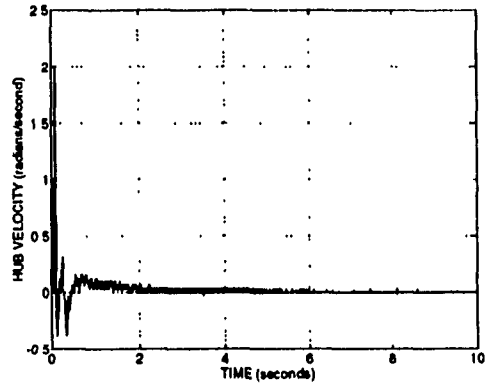

(d) Hub velocity.

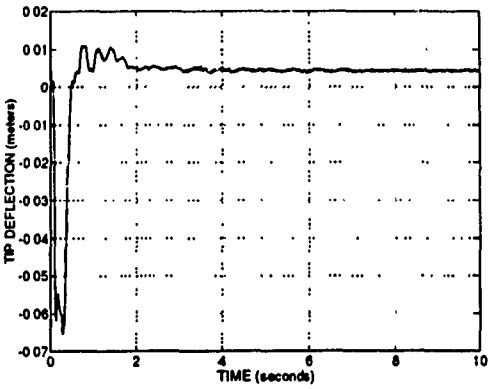

(e) Tip deflection.

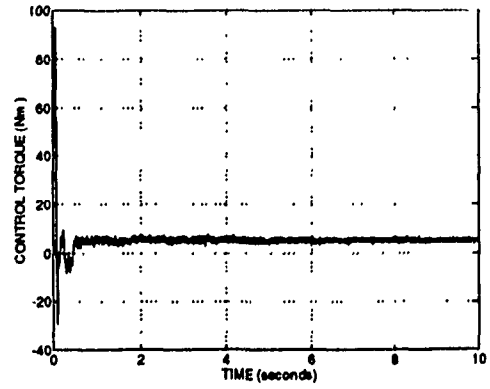

(f) Control torque.

Figure 5.7 Experimental responses to 0.2 m step reference input (K_f=1150).

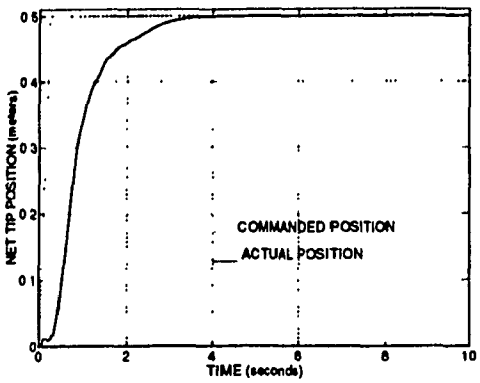

(a) Net tip position.

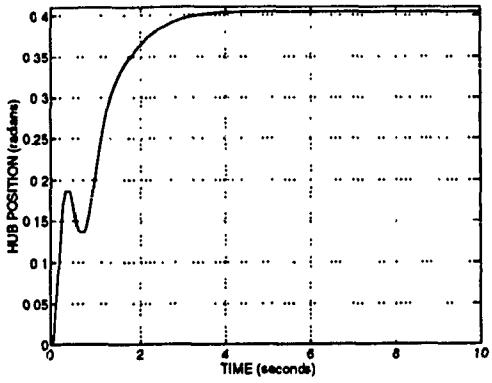

(b) Hub position.

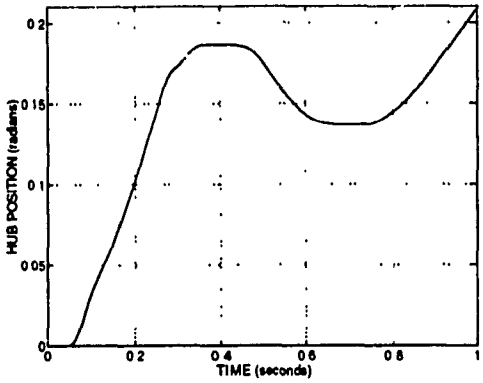

(c) Hub position.

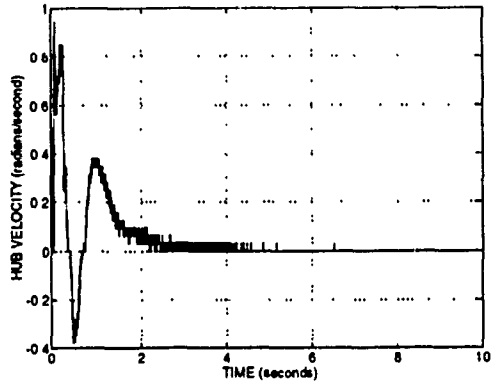

(d) Hub velocity.

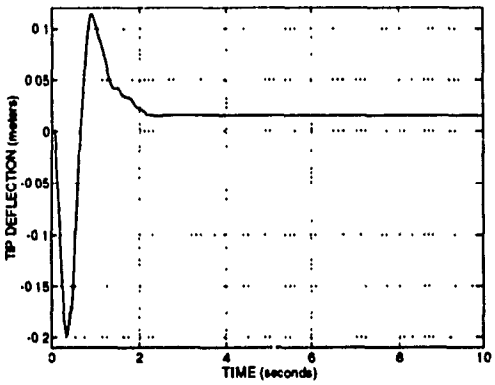

(e) Tip deflection.

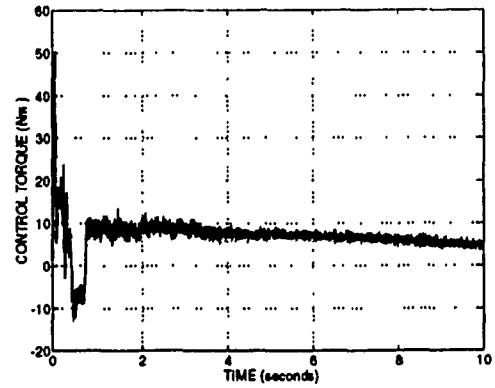

(f) Control torque.

Figure 5.8 Experimental responses to a reference input that ramps to a constant value of 0.5 m.

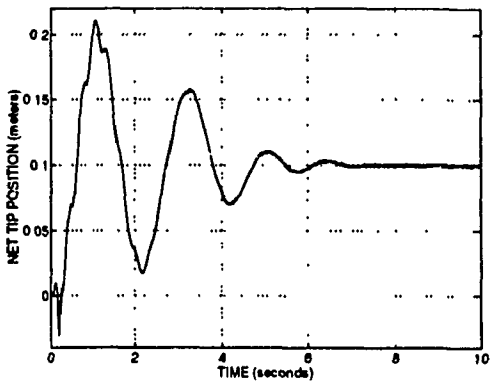

(a) Net tip position.

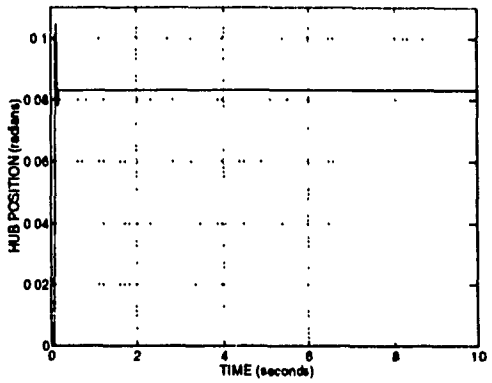

(b) Hub position.

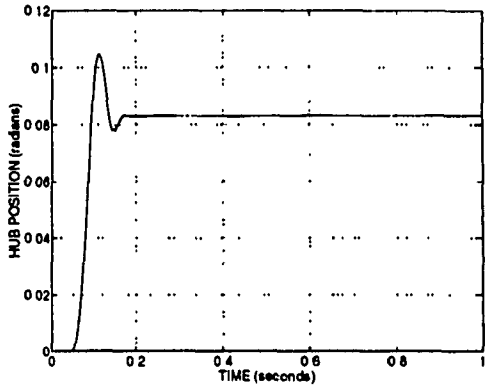

(c) Hub position.

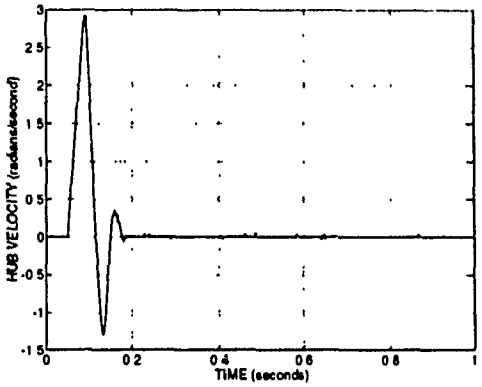

(d) Hub velocity.

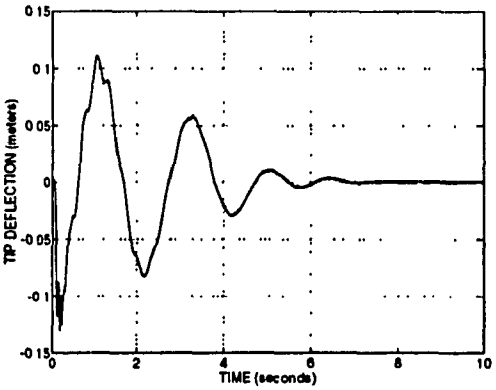

(e) Tip deflection.

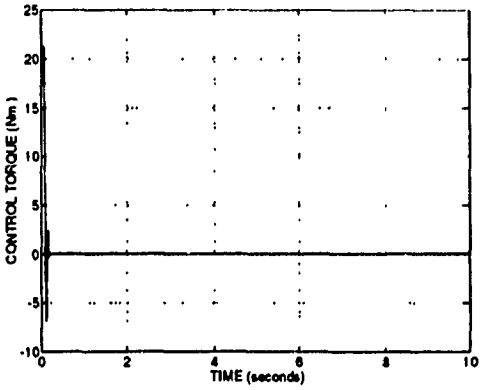

(f) Control torque.

Figure 5.9 Experimental responses of PD hub position control system to 0.083 rad step reference input.

Chapter 6

Discussion, Conclusions and Future Research

6.1 Discussion and Conclusions

As outlined in Section 3.1.2, the objective of the research described in this thesis was to design a controller that

(i) tracks a constant or step reference $y_{ref}(t)$ (set-point tracking), and
(ii) ensures that the closed-loop system remains stable in spite of the destabilizing influence of the open-loop right-half plane zeros.

The experimental results of Chapter 5 reveal set-point tracking with negligible steady-state error for step inputs of 0.1 m, 0.2 m and 0.3 m. The amplitude of the damped 3 rad/s oscillation superimposed upon the nominal steady state-output observed for simulations using the nonlinear plant model is greatly attenuated in the experimental results. This "improved tracking performance" evident in the experimental results is not due to controller action, but is instead a result of the increased damping effect of Coulomb friction in the arm of the test-bed.

Additional discrepancies between the simulated and experimental net tip positions occur during the transient portions of the responses. These oscillations originate in the tip deflection which, when summed with the product $h\theta(t)$, appear in the net tip position. The experimental transient responses contain 19 rad/s oscillations that do not appear in the simulations. In addition, the experimental 0.2 m and 0.3 m responses contain 3 rad/s oscillations during the transient periods that cause rapid rise times to initial peaks at 1.5 s and subsequent undershoots at 2.3 s. The commanded torque values at these times

are well within the saturation limits. Clearly, the controller is unable to suppress these unwanted oscillations.

The high peak commanded torque values at 0.06 s caused by integrator windup apparently excite the first and second flexible modes. The problem of integrator windup can be minimized by stopping the integral action when the commanded torque saturates. Increasing the amplitude of the reference input causes a proportionate increase in the peak torque and results in greater excitation of these modes.

Modification of the servo compensator is required to prevent disturbances of the tip deflection from appearing at the net tip position. These disturbances can be caused by hub stiction which leads to integrator windup and actuator saturation as described above. A worsening of these disturbances can be expected for cases of plant parameter variations and inaccurate plant modeling.

Admittedly, a step is a rather severe reference input that can lead to actuator saturation and excitation of high frequency modes. These effects can be mitigated by decreasing the control gains, as shown in Figure 5.7 where K_1 has been reduced from 1850 to 1150. Alternatively, the reference input signal can be changed to reduce the magnitude of its high frequency content.

Strictly speaking, the approach adopted in this thesis of specifying the gains K_p, K_d, K_1 and K_2 to be constants yields good closed-loop performance for a limited region about the single operating point designated in Section 2.4.5. Applying a rapidly varying reference input to the closed-loop system results in large variations of the plant's states from this operating point. An improvement in the closed-loop performance would be expected by redefining the operating point as the states vary, linearizing the plant for the new operating point, and updating the gains. For a reference input known *a priori*, these calculations can be performed off-line to reduce the computational burden.

Consider the response of Figure 5.8a, which corresponds to a reference input that ramps to a constant value of 0.5 m in 0.25 s. The response reaches steady state in slightly less than 4 s, a performance comparable to the 0.2 m and 0.3 m step responses. Moreover, at 50 Nm, the peak commanded torque for the ramp-to-step input is less than one-quarter and one-eighth of the peak commanded torques for the 0.2 m and 0.3 m step responses,

respectively. Furthermore, the high frequency content of the tip deflection response to the ramp-to-step input is less than for the step inputs. This may indicate that since the continuous time controller contains an internal model of the linearized plant poles, (the poles of $T(s)$ equal those of $G_t(s)$), and because the frequencies corresponding to the higher order poles do not appear in the response, the order of the controller may be decreased and its design simplified.

The hardware features that most complicate the design and implementation of the controller are the large amounts of stiction and Coulomb friction at the hub which originate primarily within the motor. A certain amount of stiction and Coulomb friction are inevitable with a brush type DC motor since commutation always involves friction between the brushes and the commutator. Brushless servo motors, on the other hand, feature electronic commutation. Without brushes, stiction, Coulomb friction and viscous damping are significantly less than for brush type motors.

As an illustration, a particular brush type permanent magnet DC servo motor with a peak torque rating of 0.71 Nm has a static friction torque of 0.0282 Nm. A specific brushless servo motor that can supply 2.53 Nm of peak torque has only 0.0026 Nm of static friction torque. The brushless motor supplies more than 3.5 times the peak torque of the brush type motor, with a ten-fold decrease in the static friction rating.

Another potential hardware improvement involves replacing the flexible arm, a composite structure that includes not just distributed parameter components such as the two parallel steel strips and the central annular tube, but also discrete-mass parts such as the aluminum bridges. For simplicity, however, the arm is modeled as a distributed parameter system with constant mass per unit length. For this reason, an accurate determination of the natural frequencies of vibration of the arm must be performed experimentally rather than by computation using Eq's. (2.23) and (2.28). A homogeneous arm composed of a length of aluminum of rectangular cross-section that is either solid or tubular would be more amenable to accurate modeling using a theoretical approach. Moreover, since there are no moving parts, Coulomb friction within the arm is nonexistent. A solid or tubular arm of rectangular cross-section that possesses the same resistance to torsional flexure as the composite arm, however, also has a larger area

moment of inertia I, and a corresponding increased stiffness factor EI.

As noted in Section 5.2, photodiode detector noise and nonlinearities reduce the accuracy of tip deflection measurements. Tip slope causes a rotation of the diode that decreases the optical power received at the detector. Slope-induced power loss will worsen with the introduction of a moment load, such as adding a second link. Boosting the peak diode current in an effort to minimize the power loss will lead to electrical interference that can generate false triggering of the ADC. **High intensity infrared radiation can cause irreversible retinal damage, and is a serious health hazard unless appropriate eye protection is used.**

An alternate method of measuring tip deflection uses strain gauges. To understand the principle of strain measurement, consider a beam undergoing negative bending as shown in Figure 2.3. The upper surface of the beam is stretched and the lower surface is compressed. Strain, ε, is a measure of the amount of deformation per unit length or fractional change in length. For a differential beam element of length dx undergoing a deformation ds at a point x along the length of the beam, strain is expressed as

$$\varepsilon(x) = \frac{ds}{dx} \quad .$$

It can be shown (Shigley, 1983) that the strain can be written as

$$\varepsilon(x,t) = \frac{cEM(x,t)}{I} \tag{6.1}$$

where $M(x,t)$ is the moment at x, I is the area moment of inertia about the neutral axis, and c is the cross-sectional distance from the neutral axis to the point x on the surface of the beam where the strain is being computed.

Now, applying Eq's. (2.13) and (2.15) yields the following expression that relates the deflection of the beam, $w(x,t)$ to the moment $M(x,t)$ as

$$EI\frac{\partial^2 w(x,t)}{\partial x^2} = M(x,t) \; . \tag{6.2}$$

Substituting Eq. (6.2) into Eq. (6.1) and solving for $\frac{\partial^2 w(x,t)}{\partial x^2}$ yields

$$\frac{\partial w^2(x,t)}{\partial x^2} = \frac{\varepsilon(x,t)}{cE^2} \quad . \tag{6.3}$$

The assumed modes method of Section 2.3.3 can be used to approximate $w(x,t)$ as the finite sum

$$w(x,t) = \sum_{n=1}^{N} \phi_n(x) q_n(t) \quad . \tag{6.4}$$

Equation (6.3) is rewritten as

$$\sum_{n=1}^{N} \frac{d\phi_n^2(x)}{dx^2} q_n(t) = \frac{\varepsilon(x,t)}{cE^2} \quad . \tag{6.5}$$

The eigenfunctions $\phi_n(x)$ and their second derivatives with respect to x can be determined according to the procedure of Section 2.3.2. The functions $q_n(t)$ may now be determined using Eq. (6.5) and the deflection may be found using Eq. (6.4).

Unfortunately, substitution of $x=h$. where h is the free end, into Eq. (6.5) in an effort to evaluate the deflection at this point will fail because the boundary condition for $M(x,t)$ (and $\varepsilon(x,t)$) at h is zero. Evaluation of $q_n(t)$ therefore requires measuring the strain at multiple points along the arm. In essence, the states of the system are being measured. This procedure can be simplified if it is known *a priori* that the system can be accurately described by only a few flexible modes. This limits the number of strain measurements that need be made along the length of the arm. A potential source of error using the strain measurement technique is that inaccurate calculation of the eigenfunctions will cause erroneous deflection values. For a homogeneous arm, accurate eigenfunction calculation may be readily achieved; for more complex structures, however, these calculations may be complicated.

6.2 Future Research

Important areas for further research are robust performance and robust stability, the ability of a closed-loop system to meet performance and stability specifications in spite of plant uncertainty (Doyle *et al* 1992, and Dorato 1987). Uncertainty can arise from:

- inaccurate measurement of the plant's parameters
- parameter drift due to component aging
- variation of the locally linearized plant's poles and zeros as the system's range of operation increases
- unmodeled dynamics, and
- measurement noise.

Any realistic application of the flexible manipulator involves introducing a payload at the tip. A *time-varying* payload substantially complicates the model and the resulting controller. Examination of control strategies for this situation is of significant practical interest.

An additional level of interest and difficulty involves the modeling of and control synthesis for a multiple-link flexible manipulator.

References

Cannon, Jr., R.H., and Eric Schmitz (1984), Initial Experiments on the End-Point Control of a Flexible One-Link Robot. *International Journal of Robotics Research*, Vol. 3. No. 3.

De Luca, A., P. Lucibello, and G. Ulivi (1988), Inversion Techniques for Open and Closed-Loop Control of Flexible Robot Arms. *Proceedings of the 2nd International Symposium of Robotics and Manufacturing Research*, Albuquerque, New Mexico, pp. 529-538.

De Luca, A., and B. Siciliano (1989), Trajectory Control of a Non-Linear One-Link Flexible Arm. *International Journal of Control*, Vol. 50. No. 5., pp. 1699-1715.

Dorato, P. (1987). *Robust Control*, IEEE Press, New York.

Doyle, J.C., B.A. Francis, and A.R. Tannenbaum (1992). *Feedback Control Theory*, Macmillan Publishing Company, New York.

Geniele, H., R.V. Patel, and K. Khorasani (1992), Control of a Flexible-Link Manipulator. *Proceedings of the 4th International Symposium of Robotics and Manufacturing Research*, Albuquerque, New Mexico, pp. 567-572.

Hastings, G.G., and W.J. Book (1987), A Linear Dynamic Model for Flexible Robotic Manipulators. *I.E.E.E. Control Systems Magazine*, Vol. 7. No. 1., pp. 61-64.

Hirschorn, R.M. (1979), Invertibility of Multivariable Nonlinear Control Systems. *I.E.E.E. Transactions On Automatic Control*, Vol. 24, pp. 855-865.

Hughes, P.C. (1987), Space Structure Vibration Modes: How Many Exist? Which Ones Are Important? *I.E.E.E. Control Systems Magazine*, Vol. 7. No. 1., pp. 22-28.

James, M.L., G.M. Smith, J.C. Wolford, and P.W. Whaley (1989). *Vibration of Mechanical and Structural Systems*, Harper and Row Publishers, Inc., New York.

Madhavan, S.K., and S.N. Singh (1991), Inverse Trajectory Control and Zero Dynamic Sensitivity of an Elastic Manipulator. *International Journal of Robotics and Automation*, Vol. 6. No. 4., pp. 179-192.

Madhavan, S.K., and S.N. Singh (1992), Sliding Mode End Point Trajectory Control of a Two Link Elastic Manipulator. *Proceedings of the 31st Conference on Decision and Control*, Tucson, Arizona, pp. 305-310.

Misra, P. (1992), The System Completion Problem: Theory and Computation. *Proceedings of the American Control Conference*, pp. 639-643.

Nebot, E.M., G.K.F. Lee, and T. Brubaker (1988), Experiments on a Single Link Flexible Manipulator. *USA-JAPAN Symposium on Flexible Automation.*

Patel, R.V., and P. Misra (1992), Transmission Zero Assignment in Linear Multivariable Systems, Part II: The General Case. *Proceedings of the American Control Conference*, pp. 644-648.

Patel, R.V., H. Geniele, and K. Khorasani (1993), Control System Design Using Transmission Zero Assignment. *Proceedings of the 12th IFAC World Congress*, Sydney, Australia, Vol. 3, pp. 77-80.

Sakawa, Y., F. Matsuno, and S. Fukushima (1985), Modeling and Feedback Control of a Flexible Arm. *Journal of Robotic Systems*, Vol. 2. No.4., pp. 453-472.

Shifman, J.J. (1990), A Tracking Controller for the Euler-Bernoulli Beam. *Proceedings of the I.E.E.E. International Conference on Robotics and Automation*, Cincinnati, Ohio, pp. 928-933.

Shigley, J.E., and L.D. Mitchell (1983). *Mechanical Engineering Design*, 4th edition, McGraw-Hill Book Company, New York.

Siciliano, B., and W.J. Book (1988), A Singular Perturbation Approach to Control of Lightweight Flexible Manipulators. *The International Journal of Robotics Research*, Vol. 7. No. 4., pp. 79-90.

Thomson, W.T. (1988). *Theory of Vibrations With Applications*, 3rd edition, Prentice-Hall Inc., Englewood Cliffs, N.J.

Wang, D., and M. Vidyasagar (1989), Transfer Functions for a Single Flexible Link. *Proceedings of the I.E.E.E. International Conference on Robotics and Automation*, pp. 1042-1047.

Wang, D. and M. Vidyasagar (1990), Passive Control of a Single Flexible Link. *Proceedings of the I.E.E.E. International Conference on Robotics and Automation*, Cincinnati, Ohio, pp. 1432-1437.

Yuan, B.S., W.J. Book, and B. Siciliano (1989), Direct Adaptive Control of a One-Link Flexible Arm With Tracking. *Journal of Robotic Systems*, Vol. 6. No. 6., pp. 663-680.

APPENDIX A

Taylor Series Expansion Of Equation (2.90)

$$M_3\ddot{q} + C_2\dot{q} + K_1 q = \dot{\theta}^2 K_2 q - m_2\ddot{\theta} \quad . \tag{2.90}$$

Consider the Taylor series expansion of each term of Eq. (2.90) about the operating point $\dot{\theta}_0 = \ddot{\theta}_0 = 0$ and $q_0 = \dot{q}_0 = \ddot{q}_0 = 0$.

$$m_2\ddot{\theta} \approx m_2\ddot{\theta}_0 + \frac{\partial}{\partial\ddot{\theta}}(m_2\ddot{\theta})|_0\delta\ddot{\theta} = m_2\delta\ddot{\theta} \tag{A.1}$$

$$M_3\ddot{q} \approx M_3\ddot{q}_0 + \frac{\partial}{\partial\ddot{q}}(M_3\ddot{q})|_0\delta\ddot{q} = M_3\delta\ddot{q} \tag{A.2}$$

$$C_2\dot{q} \approx C_2\dot{q}_0 + \frac{\partial}{\partial\dot{q}}(C_2\dot{q})|_0\delta\dot{q} = C_2\delta\dot{q} \tag{A.3}$$

$$K_1 q \approx K_1 q_0 + \frac{\partial}{\partial q}(K_1 q)|_0\delta q = K_1\delta q \tag{A.4}$$

$$\begin{aligned}
\dot{\theta}^2 K_2 q &\approx \dot{\theta}_0^2 K_2 q_0 + \frac{\partial}{\partial\dot{\theta}}(\dot{\theta}^2 K_2 q)|_0\delta\dot{\theta} + \frac{\partial}{\partial q}(\dot{\theta}^2 K_2 q)|_0\delta q \\
\dot{\theta}^2 K_2 q &\approx \dot{\theta}_0^2 K_2 q_0 + 2\dot{\theta}_0 K_2 q_0\delta\dot{\theta} + \dot{\theta}_0^2 K_2\delta q \\
\dot{\theta}^2 K_2 q &\approx 0 \quad .
\end{aligned} \tag{A.5}$$

The linearized equations of motion are written by substituting Eq's. (A.1) through (A.5) into Eq. (2.90):

$$M_3 \delta\ddot{q} + C_2 \delta\dot{q} + K_1 \delta q = -m_2 \delta\ddot{\theta} \quad . \tag{A.6}$$

where $\delta q, \delta\dot{q}, \delta\ddot{q}$ and $\delta\ddot{\theta}$ denote small perturbations in $q, \dot{q}, \ddot{q}$ and $\ddot{\theta}$, respectively, about the operating point.

APPENDIX B

Taylor Series Expansion Of Equations (2.102a) & (2.102b)

Consider the Taylor series expansion of Eq.'s (2.102a) and (2.102b) about the operating point q_0, $\dot{q}_0$, $\ddot{q}_0$, θ_0 and $\ddot{\theta}_0$.

$$m_1(q)\ddot{\theta} + m_2^T\ddot{q} + C_1(q,\dot{q})\dot{\theta} + c_{coul}\left(\frac{2}{1+e^{-k\dot{\theta}}} - 1\right) = \tau(t) \tag{2.102a}$$

$$m_2\ddot{\theta} + M_3\ddot{q} + C_2\dot{q} + K_1 q - \dot{\theta}^2 K_2 q = 0 \quad . \tag{2.102b}$$

Expand each term of Eq. (2.102a) by a Taylor series and discard all terms that are second order or higher:

$$\begin{aligned} m_1(q)\ddot{\theta} &\approx m_1(q_0)\ddot{\theta}_0 + \frac{\partial}{\partial q^T}(m_1(q)\ddot{\theta})|_0\delta q + \frac{\partial}{\partial \ddot{\theta}}(m_1(q)\ddot{\theta})|_0\delta\ddot{\theta} \\ &\approx m_1(q_0)\ddot{\theta}_0 + 2\ddot{\theta}_0[\gamma q_0^T + (M_p\Phi(h)q_0)\Phi(h)]\delta q + m_1(q_0)\delta\ddot{\theta} \end{aligned} \tag{B.1}$$

$$\begin{aligned} m_2^T\ddot{q} &\approx m_2^T\ddot{q}_0 + \frac{\partial}{\partial \ddot{q}^T}(m_2^T\ddot{q})|_0\delta\ddot{q} \\ &\approx m_2^T\ddot{q}_0 + m_2^T\delta\ddot{q} \end{aligned} \tag{B.2}$$

$$
\begin{aligned}
C_1(q,\dot{q})\dot{\theta} &\approx C_1(q_0,\dot{q}_0)\dot{\theta}_0 + \frac{\partial}{\partial q^T}[C_1(q,\dot{q})\dot{\theta}]\big|_0\delta q \\
&\quad + \frac{\partial}{\partial \dot{q}^T}[C_1(q,\dot{q})\dot{\theta}]\big|_0\delta\dot{q} + \frac{\partial}{\partial \theta}[C_1(q,\dot{q})\dot{\theta}]\big|_0\delta\theta \\
&\approx C_1(q_0,\dot{q}_0)\dot{\theta}_0 + C_1(q_0,\dot{q}_0)\delta\dot{\theta} \\
&\quad + 2\dot{\theta}_0[\gamma q_0^T + M_p q_0^T(\Phi^T(h)\Phi(h))]\delta\dot{q} \\
&\quad + 2\dot{\theta}_0[\gamma \dot{q}_0^T + M_p \dot{q}_0^T(\Phi^T(h)\Phi(h))]\delta q
\end{aligned}
\tag{B.3}
$$

$$
c_{coul}\left(\frac{2}{1+e^{-k\dot{\theta}}} - 1\right) \approx c_{coul}\left(\frac{2}{1+e^{-k\dot{\theta}_0}} - 1\right) + \frac{2kc_{coul}e^{-k\dot{\theta}_0}}{(1+e^{-k\dot{\theta}_0})^2}\delta\dot{\theta} \tag{B.4}
$$

$$
\tau \approx \tau_0 + \delta\tau \ . \tag{B.5}
$$

Expand each term of Eq. (2.102b), neglecting terms that are second order and higher:

$$
\begin{aligned}
m_2\ddot{\theta} &\approx m_2\ddot{\theta}_0 + \frac{\partial}{\partial\ddot{\theta}}(m_2\ddot{\theta})\big|_{\ddot{\theta}_0}\delta\ddot{\theta} \\
&\approx m_2\ddot{\theta}_0 + m_2\delta\ddot{\theta}
\end{aligned}
\tag{B.6}
$$

$$
\begin{aligned}
M_3\ddot{q} &\approx M_3\ddot{q}_0 + \frac{\partial}{\partial\ddot{q}}(M_3\ddot{q})\big|_0\delta\ddot{q} \\
&\approx M_3\ddot{q}_0 + M_3\delta\ddot{q}
\end{aligned}
\tag{B.7}
$$

$$
\begin{aligned}
C_2\dot{q} &\approx C_2\dot{q}_0 + \frac{\partial}{\partial\dot{q}}(C_2\dot{q})\big|_0\delta\dot{q} \\
&\approx C_2\dot{q}_0 + C_2\delta\dot{q}
\end{aligned}
\tag{B.8}
$$

$$
\begin{aligned}
K_1q &\approx K_1q_0 + \frac{\partial}{\partial q}(K_1q)\big|_0\delta q \\
&\approx K_1q_0 + K_1\delta q
\end{aligned}
\tag{B.9}
$$

$$
\begin{aligned}
-\dot{\theta}^2 K_2 q &\approx -\dot{\theta}_0^2 K_2 q_0 - \frac{\partial}{\partial \theta}(\dot{\theta}^2 K_2 q)\Big|_0 \delta\theta - \frac{\partial}{\partial q}(\dot{\theta}^2 K_2 q)\Big|_0 \delta q \\
&\approx -\dot{\theta}_0^2 K_2 q_0 - 2\dot{\theta}_0 K_2 q_0 \delta\dot{\theta} - \dot{\theta}_0^2 K_2 \delta q \quad .
\end{aligned} \tag{B.10}
$$

The Taylor series expansions of Eq's. (2.102a) and (2.102b) can each be partitioned into a nominal part and a linear perturbed part. The nominal parts of Eq's. (2.102a) and (2.102b) are computed by equating the nominal terms in Eq's. (B.1) through (B.10) and are shown in Eq's. (B.11a) and (B.11b), respectively.

$$
m_1(q_0)\ddot{\theta}_0 + m_2^T \ddot{q}_0 + C_1(q_0, \dot{q}_0)\dot{\theta}_0 + c_{coul}\left(\frac{2}{1+e^{-k\dot{\theta}_0}} - 1\right) = \tau_0 \tag{B.11a}
$$

$$
m_2\ddot{\theta}_0 + M_3\ddot{q}_0 + C_2\dot{q}_0 + K_1 q_0 - \dot{\theta}_0^2 K_2 q_0 = 0 \; . \tag{B.11b}
$$

The linear perturbed part of Eq. (2.102a) is computed by equating the linear perturbed terms in Eq's. (B.1) through (B.5) and is shown in Eq. (B.12a).

$$
\begin{aligned}
&m_1(q_0)\delta\ddot{\theta} + m_2^T \delta\ddot{q} + \left[C_1(q_0, \dot{q}_0) + \frac{2kc_{coul}e^{-k\dot{\theta}_0}}{(1+e^{-k\dot{\theta}_0})^2}\right]\delta\dot{\theta} \\
&\quad + 2\dot{\theta}_0 q_0^T[\gamma + M_p \Phi^T(h)\Phi(h)]\delta\dot{q} \\
&\quad + 2\ddot{\theta}_0[\gamma q_0^T + (M_p \Phi(h) q_0)\Phi(h)]\delta q \\
&\quad + 2\dot{\theta}_0[\gamma \dot{q}_0^T + M_p \dot{q}_0^T(\Phi^T(h)\Phi(h))]\delta q = \delta\tau \quad .
\end{aligned} \tag{B.12a}
$$

The linear perturbed part of Eq. (2.102b) is computed by equating the linear perturbed terms in Eq's. (B.6) through (B.10) and is shown in Eq. (B.12b).

$$
m_2\delta\ddot{\theta} + M_3\delta\ddot{q} - 2\dot{\theta}_0 K_2 q_0 \delta\dot{\theta} + C_2\delta\dot{q} + [K_1 - \dot{\theta}_0^2 K_2]\delta q = 0 \quad . \tag{B.12b}
$$

Consider the operating point $\boldsymbol{q}_0=\dot{\boldsymbol{q}}_0=\ddot{\boldsymbol{q}}_0=\mathbf{0}$, $\dot{\theta}_0$ and $\ddot{\theta}_0$. For $M_p=0$, the approximation to the equations of motion for this operating point is found by substituting the appropriate nominal values into Eq's. (B.11) and (B.12).

The nominal equations of motion are:

$$m_1(\boldsymbol{q}_0)\ddot{\theta}_0 + b\dot{\theta}_0 + c_{coul}\left(\frac{2}{1+e^{-k\dot{\theta}_0}} - 1\right) = \tau_0 \qquad \text{(B.13a)}$$

$$\boldsymbol{m}_2\ddot{\theta}_0 = \mathbf{0}\ . \qquad \text{(B.13b)}$$

Constant $\boldsymbol{m}_2$ is non-zero. Equation (B.13b) therefore implies that $\ddot{\theta}_0=0$. The nominal equation of motion for the system is found by substituting $\ddot{\theta}_0=0$ into Eq. (B.13a):

$$b\dot{\theta}_0 + c_{coul}\left(\frac{2}{1+e^{-k\dot{\theta}_0}} - 1\right) = \tau_0\ . \qquad \text{(B.14)}$$

The linear perturbed equations of motion for the system are found to be

$$m_1(\boldsymbol{q}_0)\delta\ddot{\theta} + \boldsymbol{m}_2^T\delta\ddot{\boldsymbol{q}} + b\delta\dot{\theta} + \frac{2kc_{coul}e^{-k\dot{\theta}_0}}{(1+e^{-k\dot{\theta}_0})^2}\delta\dot{\theta} = \delta\tau \qquad \text{(B.15a)}$$

$$\boldsymbol{m}_2\delta\ddot{\theta} + \boldsymbol{M}_3\delta\ddot{\boldsymbol{q}} + \boldsymbol{C}_2\delta\dot{\boldsymbol{q}} + \boldsymbol{K}_1\delta\boldsymbol{q} - \dot{\theta}_0^2\boldsymbol{K}_2\delta\boldsymbol{q} = \mathbf{0}\ . \qquad \text{(B.15b)}$$

APPENDIX C

Transmission Zero Assignment

The problem is to arbitrarily assign the transmission zeros of $[\boldsymbol{A},\boldsymbol{b},\hat{\boldsymbol{c}},\hat{d}]$, which is equivalent to arbitrarily placing the eigenvalues of $[\boldsymbol{A}-\boldsymbol{b}\hat{d}^{-1}\hat{\boldsymbol{c}}]$. The transmission zero assignment problem thus becomes an eigenvalue assignment problem which can be solved by choosing $\hat{\boldsymbol{c}}$ and $\hat{d}$ appropriately *if* the system $[\boldsymbol{A},\boldsymbol{b},\hat{\boldsymbol{c}},\hat{d}]$ is controllable.

Using the parameter values specified in section 2.4.2, $\boldsymbol{A}$ and $\boldsymbol{b}$ are found to be

$$\boldsymbol{A} = \begin{pmatrix} -0.331 & 0 & 0 & 0 & 1 & 0 & 0 & 0 \\ 0 & -3.310 & 0 & 0 & 0 & 1 & 0 & 0 \\ 0 & 0 & -1.655 & 0 & 0 & 0 & 1 & 0 \\ 0 & 0 & 0 & -4.138 & 0 & 0 & 0 & 1 \\ -9.000 & 0 & 0 & 0 & 0 & 0 & 0 & 0 \\ 0 & -361.380 & 0 & 0 & 0 & 0 & 0 & 0 \\ 0 & 0 & -2704 & 0 & 0 & 0 & 0 & 0 \\ 0 & 0 & 0 & -10404 & 0 & 0 & 0 & 0 \end{pmatrix}$$

$$\boldsymbol{b} = [0.247 \quad 0.496 \quad -0.021 \quad 0.331 \quad 6.727 \quad 54.148 \quad -34.649 \quad 832.674]^T \ .$$

The system $[A,b,\hat{c},\hat{d}]$ is controllable and the transmission zeros of $[A,b,\hat{c},\hat{d}]$ may be arbitrarily assigned.

As explained in Section 3.2.2, $\hat{d}$ is chosen to be 1 in order to simplify the calculations. The vector $\hat{c}$ determines the locations of the transmission zeros as specified for $\hat{G}(s)$ in Table 3.1, where

$$\hat{c} = [20.677 \quad 5.467 \quad -16.099 \quad 0.833 \quad 3.910 \quad 0.082 \quad -0.361 \quad 0.012] \ .$$

APPENDIX D

Observer Design

Consider the system described by Eq. (3.6):

$$\dot{v} = A v + b\delta\theta \tag{3.6a}$$
$$\delta y = c v + d\delta\theta \ . \tag{3.6b}$$

The objective is to construct x, an estimate of state vector v. The vector x is generated by a dynamic system called an *observer*. The observer's inputs consist of $\delta\theta$ and δy and its state is x.

The observer has the form

$$\dot{x} = Ex + b\delta\theta + g\delta y - gd\delta\theta \ . \tag{D.1}$$

Substituting Eq. (3.6b) into Eq. (D.1) yields

$$\dot{x} = Ex + gcv + b\delta\theta \ . \tag{D.2}$$

Defining the error e as v-x, the error dynamics are obtained by subtracting Eq. (D.2) from Eq. (3.6a):

$$\dot{e} = \dot{v} - \dot{x} = Av - gcv - Ex \tag{D.3}$$
$$\dot{e} = (A - gc)v - Ex \ .$$

If $E = A - gc$, Eq. (D.3) can be rewritten as

$$\dot{e} = Ev - Ex = E(v - x) \tag{D.4}$$
$$\dot{e} = Ee \ .$$

If all the eigenvalues of $\boldsymbol{E}$ have negative real parts, the error equation (D.4) is asymptotically stable. This means that $e(t)\rightarrow\mathbf{0}$ and $x(t)\rightarrow v(t)$ as $t\rightarrow\infty$. If the system of Eq. (3.6) is observable, a vector $\boldsymbol{g}$ can always be found to yield any arbitrary set of desired eigenvalues for $\boldsymbol{E}$.

The system $[A,b,c,d]$ is observable and the eigenvalues of $\boldsymbol{E}$ may be arbitrarily assigned. Choosing the eigenvalues of matrix $\boldsymbol{E}$ to be

$$[-15 \quad -15.5 \quad -16 \quad -16.5 \quad -17 \quad -17.5 \quad -18 \quad -18.5]$$

ensures that the observer dynamics do not significantly alter the dynamics of the system. If the vector $\boldsymbol{g}$ is

$$\boldsymbol{g} = [0.115 \quad 0.296 \quad -13.600 \quad -104.151 \quad 0.074 \quad 6.275 \quad -748.137 \quad 3676.619]^T$$

the resulting eigenvalues of $\boldsymbol{E}$ are

$$[-14.99 \quad -15.56 \quad -15.78 \quad -16.44 \quad -16.85 \quad -17.56 \quad -18.04 \quad -18.51]$$

which are close to the desired values.